Measuring the Electron Electric Dipole Moment with Trapped Molecular Ions

by

Matt Grau

B.S., California Institute of Technology, 2009

M.S., University of Colorado Boulder, 2011

A thesis submitted to the

Faculty of the Graduate School of the

University of Colorado in partial fulfillment

of the requirements for the degree of

Doctor of Philosophy

Department of Physics

2016

This thesis entitled:
Measuring the Electron Electric Dipole Moment with Trapped Molecular Ions
written by Matt Grau
has been approved for the Department of Physics

_____

Prof. Eric Cornell

_____

Prof. Jun Ye

Date _____

The final copy of this thesis has been examined by the signatories, and we find that both the content and the form meet acceptable presentation standards of scholarly work in the above mentioned discipline.

Grau, Matt (Ph.D., Physics)

Measuring the Electron Electric Dipole Moment with Trapped Molecular Ions

Thesis directed by Prof. Eric Cornell

An electron electric dipole moment (eEDM) directly violates time-reversal symmetry, a fact which has far reaching implications for physics beyond the Standard Model. An experiment using trapped molecular ions offers high sensitivity because of the large effective electric fields and long coherence times that are possible. We demonstrate precision spectroscopy on many trapped HfF^+ ions in a radiofrequency quadrupole trap with rotating electric and magnetic fields. The spectroscopy performed is a Ramsey type experiment between spin states of the metastable $^3\Delta_1$ electronic state and has a coherence time exceeding 1 second. We have collected and analyzed over 200 hours of Ramsey spectroscopy data taken under a variety of experimental conditions. We identify several systematic errors that could potentially affect an eEDM measurement and estimate the size of these interloping effects. By collecting data under pairs of conditions where the eEDM has opposing signs (e.g. performing Ramsey spectroscopy on the two Λ-doublets) we are able to take frequency differences that can suppress some of these systematic effects. Although our data set includes runs where we have intentionally varied experimental parameters to study systematic effects, we achieve a 1σ statistical sensitivity of 2.76×10^{-28} $e\cdot$cm and place a 1σ upper bound on the size of systematic effects of 2.82×10^{-28} $e\cdot$cm. Finally we present a preliminary upper bound on the eEDM of $|d_e| < 4.6 \times 10^{-28}$ $e\cdot$cm with 90% confidence.

Dedication

To Mom & Dad – Thanks. Also BJ is great.

Acknowledgements

This thesis is only possible thanks to the help of a great many people. In particular my fellow graduate students Dan Gresh and Will Cairncross, who not only make working in lab productive but enjoyable as well. Proper tribute must be paid to Dan for his stoic relentlessness. Like a boulder tumbling down a hill, he will surely crush all opposition in between us and the EDM. Will is as enthusiastic as he is talented, and his zeal for simulation causes me to worry that we might all be inside of one. Additionally, Yan Zhou, amazes me by his embodiment of the principle of superposition - he seems to be everywhere and working on everything at once. Kia is new to the group, but I am sure that he will have the experiment control completely rewritten in Python in no time flat. Finally I must thank Yiqi Ni, our brilliant undergraduate, who did all the real work on the experiment while only complaining a little.

I've been very fortunate to work with exceptionally great colleagues in the past as well. Huanqian Loh was a fantastic labmate for many years on the experiment, and a great role model for me. I learned a great deal from her. I've also benefited greatly from working closely with Kevin Cossel, ever since he lent me a drill almost a decade ago. Additionally I'd like to thank Kang-Kuen Ni, Laura Sinclair, Russel Stutz, Tyler Yahn, and Tyler Coffey for all of their past contributions to the experiment.

My advisers Eric Cornell and Jun Ye have been influential in more ways than I have space to write about here. Eric taught me to question everything, and to never even think about collecting data without a plan to analyze and interpret it first. His intuition for physics never ceases to astonish me. Jun is a constant source of energy and enthusiasm, and is never afraid to jump right

into any problem that needs solving. I'd also like to thank Deborah Jin and her group for great feedback during the Jin/Cornell meetings, and also Pam Leland and Krista Beck, who are the only reason anything ever gets done.

I've had great technical support from the JILA instrument shop and electronics shop. Todd Asnicar machined and delicately hand polished the ion trap that made all of the experiments in this thesis possible. He did a great job, and the trap has never disappointed me. David Alchenberger was critical in cleaning the trap electrodes for ultrahigh vacuum and gold coating them for high optical reflectivity. Terry Brown, James Fung-A-Fat, Carl Sauer, and Chris Ho all provided expert guidance for electronics projects large and small.

My fellow classmates at CU, Dan Weflen, Maya Fabrikant, Dan Lobser, Adam Kaufman, and Brandon Ruzic, have provided me the occasional useful idea as well as the more occasional entertaining diversion. In particular Josh Weiner has been a great friend for the past decade, ever since he explained to me how a rotisserie functioned in undergrad. Jon Malmaud aided me with tons of useful insight into statistics and general strategic thought. Todd Gingrich has always been a source of motivation for me. I'd also like to thank John Leichty for more than a little help with microcontrollers, and Dan Lo and Gabe Cohn for answering countless questions about FPGAs and digital electronics.

I've had many great teachers along the way, but I'd like to especially thank Michael Cross and Gil Refael for always having time to answer my questions. Mondania Gallagher was my wonderful middle school science teacher who was always engaged and ever patient. She was always delighted to share in her students' discoveries. Karen Young was a great teacher and an awesome scoutmaster. Without them I would be nowhere.

I'd also like to thanks my parents, my siblings Dan, Christina, and Maria for their support, as well as all my family in Virginia, Maryland, and especially Colorado for their unwavering encouragement and cheer-leading. Finally, I want to thank my wonderful wife BJ for her love and care while I've been writing this. She also painstakingly revised the inchoate neighing and braying of barnyard animals into something that resembles prose. She pushes me to be all I can be.

Contents

Chapter

Tables

Table

Figures

Figure

Chapter 1

Introduction

1.1 The electron EDM

The electron is an elementary particle that has a well defined mass ($m_e = 9.10938356(11) \times 10^{-31}$ kg) and a well defined charge ($-e = -1.6021766208(98) \times 10^{-19}$ C)[49]. It is appealing to visualize the electron as a small clump of charged "stuff" with mass m_e and charge e. Additionally the electron has intrinsic angular momentum, known as spin, that has no classical analog. The electron spin is a vector quantity $\left|\vec{S}\right| = \frac{1}{2}\hbar$, where $\hbar$ is the reduced Planck constant. For much of the rest of this thesis we will consider units where $\hbar = 1$, and the electron spin is simply $\frac{1}{2}$. As the electron has both charge and angular momentum it must have a magnetic moment, which for a non-relativistic object is

$$\vec{\mu} = \frac{1}{2}\left(\frac{-e}{m_e}\right)\vec{S} = -\mu_B \vec{S}. \tag{1.1}$$

Where $e/2m_e = \mu_B$ is the Bohr magneton. However, Thompson scattering shows that the electron radius is less than 10^{-15} m, which would mean that in a classical calculation of the angular momentum of the electron that the outside radius of the electron is moving at relativistic speeds. Therefore we must use the relativistic Dirac equation to calculate the magnetic moment. The Dirac equation finds a magnetic moment that is a factor of 2 larger than the naive non-relativistic expectation,

$$\vec{\mu} = -2\mu_B \vec{S}. \tag{1.2}$$

This difference from the non-relativistic expectation is typically contained in a factor g, the so-called g-factor, $\vec{\mu} = -g_s \mu_B \vec{S}$, where $g_s = 2$ is the relativistic electron spin g-factor. In fact, the

electron spin g-factor is not quite equal to 2, more precisely $g_s \approx 2.0023$. This difference from 2 is referred to as the anomalous magnetic moment of the electron, $a_e = (g_s - 2)/2$. It arises due to higher order interactions of the electron with itself in Quantum Electrodynamics (QED). A free electron is surrounded by a "cloud" of virtual particles: virtual photons and virtual electrons. These virtual particles provide radiative corrections to the magnetic moment of the electron, which can be calculated in a perturbation series,

$$a_e = \left(\frac{\alpha}{\pi}\right) A_e^{(2)} + \left(\frac{\alpha}{\pi}\right)^2 A_e^{(4)} + \left(\frac{\alpha}{\pi}\right)^3 A_e^{(6)} + \dots \tag{1.3}$$

where $\alpha \approx 1/137$ is the fine structure constant, and the terms $A_e^{(n)}$ are the integrals of the n^{th} order QED Feynman diagrams describing the electron magnetic dipole moment. Almost surprisingly, this perturbative calculation agrees well with experiment out to 10^{th} order and beyond. The calculated value $a_e = 0.00115965218178(77)$[4] agrees with the experimentally determined value of $a_e = 0.00115965218073(28)$[33] made by single electron cyclotron measurements in a Penning trap. This extreme precision and marvelous agreement between experiment and theory are one of the crowning successes of QED.

Seeing as the phenomenon of the electron magnetic moment is so rich we might next consider an electric dipole moment (EDM). Unfortunately, simply referencing an elementary textbook[10] will tell us that fundamental particles (such as electrons) and nuclei (such as neutrons) must not have any electric dipole moments because parity is a conserved quantity. The electric dipole moment can be expressed as

$$d_e = \int dx_j e_i r_i |\psi(r_j)|^2, \tag{1.4}$$

where r_i is the position coordinate along the i^{th} dimension, e_i is the charge distribution along that dimension, $\psi(r)$ is the particle wavefunction as a function of spatial coordinate, and repeated indices represent a sum over that index. A parity inversion operation $r_i \to -r_i$ should leave the system invariant, and we find that $d_e = -d_e = 0$. However, Purcell and Ramsey pointed out in 1950 that this argument is ludicrous[55]. This sort of theoretical argument rests on an assumption that has not been tested, namely that parity is a perfect symmetry of nature, and the proper course of action

is to either validate or invalidate this argument by the means of an experimental measurement. They argued that EDMs of fundamental particles and nuclei could be used as observables for symmetry violations. At this point in time there was not conclusive evidence against the existence of EDMs, most experiments were not sensitive to EDMs that were smaller than 10^{-13} e·cm. Smith, Purcell, and Ramsey then performed an experiment to measure the EDM of the neutron. The used a polarized beam of neutrons in a 71.6 keV/cm electric field to place an upper limit on the neutron EDM of $|d_n| < 5 \times 10^{-20}$ $e \cdot$cm[67]. This type of experiment is only suitable for experiments on neutral particles, as a charged particle such as an electron would be quickly accelerated out of the beam path.

As it turns out, parity is not a conserved quantity, demonstrated by the angular distribution of parity violating Beta decays[74] and meson decays[29]. Lee and Yang calculated that the size of the neutron EDM which would be generated by the amount of parity violation measured in [74] and [29] would be well below the measured upper bound of $|d_n| < 5 \times 10^{-20}$ $e \cdot$cm[43]. Moreover, Landau theorized that even though parity P is not a good symmetry, that CP, the product of the symmetries of charge conjugation C and parity P, is a good symmetry. If CP is a good symmetry then we should not expect EDMs of fundamental particles to exist.

In 1964 Cronin and Fitch found direct evidence of CP violation in the decay of the K_2^0 meson[15]. This finding renewed interest in the measurement of fundamental particle EDMs. Sandars performed one of the first electron EDM experiments, measuring the EDM of a beam of neutral Cesium atoms to be $|d_{Cs}| < 2.2 \times 10^{-19}$ $e \cdot$cm[63]. While it was shown by Schiff[64] that in the non-relativistic limit an atom such as Cesium has no EDM even if its constituent electrons do, in a relativistic treatment the EDM of the atom can be more than 100 times larger than that of the electron[61]. Sandars was able to interpret the Cesium EDM limit as an electron EDM limit of $|d_e| < 2 \times 10^{-21}$ $e \cdot$cm, a factor of 10^5 smaller than limits placed by scattering electrons off of ^{4}He at the Stanford linear accelerator[31].

The CP violation measured so far has been in the hadronic sector of the Standard Model, affecting primarily heavy quarks. It can be included in the Standard Model as a single CP violating

phase in the Cabibbo-Kobayashi-Maskawa (CKM) matrix that describes the mixing of quarks[12, 41]. The CP violating phase in the CKM matrix may contribute to a neutron EDM at the $d_n < 10^{30}$ e·cm level, which is still beyond the current best limit of 2.9×10^{26} e·cm[5]. Even though this CP violation primarily affects hadrons, it does have the potential to contribute to an electron EDM through very high order effects. These high order effects can be represented as Feynman diagrams where an electron couples to a quark loop containing a CP violating phase via several virtual W bosons. These Feynman diagrams are exactly zero out to second order[9], so only third order and higher diagrams contribute. An example of such a high order Feynman diagram is shown in fig. 1.1.

We can make a back-of-the-envelope calculation by summing over the vertices of such a diagram,

$$d_e = \frac{1}{(4\pi)^5} e G_F m_e \alpha^2 \alpha_s J, \tag{1.5}$$

where G_F is the Fermi coupling constant, α is the fine structure constant, α_s is the strong coupling interaction constant, and J is an invariant combination of angles in the CKM matrix to which any CP violating effects in the Standard Model must be proportional. If we use a value of $J = 2 \times 10^{-4}$ we obtain an upper bound for the Standard Model prediction of the electron EDM of $|d_e| < 10^{-37}$ e·cm.

While the amount of CP violation already included in the Standard Model is insufficient to generate a large electron EDM, there are still compelling reasons to suspect more CP violation,

Figure 1.1: Example of a three-loop electron EDM Feynman diagram, where an electron couples to a CP violating quark loop via W bosons.

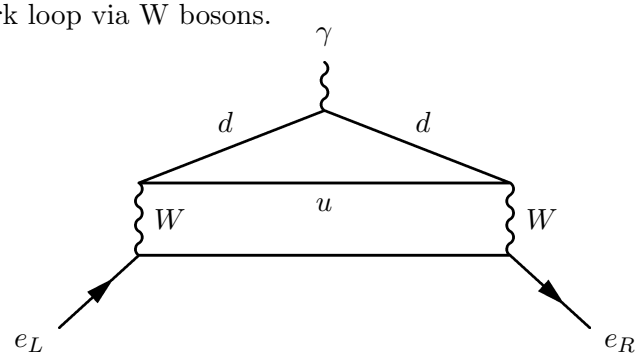

and thus larger electron EDMs could exist. One such reason is the asymmetry between matter and antimatter in the universe, or . The so-called baryon asymmetry can be estimated by the baryon to photon ratio, $\eta = (N_B - N_{\bar{B}})/N_\gamma = 5.8 \pm 0.27 \times 10^{-10}$[14]. The matter-antimatter difference is normalized by photon number because equal portions of matter and antimatter can annihilate and produce photons. Balloon experiments have searched for signatures of antihelium by measuring antiproton decays with no evidence of antibaryons[2]. Sakharov proposed a potential solution to this problem[60]. In order to produce this asymmetry we need a mechanism where matter and antimatter can be produced at different rates. In order to produce matter and antimatter at different rates these three criteria must all be met:

(1) Baryon number violation

(2) Interactions out of thermal equilibrium

(3) CP violation

However, the amount of CP violation required to produce a baryon asymmetry as large as 10^{-10} is much more than is present in the CP violating phase in the CKM matrix. The quantity of CP violation required to satisfy Sakharov's criteria could generate an electron EDM as large as 10^{-29} $e\cdot$cm[28].

Additionally, many physical theories predict new physics beyond the confines of the Standard Model. Nearly all of them introduce new CP violating phases ϕ_{CP} which allow for an electron EDM that is much larger than that predicted by the Standard Model [9, 54]. These CP violating phases can couple to the electron at the one-loop level, meaning that their effect can be greatly enhanced

Figure 1.2: Example of a one-loop contribution to the electron EDM from a Beyond Standard Model theory where the electron couples to some source of CP violation directly via a new fermion F or boson B.

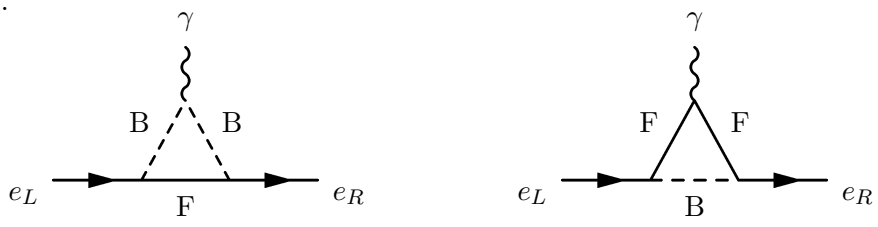

compared to the CP violating phase found in the CKM matrix that couples to the electron only above the three-loop level[25]. The size of an electron EDM we expect from a one-loop diagram coupling the electron to some new physics at energy scale Λ is

$$d_e = e\left(\frac{\alpha}{4\pi}\right)\left(\frac{\hbar c}{m_e c^2}\right)\left(\frac{m_e c^2}{\Lambda^2}\right)^2 \sin(\phi_{CP}). \tag{1.6}$$

Without any sort of specific symmetry requirement constraining the value of ϕ_{CP} we can assume that $\sin(\phi_{CP}) \sim 1$. If $\Lambda \sim 10$ TeV, then $d_e \sim 5\times10^{-29}$. This prediction is an attractive proposition, because it means that by constructing sensitive probes of the electron EDM we can probe for new physics at the several TeV scale.

1.1.1 EDM searches

Following the Sandars electron EDM experiment in 1964 there have been many attempts to measure the electron EDM in atomic systems, including those in Cesium[72], metastable Xenon[53], and Thallium[1]. The most recent atomic beam experiment, performed by Commins, reported $d_e = 6.9 \pm 7.4 \times 10^{-28}$ e·cm, placing an upper bound on the electron EDM of $|d_e| < 1.6\times10^{-27}$[57]. In this experiment Commins measured the EDM of atomic Thallium, which has an EDM with and opposite sign a factor of 585 larger than the electron EDM, by applying a 122 kV/cm electric field to a Thallium beam with a detected count rate of almost 10^9 per second. The dominant systematic in this and other atomic beam experiments comes from motional magnetic fields. This systematic arises because the atoms moving in the applied lab-frame electric field experience a rest-frame magnetic field. This rest-frame magnetic field leads to a Zeeman shift that is linear in applied electric field and mimics an electron EDM of the size $(v/c)\mu_m \sim 10^{-17}$ e·cm. This effect is many orders of magnitude larger than the sensitivity that these beam experiments hope to obtain, so the experiments require extremely precise cancellation via a co-magnetometer species. The Thallium experiment used Sodium as a co-magnetometer species. By carefully measuring the motional fields experienced by the co-magnetometer species this effect can be subtracted off.

A way to improve upon the electron EDM limit set by atomic beam experiments is to use a

molecular beam. The figure of merit for the sensitivity of an EDM experiment is $\mathcal{E}_{\text{eff}}\tau\sqrt{\dot{N}}$, where $\mathcal{E}_{\text{eff}}$ is the size of the effective electric field that can be applied to the electron, τ is coherence time, and $\dot{N}$ is the experimental count rate. Molecules have much more closely spaced energy states, which means that they can be fully polarized with an electric field, making the effective electric field $\mathcal{E}_{\text{eff}}$ experienced by the electron much larger. This means that the ratio of the molecular EDM to the electron EDM can be a factor of ~ 1000 larger than the enhancement factor in an atomic experiment. The first molecular experiment was performed by Imperial College, using a beam of YbF molecules. They measured the electron EDM to be $d_e = -2.4 \pm 5.7_{\text{stat}} \pm 1.5_{\text{syst}} \times 10^{-28}$ $e{\cdot}$cm, placing a 90% confidence interval upper bound on the electron EDM of $|d_e| < 10.5 \times 10^{-28}$[36]. This experiment benefited from an effective electric field that was 220 times larger than that of the Thallium atomic beam experiment. With over 270 hours of data the measurement is still statistics limited. The dominant systematics are on the 1×10^{-28} $e{\cdot}$cm level. One systematic was due to correlations with their electric field switch, caused by incomplete electric field reversals. Another dominant systematic was a correlated signal with the detuning of the $\pi/2$ pulses, causing an initial phase shift in their Ramsey fringe[39].

Another potential advantage of molecules is that they often possess closely spaced parity doublets. A parity doublet can be exploited like an "internal co-magnetomoeter" to remove the effect of any motional fields or other systematics. Additionally, these doublets are typically more closely spaced than rotational energy levels, allowing such molecules to be polarized by electric fields of only several V/cm. This further reduces systematic effects due to leakage currents created by, e.g., charging large capacitor places in order to apply the very large electric fields required to mix rotational levels. This technique was first demonstrated by an experiment at Yale using a vapor cell of PbO[23]. The species PbO has a $^3\Sigma^+$ state which possesses an Ω-doublet. This experiment was able to achieve an electron EDM measurement of $d_e = -4.4 \pm 9.5_{\text{stat}} \pm 1.8_{\text{syst}} \times 10^{-27}$ $e{\cdot}$cm.

Using a similar technique, the ACME collaboration at Harvard and Yale have performed the most sensitive electron EDM experiment to date. The molecular species ThO has an effective electric field of 75.2 GV/cm[27], and the $^3\Delta_1$ state of ThO possesses a similar doublet structure to

the $^3\Sigma^+$ state of PbO. ACME was able to measure the electron EDM to be $d_e = 2.1 \pm 3.7_{\text{stat}} \pm 2.5_{\text{syst}} \times 10^{-29}$ $e\cdot$cm, placing an upper bound of $|d_e| < 8.7 \times 10^{-29}$ $e\cdot$cm with 90% confidence[7]. The largest systematic effects in this experiment are constrained to the 10^{-29} $e\cdot$cm level:

- A laser polarization gradient causes an initial phase shift of the Ramsey fringe that is at the 10^{-29} $e\cdot$cm level. This is caused by laser-induced thermal stress birefringence in the optically transparent electric field plates. The ThO molecules are initially prepared with spin orientation dependent on laser polarization. This polarization gradient induces a phase between the dark and bright states, creating the initial phase shift that is indistinguishable from a frequency shift at later time in the Ramsey fringe.

- Change of state preparation laser pointing of 5 μrad can have an effect that is correlated with the direction of the electric field that is a 10^{-29} $e\cdot$cm effect.

- State preparation and state readout laser detuning has a 1×10^{-29} $e\cdot$cm systematic effect.

In this thesis we will describe an experiment to measure the electron EDM using molecular HfF^+ ions in an rf quadrupole trap. By using a molecular species such as HfF^+ we will take advantage of the large effective electric field typical of molecules, and also the systematic error rejection that comes from using a $^3\Delta_1$ state with a parity-doublet internal co-magnetometer. Moreover, because we will use molecules in an ion trap rather than in a beam, we will have access to the Ramsey fringe at all times during its evolution, compared to a beam experiment that can only measure at the outlet of the experiment apparatus. This will make us less susceptible to systematic effects caused by imperfect state preparation that will cause initial phase shifts of the Ramsey fringe.

1.2 Overview for thesis

This chapter provides some motivation for the importance of an electron EDM search, as well as providing some historical perspective. In chapter 2 we will discuss the apparatus we use to perform the eEDM measurement. We will also provide an overview of the techniques we use to

create, manipulate, trap, and detect the molecular ions used in the experiment. Additionally this chapter will cover some of the technical details involved in automating a complex experiment that is capable of self correcting its parameters based on the results of analyzed data. We will then review the statistical sensitivity of the experiment in chapter 3, and describe the Ramsey sequence we will use to measure the eEDM. We will also discuss measurement strategies we can adopt to optimize the statistical sensitivity achievable in a fixed amount of time. Next, in chapter 4 we explore the various systematic effects we have so far uncovered that might affect a precision eEDM measurement. Finally, in chapter 5 we summarize the systematic effects characterized in chapter 4 and use over 200 hours of data to calculate the size of these systematic shifts and estimate the uncertainties of the corrections we must apply to cancel these shifts. With a full estimate of all known systematic effects we calculate a preliminary upper bound on the size of the electron EDM.

Chapter 2

Experimental apparatus

In this chapter we will outline the design of the experimental apparatus, with particular attention paid to the components that make an appearance in the following chapters.

2.1 Summary of techniques

Many of the techniques we use to prepare, manipulate, and detect our molecules were pioneered by Huanqian Loh and Kevin Cossel. We will briefly survey these techniques for the sake of completeness, but for a thorough discussion the reader is directed to the PhD theses [44] and [18].

2.1.1 Choice of molecular species

We choose to work with HfF^+ as the foundation of our experiment. There are several advantages to this choice of molecule. The molecule HfF^+ was pointed out to have a large internal effective electric field, $\mathcal{E}_{\text{eff}}$,[48], and subsequent studies[51, 47, 26] calculated the value of $\mathcal{E}_{\text{eff}}$ to be 24–30 GV/cm. We will use the most recent determination[26] of 23.3 GV/cm in all future calculations that involve $\mathcal{E}_{\text{eff}}$. The most recent calculation uses 34 valence electrons in its calculation. Additionally, HfF^+ possesses a $^3\Delta$ molecular symmetry. In particular, the $^3\Delta_1$ electronic state contains two closely spaced opposite parity states, allowing it to be fully polarized with electric fields as small as ~ 1 V/cm. Once the molecule is fully polarized we can take full advantage of the internal effective electric field in our Ramsey experiment. Finally, the $^3\Delta_1$ state in HfF^+ is very low-lying. PFI-ZEKE studies have experimentally determined that the ground state of HfF^+ is

$^1\Sigma_0^+$, and the $^3\Delta_1$ state is located at 978.3 cm^{-1}[6]. This low energy gives the $^3\Delta_1$ a long radiative lifetime of 2.1(2) second[50]. This long lifetime has allowed us to achieve a long coherence time of ~ 1 second when performing Ramsey spectroscopy to measure the electron EDM. In order to take advantage of this long lifetime we use a radio-frequency Paul trap to confine the HfF^+ ions so that the linewidth of our Ramsey experiment is not transit time broadened, as would be the case in a beam-type experiment.

2.1.2 Neutral HfF production

To produce the HfF^+ molecules that will be used in the experiment we must first have the neutral species HfF. We produce the neutral molecules by using a small, variable repetition rate Nd:YAG pulse laser to ablate the surface of a Hf metal rod. At the same time, a piezo-actuated valve releases a pulse of 99% Ar gas seeded with 1% SF_6. The ablation plume is entrained in the gas pulse and HfF molecules are produced. The HfF molecular beam is cooled through supersonic expansion to a rotational temperature of $\sim$ 10 Kelvin, measured by laser-induced fluorescence spectroscopy. Two skimmers, one 2mm in diameter and a second 3mm in diameter, collimate the beam before it enters the ion trapping region.

2.1.3 Photoionization

Once the neutral HfF molecules enter the ion trapping region our task is to ionize them. We employ a two-photon process to promote a valence electron of HfF to a highly excited Rydberg state that is 54 cm^{-1} above the HfF ionization threshold of 59462(2) cm^{-1}. The first photon is the doubled output of a 3-stage dye laser amplifier seeded by the doubled output of a 1240 nm high power diode laser. We achieve ~ 5 μJ per pulse at 309.388 nm. The linewidth of this laser is sufficient to resolve transitions of the various HfF isotopologues, allowing us to address transitions of only the $^{199}Hf^{19}F$ isotopologue. The second photon is the doubled output of a commercial dye laser, at a wavelength of 368.351 nm with pulse energy of 100-1000 μJ depending on the number of ions we would like to produce. Once promoted to a Rydberg state above the ionization threshold,

the HfF molecules quickly autoionize. The Rydberg state is energetically allowed to decay only to the $^1\Sigma_0^+, v = 0$ vibronic ground state of HfF^+, although this could be spread out over as many as 13 distinct rotational states. However, we observe a propensity of the Rydberg HfF molecules to decay only into a few ion rotational states with a specific parity. By choosing the correct parity of the intermediate state we can prepare as much as 50% of the ions in the $^1\Sigma_0^+, v = 0, J = 0$ state[46].

Once the molecules are ionized we confine them with an rf quadrupole trap. The details of ion trapping are discussed more in section 2.2.

2.1.4 State transfer

After ionization we transfer population from the $^1\Sigma_0^+$ ground state to $^3\Delta_1$, the state we wish to perform Ramsey spectroscopy on. We use two cw lasers with crossed linear polarizations directed along the axial direction of the ion trap in order to avoid sampling the Doppler shifts caused by trap micromotion. The transfer laser wavelengths are $\lambda_S = 899.670$ nm and $\lambda_T = 986.422$ nm, chosen to couple the $^1\Sigma_0^+$ $v = 0, J = 0$ and $^3\Delta_1$ $v = 0, J = 1$ states via intermediate state $^3\Pi_{0+}$ $v = 0, J = 1$ (fig. 2.1). The high-lying $^3\Pi_{0+}$ intermediate state has strong transition dipole moments and good Franck-Condon overlap with both lower states[45]. Both transfer lasers are external cavity diode lasers with tapered amplifiers and provide about 1.5 W of power each. The two lasers are locked to two separate modes of a high-stability cavity. Most of the power from each laser is sent to the ion trap with polarization-maintaining single-mode fiber. At the ion trap, we obtain about 200 mW of power at 899 nm and 500 mW at 986 nm. We initially operated with a total single-photon detuning (Δ) of 160 MHz. However, we found that scattered light in the trap chamber led to single-photon line broadening in the presence of the rotating electric-field due to the large Doppler shifts arising from the rotational micromotion. To reduce the spontaneous emission, we increased the single-photon detuning to ~ 1.5 GHz.

We use an AOM to tune the frequency of the down-going transfer laser such that when we apply an electric field it addresses a single Stark level of $^3\Delta_1, v = 0, J = 1$. In a half period of axial oscillation in the trap, each ion experiences a two-photon Doppler shift $\delta(t)$, causing a sweep

Figure 2.1: Schematic diagram of the experimental setup during state transfer from ${}^1\Sigma_0^+$ to ${}^3\Delta_1$. We use two lasers, labelled S and T to transfer population from ${}^1\Sigma_0^+, N = 0$ to ${}^3\Delta_1, J = 1$ through the intermediate ${}^3\Pi_{0+}, J = 1$ state. Both lasers are detuned $\Delta \approx 1.5$ GHz from the intermediate ${}^3\Pi_{0+}$ state in order to prevent populating this state. The transfer lasers also have a two-photon detuning $\delta(t)$ from the final state within the ${}^3\Delta_1, J = 1$ state manifold. This detuning is the result of the Doppler shift due to harmonic motion in the ion trap.

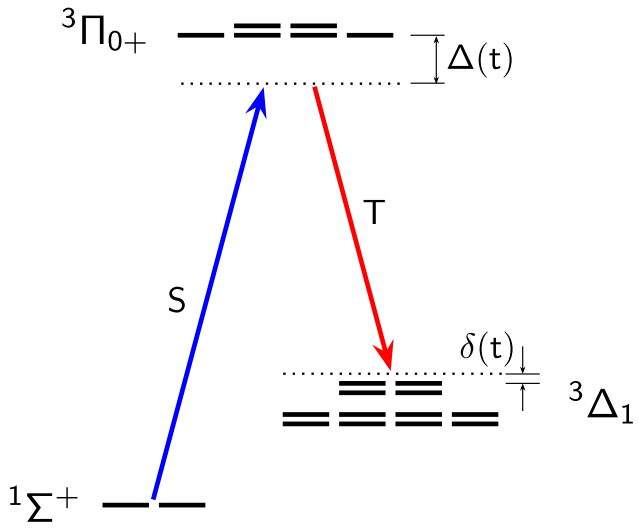

through the two-photon resonance. The probability of transfer for a single ion in a half trap cycle is given by the Landau-Zener formula, $P = e^{\frac{2\pi\Delta^2}{\hbar\dot{\delta}}}$. For $P \sim 1$ it is enough to pulse the transfer lasers on for half a period of axial oscillation. However, the temperature of the ions in the axial direction is ~ 30 K, and $P \ll 1$. In this case we pulse the transfer lasers for many axial periods until the population equilibrates between the $^1\Sigma_0^+$ and $^3\Delta_1$ states. In this scenario we expect a transfer efficiency of ~ 50 %, but we observe 37(2) %. This discrepancy could potentially be due to ion-ion collisions.

2.1.5 State detection

After the HfF^+ions are transferred into the $^3\Delta_1$ state we are ready to perform Ramsey spectroscopy. The Ramsey spectroscopy is covered in detail in chapter 3. The final step in the spectroscopy is to be able to detect the state of the ions. We explored two options: laser-induced fluorescence and photodissociation.

(1) Laser-induced fluorescence

The ion trap was designed to facilitate the detection of ions using laser-induced fluorescence, where a laser pulse would state-selectively promote the ion to an excited state from which it could decay, emitting a photon in the process. This photon could be collected onto a photomultiplier tube, allowing us to count the ions in a particular state. We demonstrated this technique in an ion beam in [46] to detect the rotational states of the HfF^+ ground state, $^1\Sigma_0^+$. The trap was designed to optimize the signal possible with this detection technique. Two ellipsoidal reflecting electrodes were placed around the trap, subtending 80% of the solid angle, designed to focus fluorescence from the center of the ion trap to light pipes leading to photomultiplier tubes. These reflecting surfaces needed to be metallic, because any insulator near the trap could disrupt the uniformity of the ion trap. The reflecting surfaces also needed to be highly polished, so we chose to work with polished aluminum. Because aluminum typically has poor ultrahigh vacuum performance due to the porosity of

the oxide layer that forms on its surface, we treated the aluminum with a cleaning process that has been shown to form a dense oxide layer, for superior vacuum performance[58]. With this aluminum treatment we achieve a base pressure of 2×10^{-9} torr. We ultimately achieve a count rate of almost 1 photon per shot of the experiment, however this signal was still too small to continue with LIF as a detection technique.

(2) Photodissociation

Our favored technique for molecule state detection is resonance-enhanced multiphoton dissociation. We employ two photons, the first tuned to a UV bound-bound transition of HfF^+. Depending on which state we wish to address, this photon has a wavelength of 277 – 286 nm, which promotes either the $^1\Sigma_0^+$ ground state or the metastable $^3\Delta_1$ state to an intermediate $\Omega = 0$ state. We are able to address this intermediate state transition with rotational selectivity, so this is suitable as a readout technique for a single rotational state of the molecular ion. In particular, the $^3\Delta_1, v = 0, J = 1$ rovibrational state can be selectively dissociated using this technique. A second photon then promotes the ion from the intermediate $\Omega = 0$ state to a repulsive state which dissociates into Hf^+ and F. Because Hf^+ is 10% lighter than HfF^+, it can be co-trapped in the ion trap. We may then use an electric field pulse to eject the ions from the trap onto an ion detector. With a large enough electric field kick the ion detector effectively subtends a 4π solid angle, allowing us to realize good detector efficiency compared to laser-induced fluorescence, where many optical elements were required to direct the photons onto the photon detectors. We are able to realize a single shot detection efficiency of 18%, which is about 200 times better than we were able to achieve using LIF. For more details please see [50].

2.2 Ion Trap

2.2.1 Refinements unique to the eEDM experiment

The ion trap we use for our precision spectroscopy has several differences from the standard "off the shelf" rf quadrupole trap. It is a custom design, unique to our group, where we have taken steps to optimize characteristics not commonly targeted in other ion trapping experiments. The qualities we wanted to optimize when designing the current generation ion trap were:

(1) application of additional rotating electric bias field.

(2) electric field homogeneity.

(3) fluorescence collection efficiency.

In addition to using the ion trap electrodes to apply a time-dependent electric field to confine the ions in the trap, we will use the ion trap electrodes to apply an electric field to polarize the trapped molecular ions. However, at the center of an ion trap the time averaged electric field must be zero, otherwise the ions must be accelerating. This complicates the application of a polarizing electric field because we cannot simply apply a static, uniform electric field. Instead we apply a rotating electric field and polarize the molecules in a rotating frame of reference. The electric potential to create this rotating field can be added to the electric potential used to create the rf quadrupole trap due to the principle of superposition. The application of this additional field will have various design consequences, discussed below.

We chose to optimize electric field homogeneity because we predicted that inhomogeneity of the trapping electric fields, and especially of the rotating bias field, would be a source of systematic errors[42]. Indeed, if we skip ahead to chapter 4 we will see that we observe several systematic shifts in the EDM measurement that we can attribute to inhomogeneity in the trap. There are several features of the trap that help optimize the electric field homogeneity.

- The trap is extremely large. Typical ion traps range in size from tens of μm between electrodes, as in the case for quantum information surface traps[65], to tens of mm, as in

the case of the multi-pole traps used to study ballistic collisions[30]. The distance between rf electrodes in our trap is 8 cm, making it probably one of the larger rf quadrupole traps constructed. Increasing the size of our ion trap allows us to increase the size of the homogeneous electric field region at the center of the trap. Additionally, with such a large trap architecture we are unlikely to experience the anomalous rf heating encountered in microscale surface traps[35].

- The trap does not have the standard four electrodes found in a conventional linear quadrupole trap design. We have instead opted for six electrodes, distributed radially around the trap at 60° intervals. This allows us to apply a more homogeneous rotating electric field by "smoothing" out the difference in electric field magnitude during a period of rotation. When the electric field points directly at an electrode it will be stronger than when it points at the space between two electrodes. This effect decreased as we crowded more electrodes in, but numerical simulations of the electric field show that operating with 6 is sufficient. We do not drive the six electrodes as a hexapole, but instead electrically short pairs of electrodes together and apply the voltage V_i to the i^{th} electrodes (where i runs from 1 to 6),

$$V_i = V_{\text{rf}} \sin(\omega_{\text{rf}} t) \cos(2\pi(i-1)/3). \tag{2.1}$$

- The trap has electrodes that curve in at the ends, as shown in fig. 2.2. The purpose of this is to compensate for the electrodes not being infinitely long in the axial direction. The curve was calculated to cancel the second order gradient of the rotating electric field in the axial direction using SIMION[19].

We optimized fluorescence collection efficiency because we initially planned laser-induced fluorescence to be our primary technique to read out the internal state of the molecules. As such, optics were designed into the trap to focus fluorescence from a 1 cm diameter region at the center of the trap to exit ports at the center of the axial endcaps. Light pipes directed the fluoresced light further out from the trap to photomultiplier tubes where the light could be collected. As fluorescence

Figure 2.2: Depicted is the design of the current ion trap. It has six linear electrodes, in contrast to the standard four, to provide more uniform rotating electric fields. The bottom axial endcap is shown, as well as the bottom half of the ellipsoidal reflector which focuses fluorescence from the center of the trap to the exit port at the center of the top endcap electrode (not shown). The top half of the ion trap, comprising the top ellipsoidal reflector and top endcap electrode are hidden in order to reveal the six linear electrodes.

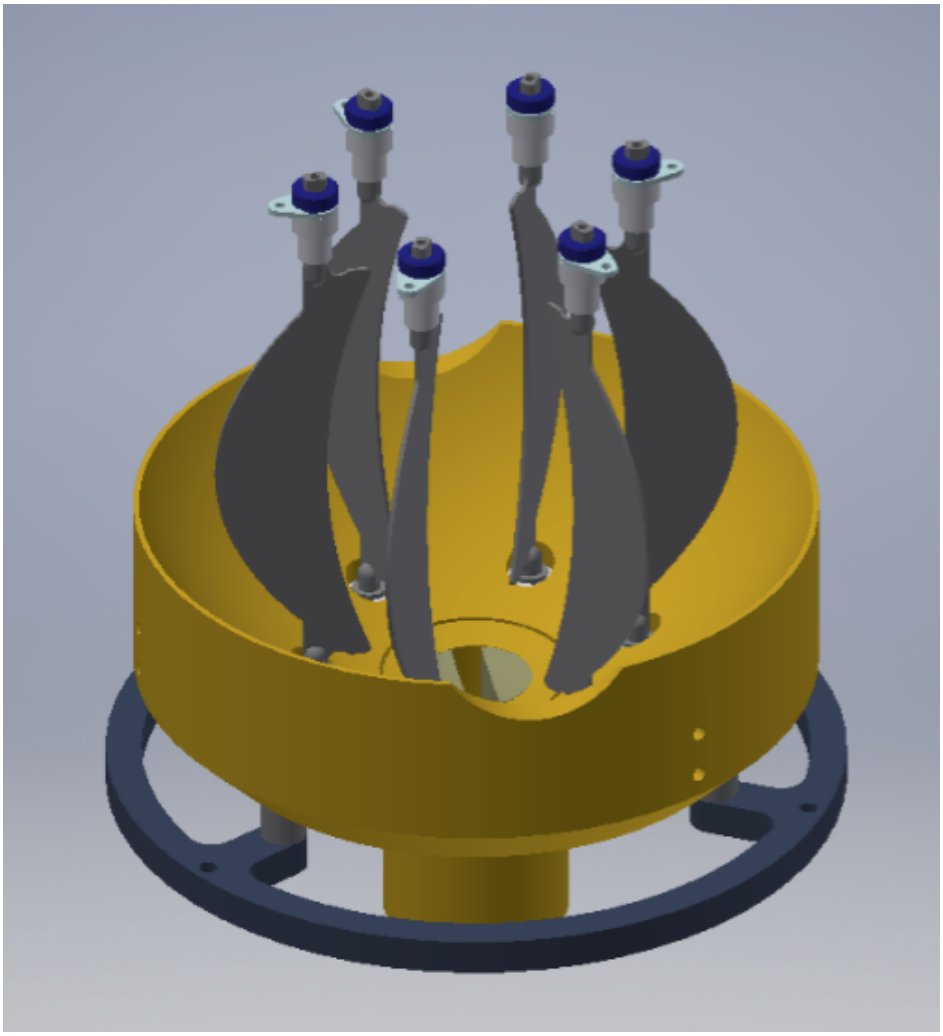

collection is no longer used in the experiment, these mirrors serve no purpose other than to help define the ground plane of the trap. If they were removed this would actually ruin the uniformity of the rotating electric field, but in future iterations of the ion trap we will redesign the shape of the electrodes to compensate for this.

2.2.2 Rotating electric field

To apply the rotating electric field we add the sinusoidal voltage V_{rot} to the rf quadrupole voltage V_{rf}, such that the voltage V_i on the i^{th} electrode (where i runs from 1 to 6) is

$$V_i = V_{\text{rf}} \sin(\omega_{\text{rf}} t) \cos(2\pi(i-1)/3) + V_{\text{rot}} \sin(\omega_{\text{rot}} t + 2\pi(i-1)/6). \tag{2.2}$$

We typically operate with $\omega_{\text{rf}} = (2\pi) \times 50$ kHz and $\omega_{\text{rot}} = (2\pi) \times 250$ kHz. Generating the V_{rot} drive for each of the six electrodes at six different phases requires some custom control hardware. The rf quadrupole drive is a sinusoid at frequency ω_{rf} that is π out of phase, which can be done with a simple inverting op amp. One potential way to generate the 60° phase offsets is to make low-pass filters with corner frequencies chosen to import the $60°, 120°, \ldots$ phase shifts necessary. This has several disadvantages. The first is that this will only work for one particular frequency, and there are various reasons explored in chapter 4 for why we would want to operate at a range of ω_{rot} frequencies. A second disadvantage is that such a circuit would be difficult to tune, and be susceptible to drifts which would cause the relative phases to wander, consequently contributing to inhomogeneity in $\mathcal{E}_{\text{rot}}$.

Our solution to this phase problem is to generate the V_{rot} signal using direct digital synthesis (DDS). DDS works by keeping track of a phase in time with a digital clock, and using a sinusoid look-up table to digitally generate a sine wave signal. We can construct six separate DDS units with synchronized clocks and program in the exact relative phase offsets. This has the advantage of having exact correct relative phase offsets for a range of frequencies, up to the digital precision, which is better than 0.03°. We use the popular Analog Devices AD9959 DDS, because it incorporates 4 separate DDS units onto one chip. This model DDS also comes on a convenient evaluation

board containing a microcontroller that can be used to program the frequency and phase of the DDS with a computer.

2.2.3 $\mathcal{E}_{\mathrm{rot}}$ amplitude pulses

When applying the rotating electric field it is important that we take care not to do so too quickly. Instantly turning $\mathcal{E}_{\mathrm{rot}}$ on or off will accelerate the trapped ions to one direction, causing excess trap slosh and heating. To solve this problem we turn on the rotating electric field gradually over the period of many, typically 50, rotations. Additionally, we use fast amplitude ramps of the rotating electric field to apply $\pi/2$ pulses for Ramsey spectroscopy, as explained in section 3.2.3. This requires some technology to control the amplitude of the sinusoidal voltage that we apply to the ion trap to generate $\mathcal{E}_{\mathrm{rot}}$.

We initially designed a board with 6 voltage controlled amplifiers (analog devices AD8337), allowing us to control the amplitude of our applied $\mathrm{V_{rot}}$ with a single voltage generated by an arbitrary waveform generator. However, the voltage controlled amplifiers are not really variable amplifiers, they are variable attenuators with a built-in +18dB amplifier. This has two consequences, the first being that we get extra noise from the extra built in attenuator, and the second that we are limited in the contrast we can achieve. We would like an amplifier that operates between 0dB (unity gain), and $-\infty$ dB (fully off). This architecture seems typical for packaged voltage controlled amplifiers, which seem to be designed for use in modulating cellphone transmission signals. When tested in the ion trap, this design produced too much excess ion slosh due to the lack of a full off and the additional noise of the built in amplifier.

We quickly designed an alternative amplitude control board using multiplying DACs. Multiplying DACs are typically very fast digital to analog converters that can operate with a variable voltage reference, instead of the conventional DAC design with a constant voltage reference and a variable analog output defined by the digital inputs. A multiplying DAC can essentially be thought of as voltage divider and a set of very fast switches. When all the digital inputs are high, the switches are closed and the voltage divider is bypassed, and the output voltage is equal to the

reference voltage. When all the digital inputs are low, the switches all open and the voltage output is shorted to ground. In this sense the output of the DAC, $V_{out} = V_{ref} \times x$, where x is an unsigned integer defined by the the digital inputs. The advantages of this method are that it is capable of perfect contrast, by programming the value of 0 to the DAC, and it doesn't include any additional noise due to amplification.

The design of the amplitude control boards is shown in fig. 2.3 and fig. 2.4. The essential component is the AD5433 10 bit multiplying DAC, which has a 10 MHz bandwidth and an update rate of 20Mbps, which is ideal for our application where the frequency of $\mathcal{E}_{\text{rot}}$ will typically be 250 kHz. By using a DAC instead of a voltage controlled amplifier we have made the control problem an order of magnitude more difficult, because instead of one analog control voltage we now require 10 digital controls. We used a fast ARM Cortex-M3 microcontroller running at 72 MHz seated on the same PCB as the multiplying DACs. This microcontroller should in principle be capable of switching a digital output with a period of 28 ns, which means it could run through the sequence to either fully ramp up or ramp down the 10 bit control to the DAC in 28 μs. However, the microcontroller has a more complicated task than simply producing square waves: it must output a sequence of pulses on 10 separate channels that count up or count down an integer. This requires storing the value of the integer in the microcontroller memory, performing arithmetic to increment or decrement the integer, indexing a loop, and conditional statements to check if the ramp has finished. All of these have overheads of several clock cycles. In order to reduce the overhead as much as possible while still retaining flexibility we use the interrupt function of the ARM microcontroller to ensure that our code is executed immediately and does not suffer overhead from other microcontroller functions (such as communicating with the main experiment control computer). In order to not perform the condition check of whether to increment or decrement the integer every loop iteration, we only perform unidirectional ramps; 6 interrupts will ramp up and 6 interrupts will ramp down. An example of an interrupt ramping down follows:

```
1 void ramp1()
2 {
3   int a = begin1;
```

Figure 2.3: The multiplying DAC variable attenuator is designed to accept both the true and complementary current outputs of the DDS DAC channel. The currents are converted into a voltage and buffered with a differential amplifier (U3). The differential output is fed into the VREF of a AD5433 multiplying DAC. Digital lines D0-D9 represent a 10bit unsigned integer that is effectively multiplied by VREF, thus programming 1023 into lines D0-D9 will pass the input at VREF to the output at full scale, 512 will output it at half scale, and 0 will turn the output off. The digital lines D0-D9 come from the outputs of an ARM Cortex-M3 microcontroller buffered by three 74HC125 quad TTL buffers. The sub schematic from IN1 to OUT1 is repeated 6 times, for each of the trap DDS channels, but is driven in parallel by the same digital lines to ensure that all DDS channels have the same multiplicative attenuation. Inputs TTL1 through TTL13 are connected to interrupt pins on the ARM microcontroller, which is programmed to initiate various ramp sequences when it detects a rising edge on one of these channels.

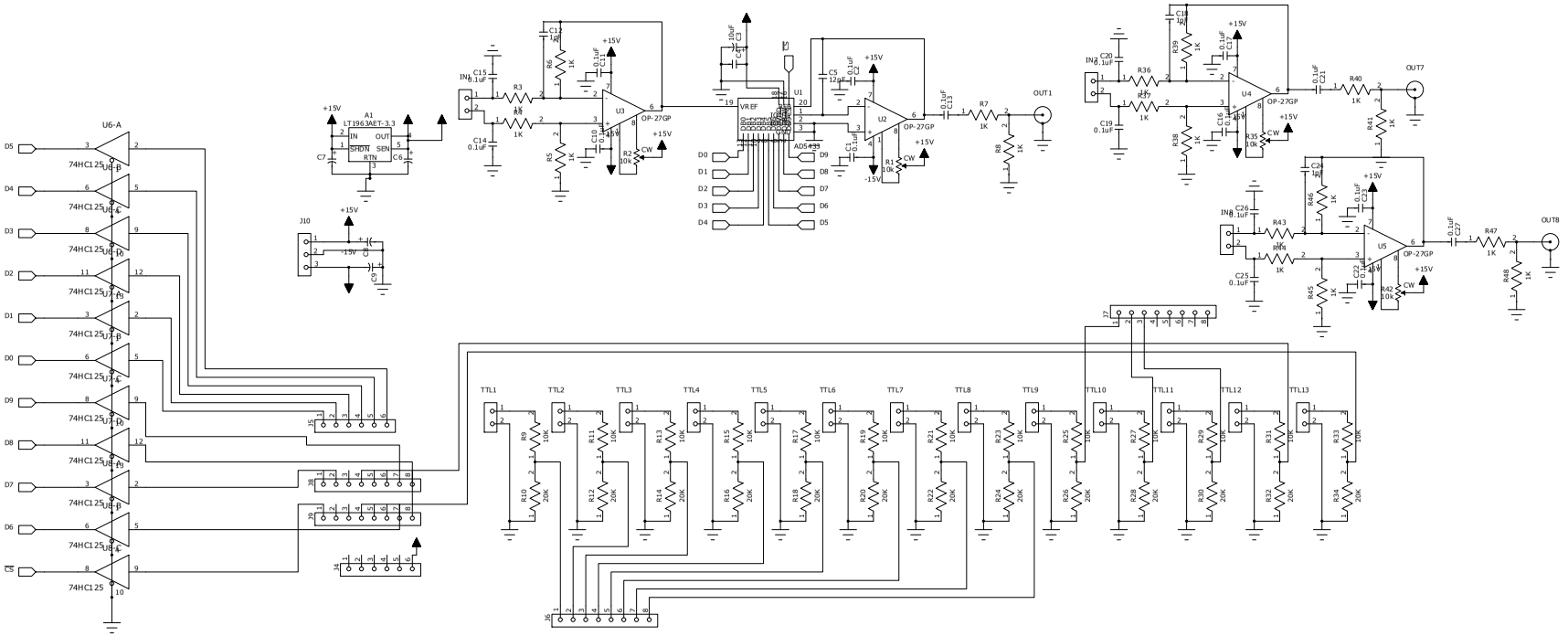

Figure 2.4: The multiplying DAC variable attenuator has 6 parallel channels OUT1-OUT6 which attenuate the current output of a DDS channel by a factor specified by a programmable 10 bit unsigned integer. The 10 bit unsigned integer is supplied by a ARM Cortex-M3 microcontroller on a Maple hobbyist board developed by Leaf Labs, and headers J4, J5, J6, J7 and J8 are designed to interface with the Maple board. Channels OUT7 and OUT8 are identical to OUT1-OUT6 with the exception of the multiplying DAC hardware, they simply provide a differential buffered output to the remaining two DDS channels. Through efficient microcontroller software design this board is capable of ramping the DDS output amplitude smoothly through the full 1024 bit range in 100 μs.

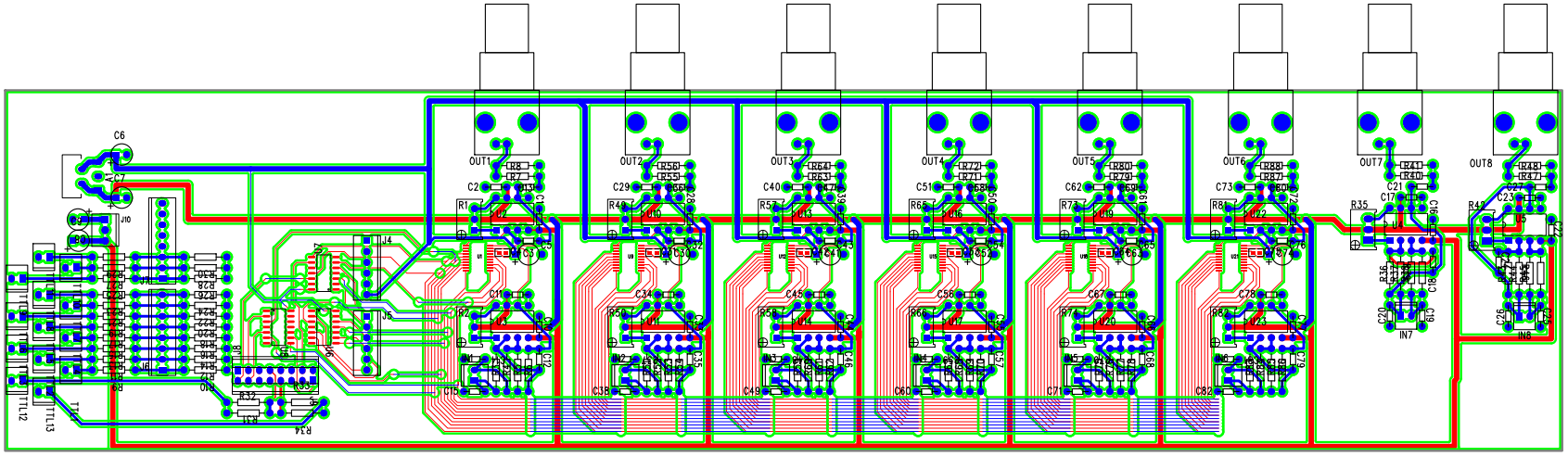

```
4   int b = end1;
5   int c = step1;
6   for (int i=a; i>b; i-=c)
7   {
8     GPIOC->regs->ODR = i;
9     GPIOC->regs->BSRR = 1<<15;
10  }
11  GPIOC->regs->ODR = b;
12  GPIOC->regs->BSRR = 1<<15;
13 }
```

The code `GPIOC->regs->ODR = i;` allows us to write the bits of the integer `i` to the register `ODR` in a single clock cycle, rather than 10. This requires careful PCB layout to ensure that the output pins of the register correspond to the correct digital input pins of the multiplying DACs. The code `GPIOC->regs->BSRR = 1<<15;` makes one bit of the BSRR register high to latch the DAC. This allows us to increment the values of the DAC once every 8 clock cycles, or equivalently, perform a full ramp in 100 μs. In a typical experiment sequence we might ramp $\mathcal{E}_{\text{rot}}$ on to full, and then pulse it down to 25% of its value and back up to perform one $\pi/2$ pulse, pulse it down and up again 100 ms later for the second $\pi/2$ pulse, before finally ramping $\mathcal{E}_{\text{rot}}$ down to zero at the end of the experiment. This requires triggering 4 different interrupts on the microcontroller 6 times, e.g. in the sequence $\{2, 3, 4, 3, 4, 1\}$, and programming the thresholds `begin_i` and `end_i` on each beforehand. This is easily done using the fast digital timing card that sequences the experiment.

2.2.4 Experiment sequence

The experiment is timed by a special purpose timing card designed by Viewpoint Systems. The card is at its core an FPGA that has a 32×512 bit memory bank containing timestamps and a 64×512 memory bank containing digital output line states. After receiving a trigger the FPGA increments a counter every cycle of a 10 MHz external clock, comparing the counter to an entry of the timestamp memory bank indicated by a pointer. Once the counter matches a timestamp the corresponding row of the output memory bank is latched to the outputs and the pointer is incremented such that it points at the new row of the timestamps memory bank. This allows the timing card to specify pulses as narrow as 100 ns spaced as much as 7 minutes apart. This is

ideal for an experiment such as ours that lasts for no more than several seconds and rarely requires timing precision better than 100 ns. Compare this to the more typical configuration found on many computer controlled DACs that simply playback from memory 1 sample per clock cycle, and as such are typically limited to experiment times no greater than the product of the resolution and the number of samples that can be stored in memory.

Additionally, the timing card can be reprogrammed by transferring several kB of data at a time. This is because of its efficient nature at representing sparse pulse sequence. To reprogram the same pulse sequence on a traditional DAC we would have to transfer several GB of data, because we must specify the dead time between pulses. A potential disadvantage of this specific timing card is that Viewpoint Systems is all but no longer supporting it. While they are still available for sale, it is increasingly difficult to make them run on newer computer systems. A potential solution is internal development of a new timing board. We currently have prototype designs of a timing sequencer that can run on a Xilinx FPGA and should replicate the features described above, although due to improvements in FPGA technology since the design of the Viewpoint card it is possible to store more than 512 pulses in memory. This new timing board design can communicate with computers using the standard RS232 protocol over USB2.0 at several MB/s, and could potentially be extended to even higher speeds using PCIe.

The timing sequence for a typical Ramsey experiment is shown in fig. 2.5. There are primarily three sets of things sequenced in the experiment: lasers, trap electronics, and the rotating electric field. Timing pulses fire the Q-switch of the ablation laser to produce neutral molecules, open shutters to allow the two transfer lasers to irradiate the ions, pulse on the amplifier to the AOMs that shutter the depletion pulse train, and open the shutter for the 266 nm laser that dissociates the ions. In synchrony with this, various pieces of electronics attached to the ion trap driver receive pulses to increase confinement of the ion trap in the radial direction to overlap the ions with the transfer lasers, then to relax the trap to suppress collisions during the Ramsey experiment, and finally to compress the ions so that the 266 nm laser can be focused on them during dissociation. Pulses are also sent to the rotating electric field amplitude modulator described in section 2.2.3 to ensure the

rotating electric field is at one value for transfer, is at another value for the Ramsey experiment, and is pulsed to a lower value to apply $\pi/2$ pulses before and after the Ramsey experiment.

2.2.5 Future trap directions

The current ion trap has been very useful for the study of EDM systematics and in demonstrating the rotating electric field technique. It does have some minor shortcomings, which we hope to correct in a 3$^{\text{rd}}$ generation version ion trap. Perhaps the most immediately obvious when looking at the trap is that it was designed to be optimized for fluorescence collection, which is no longer used in the experiment. This design constraint dictated much of the shape of the current trap. As discussed in chapter 4 it has also become clear that trap is not as uniform as we would like, and this can potentially be improved by revisiting the shape of the trap electrodes, the number of electrodes, and the size of the trap itself. Finally, the trap vacuum chamber and electrodes were fabricated from stainless steel, which while nominally nonmagnetic, might perhaps be magnetic enough to be a source of potential systematic errors, see section 4.2.3. Indeed, the table upon which the experiment rests is also made of stainless steel. This could be replaced by a skeleton structure made of extruded aluminum, which in addition to being nonmagnetic might provide easier access to parts of the experiment.

2.3 Computer control

Sophisticated computer control of experiments is very commonplace in the field of physics in this day and age. While every experiment has its own peculiarities, there are a few interesting features of our experiment control that are worth mentioning, because their complexity requires some documentation, and also because they might be useful in general.

2.3.1 uBinary file format

In the EDM experiment we record photo-dissociated ion counts using a digital oscilloscope. A single shot of the experiment corresponds to a single trace of the oscilloscope which is 2500

Figure 2.5: Experiment timing pulses for a typical run of a Ramsey fringe experiment.

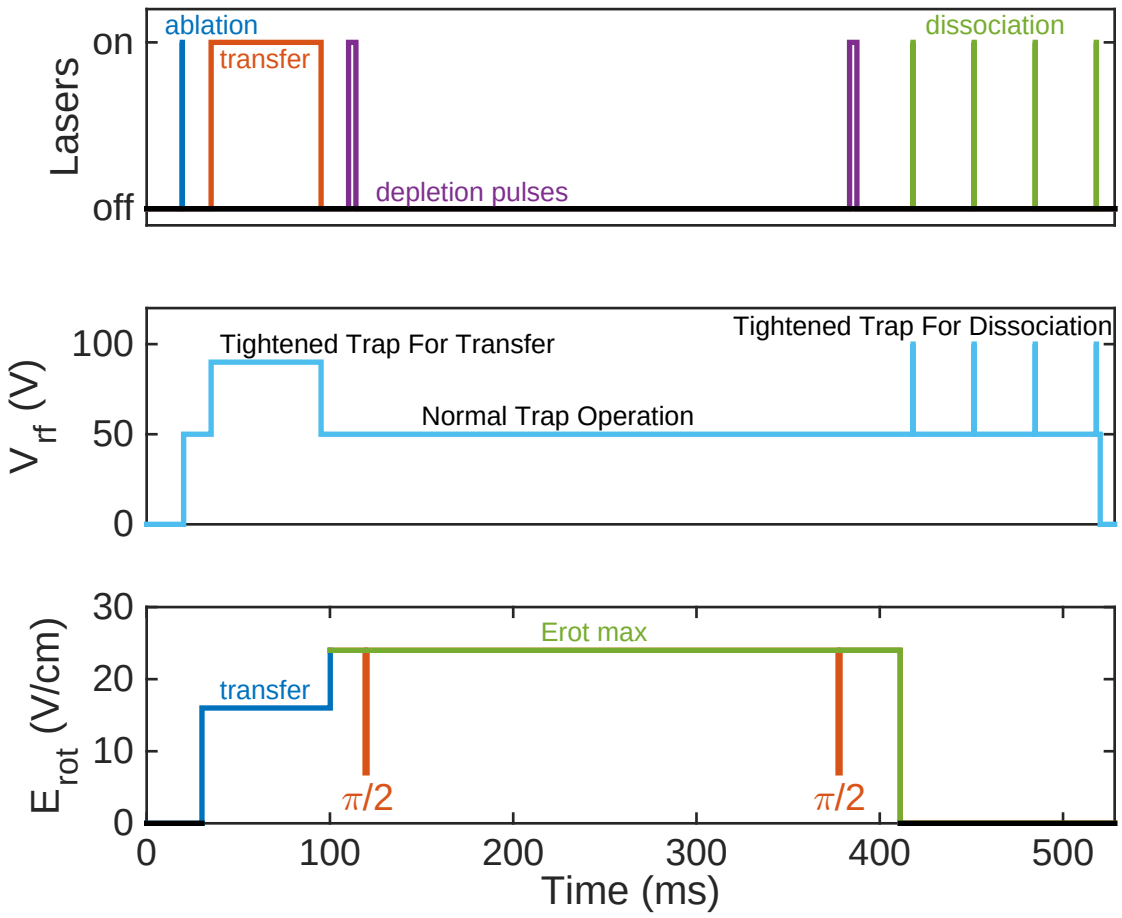

double precision floating point numbers, which if taken at a rate of 2 Hz is a modest data rate of about 40 kB/s. A precision measurement of the electron EDM will require about 100 hours of data, or more than 14 GB. Additionally, this 100 hours of data will be taken under a large number of deliberately varied experimental conditions, and we will want to track these along with the raw oscilloscope data. We need to store the data in some manner that is consistent, unambiguous, and reasonably compact. For example, a large text file with lists of human readable numbers and a text header describing each section is reasonably unambiguous, but it is not very compact. A large text file is about a factor of 10 times larger than the minimal machine binary representation of the data (140 GB), and the time to read or write data to disk will be similarly increased. Moreover, there is the additional overhead of parsing the text to and from machine data whenever the data is stored or retrieved. Conversely, a pure machine binary representation of the data will be very efficient in terms of storage space and read/write times, but will be completely unintelligible to a human reader. Additionally, both data formats are inflexible to changes in the sets of parameters we wish to store in the data file. If, for example, we increase the resolution of the oscilloscope to 10000 points per trace, or if we wish to also begin tracking the relative humidity in the lab, this will require changes made to the computer code that reads and writes the data to disk.

Our solution to these problems is to design a new data file format unique to our experiment. The file format is self descriptive so that it can remain flexible to changes in the quantity of type of data contained, and it is in machine binary so it can be efficiently stored and retrieved to disk. Even though it is in a binary format it is still suitable for archival purposes due to its self descriptive header. There are similar existing file formats, such as the Hierarchical Data Format (HDF)[71] developed by the NCSA, or the Common Data Format (CDF)[68] developed by NASA. These were considered, but ultimately rejected due to their complexity and lack of suitable libraries for the software environments we were currently using at the time.

We refer to this file format as “uBinary”, which is short for Universal Binary, because it allows us to store, retrieve, and manipulate our data in a platform independent manner while still taking advantage of the speed and compactness of a binary format. In particular it allows us to

share data between the MATLAB and LabView platforms, our choice platforms for data analysis and data acquisition. A description of the file format is outlined in table 2.2, with the relevant data types enumerated in table 2.1. The file has gone through several iterations, but the most current, used in all the data presented in chapter 5, is the 4^{th} iteration. All versions at their core share the same structure, but the newer versions divide data in ways to make it more easily searched.

Table 2.1: uBinary data types

Type	**MATLAB**	**LabVIEW** (G)
1	`int8`	`int8`
2	`int16`	`int16`
3	`int32`	`int32`
4	`int64`	`int64`
5	`uint8`	`uint8`
6	`uint16`	`uint16`
7	`uint32`	`uint32`
8	`uint64`	`uint64`
9	`single`	`single`
10	`double`	`double`
22	`uint16`	`enum`
23	`uint32`	tab control
33	`logical`	`bool`
48	string	string
50	string	path
51	string	text picture
55	string	DAQmx resource
64	array	array
80	`struct`	cluster
84	waveform	waveform
112	string	VISA resource

The first 18 bytes of the uBinary format is the string "@@@@@uBinary4}}}}}", identifying it as a file with a format described in table 2.2. Next is a 4 byte integer that describes how many "chunks" the file contains. Each chunk contains 4 parts:

(1) the name of the chunk.

(2) a list of strings called `names`, naming the data in the chunk.

Table 2.2: uBinary file format specification

Field	Description	Type	Value
file header			
`filetype`	string to identify file as ubinary4	`char[18]`	ubinary4
`N_chunks`	number of chunks of data	`uint32`	
list of `N_chunks` *data chunks*			
`name_len`	length of chunk name	`uint32`	
`chunk_name`	name of the chunk	`char[name_len]`	
`N_name`	length of list of chunk element names	`uint32`	
`names`	names of the chunk elements	**string**`[N_name]`	
`N_type`	length of list of chunk element types	`uint32`	
`types`	types of the chunk elements	`uint8[N_type]`	
`N_data`	size of chunk data	`uint32`	
`data`	chunk data	`uint8[N_data]`	
format of `data` *is defined by parsing through* `types[i]`*. Each parsed element has a name in* `names[j]`*. The number of elements in* `types[]` *and in* `names[]` *may be different, so they must be parsed through in order. For fields and values that reference* `types[]` *and* `names[]`*, these are parsed from those arrays, and not from* `data`*.*			
`types[i]`	**string**		48
`str_name`	name of the string	**string**	`names[j]`
`str_len`	length of the string	`uint32`	
`str_data`	string data	`char[str_len]`	
`types[i]`	**array**		64
`dims`	number of array dimensions	`uint8`	`types[i+1]`
`e_type`	type of array element	`uint8`	`types[i+2]`
`array_name`	name of the array	**string**	`names[j]`
`N_array[dims]`	size of each array dimension	`uint32[dims]`	
`array_data`	array data	`e_type[`$\prod_n$`N_array[n]]`	
$\prod_n$`N_array[n]` *array elements must be parsed from* `data[]`			
`types[i]`	**cluster**		80
`N_cluster`	number of elements in cluster	`uint8`	`types[i+1]`
`cluster_name`	name of the cluster	**string**	`names[j]`
`N_cluster` *cluster contents types and names must be parsed from* `types[i+2:...]` *and from* `names[j+1:...]`			
`types[i]`	type in table 2.1		1 – 33
`name`	name of the data element	**string**	`names[j]`
`element_data`	data element	`types[i]`	
`N_cluster` *cluster contents types and names must be parsed from* `types[i+2:...]` *and from* `names[j+1:...]`			

(3) a list of `types` describing the data in the chunk.

(4) the `data` in the chunk.

Each of these 3 parts is preceded by a 4 byte integer describing the length of each list in bytes. This allows for chunks to be easily skipped over if we wish to only read or write to a single chunk. As an interesting historical note, with the chunk name and the integer describing the data length removed, a chunk is actually the first iteration of uBinary. Once the `data` from a chunk is read in it must be parsed, according to the prescription in the bottom part of table 2.2. This is done by iterating through the list `types`, an array of 8 bit integers. These numbers enumerate the type of the `data` to be parsed, and are listed in table 2.1. For example, if the next integer parsed off the list `types` is `10`, this means that the next parcel of `data` is an 8 byte double. We then remove 8 bytes from `data`, typecast it as a double, and label it with the next string parsed off of the list `names`. The matter is more complicated for the composite types of **string**, **array**, and **cluster**. These require recursive parsing. For example, a cluster might contain 3 elements, a double, a 32 bit integer, and another cluster containing two 8 bit integers. The list of types describing this scenario would be `[80 3 10 3 80 2 1 1]`: `80` for the cluster, `3` for the three elements, `[10 3 80]` for `double`, `int32`, and **cluster**, and then finally `2` for the two `int8`s each specified by `1`.

Currently we have software libraries to read and write uBinarys in LabVIEW, our data acquisition platform, and to read and write uBinarys in MATLAB, our data analysis platform. In principle this can be extended to other languages as well. For example, preliminary code exists to read uBinarys in Python, and libraries for other software environments can be implemented as needed. The peculiarities of the format are due to it being based around the format LabVIEW uses for storing its own data types internally, which we pieced together from some small amounts of documentation and trial and error. Because it is based on the LabVIEW internal data format, all data in the uBinary file is stored in the big-endian[69] byte order, with the most-significant byte stored in the first indexed memory address. Because of this relationship with the internal LabVIEW data format we can very easily generate uBinary files by using the LabVIEW built in

function “Flatten To String” to generate the binary data. By iterating through all controls in a LabVIEW program by reference we can automatically save every parameter in our LabVIEW control program using the uBinary data, as shown in fig. 2.6. The top level LabVIEW experiment control has 368 independent controls that can be written along with data to a uBinary file in under 80 ms. This time is primarily limited by how long it takes to parse the data to be saved and construct the appropriately descriptive header. Additionally, a uBinary file can be loaded back into the data acquisition program, effectively allowing us to reset the experiment parameters to match that of any recorded set of data.

2.3.2 Experiment control state machine

We choose to work with two separate software environments, LabVIEW for data acquisition, and MATLAB for data analysis, to exploit the separate strengths of each system. The LabVIEW development environment, based on the graphical G data-flow based programming language, is well suited for quick and easy production of experiment control graphical user interfaces. Additionally, LabVIEW is produced by National Instruments (NI), an industry leader in the production of data acquisition and control hardware, and programmatically interfacing with these devices is made extremely simple using NI’s libraries. Conversely, MATLAB was designed with scientific computing in mind, and is well suited for performing arbitrarily complex analysis on data. While either system could be used for both tasks, it typically is much more tedious, e.g. designing a GUI in MATLAB to control a complex device might take roughly ten times longer, and that time could be better used serving the needs of science.

During the course of an EDM measurement we will want to interweave various different types of data, such as periodically taking trap slosh measurements to check the position and oscillation amplitude of the ion cloud in between Ramsey fringe measurements. To achieve this goal we need a flexible computer control scheme that allows us to perform many different types of experiments in arbitrary sequence without having to retool large portions of the experiment control code. We use a state machine with about 140 different states corresponding to sending various types of commands

Figure 2.6

(a) ubinary_save.vi – This subvi works by assembling a list of references to every control in the program (via All Refs subvi). It parses out those controls which cannot be saved, either because we do not wish to save them, or because they cannot be accessed via reference due to race conditions (e.g. latching boolean controls). It iterates through these control references, first writing the Label.Text as the chunk name, then writing the list of control names and types returned from the uBin Single subvi, and finally writing the value of the control, accessed by reference.

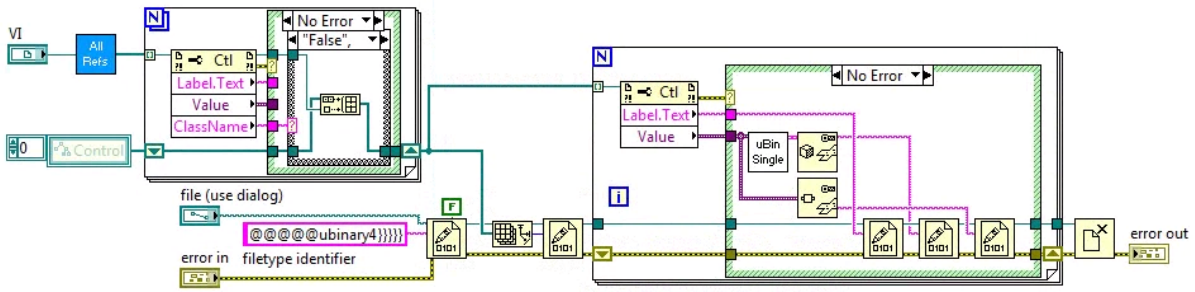

(b) ubinary_load.vi – This subvi reverses the hard work done by ubinary_save.vi. It reads in a uBinary file, checking first that the header string matches the expected "@@@@@ubinary4}}}}}", and then iterates through the chunks of the file. For each chunk it checks to see if the chunk name matches an entry in the list of control references returned by All Refs. If it does discover a match, then it will try to typecast the chunk data to the type of the matching control. If this typecast succeeds then it inserts the chunk data into the control, otherwise it quietly returns an error and continues iterating. This subvi also has the optional input of "control", allowing us to specify a single control to match to. This is useful if we wish to use a uBinary file to roll back changes to a single control, such as the DAC voltages, while leaving the whole of the experimental parameters unchanged.

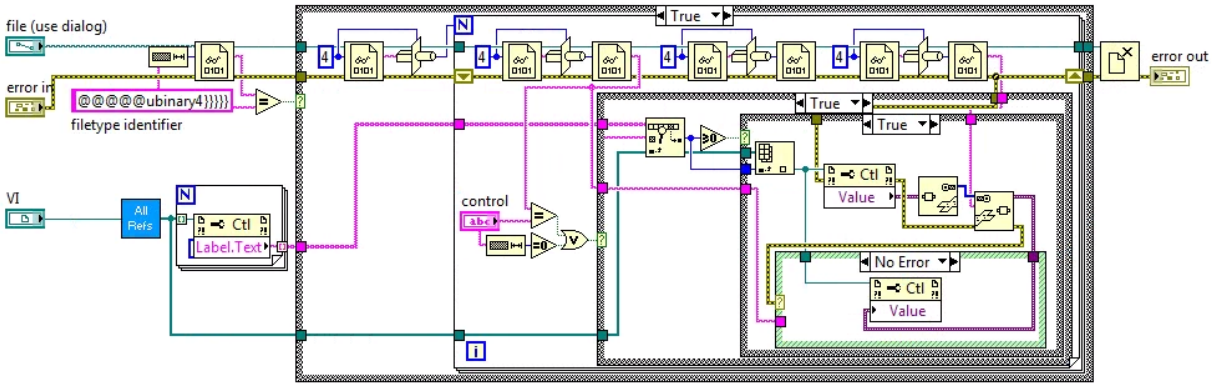

to pieces of acquisition or control hardware, e.g. "Scope: Read" or "TrapDDS: Upload". By specifying a short sequence of states we can efficiently describe an experiment sequence, as in the following case describing a sequence to measure ion trap slosh on two different ion detectors:

```
Frames >> 1,1
Scope: Settings >> TDS5034B
Scope: Trigger Settings >> TDS5034B
Trap DDS: Upload

DAC: Upload2 >> 1,Fast
Scope: Start >> TDS5034B
DIO64: Prepare >> 5
DIO64: Run
Scope: Read >> TDS5034B
Scope: Stop >> TDS5034B
Scope: Display Traces >> TDS5034B
Count Ions

IMG MCP: Clear
DAC: Upload2 >> 1,IMG
DIO64: Prepare >> 6
MV500: Trigger
Wait >> 50
DIO64: Run
MV500: Read
Count Ions
```

In principle such a state machine is Turing complete and capable of arbitrary computation, but this would be tedious, especially given the number of already existing scripting languages with much more well thought out control flow. We chose the MATLAB language as the master arbiter of the control flow of the state machine, as we were already using it for data analysis. Given an appropriate interface layer between the LabVIEW state machine and MATLAB, we can script experiments in the MATLAB language, taking full advantage of that language's control flow features, function stack, and numerical analysis techniques.

Because of the flexible nature of the uBinary file format it is well suited for use as a serialized format for real time communication between LabVIEW and MATLAB. By creating a parallel thread of execution within the LabVIEW state machine we can implement a TCP server that listens for communications requests from clients. MATLAB can talk to this TCP server and manipulate the status of the state machine queue by adding states to the front or back. In other words, MATLAB commands LabVIEW via TCP to execute a particular set of commands to communicate with

hardware and collect data before turning over control back to MATLAB. Additionally, the uBinary data format can be used to pass experiment control parameters and measurement data between LabVIEW and MATLAB. This allows MATLAB to instruct the LabVIEW to make a sequence of measurements, request the data and analyze it, and then in real time make some decision about what nature of experiment to run next. This blurring of the boundaries of data acquisition and data analysis allows us to create very sophisticated experimental control sequences, where for example we record EDM data until the contrast of our Ramsey fringe begins to fall, at which point the data analysis can identify the decrease in contrast and add some diagnostic sequences to the queue, make a decision, and correct.

The experiment control TCP server runs on port 8888, and it listens until a TCP request is made. Once communication is initiated it expects one `uint32` describing how many bytes will follow. It then parses these bytes for text strings, recognizing the following commands:

(1) “commands” - will return an array of strings containing all of the available states of the state machine.

(2) “documentation” - will return an array of strings containing the documentation of the available states of the state machine.

(3) “controls” - will return an array of strings containing the names of all of the available controls in the data acquisition program.

(4) “type” - will attempt to read a string, match that string to a control, and return an array of names and types as specified by table 2.2 describing how to parse the uBinary data chunk associated with that control.

(5) “read” - will attempt to read a string, match that string to a control, and return the uBinary data of that control.

(6) “write” - will attempt to read a string, match that string to a control, and then read uBinary data and load that into that control.

(7) “sync” - will wait until the state machine reaches the state “Sync”, and then return a `1`.

Additionally, if a string is not recognized as a command it will try to load this onto the back of the state machine queue. The state machine is robust to unrecognized states, removing them from the queue when they reach the front, and passing a descriptive error to a text control facing the user.

Chapter 3

Statistical sensitivity

3.1 Theory of measurement

3.1.1 Measurement principles

The electron EDM manifests as a torque on an electron spin due to the interaction with an electric field. Much like the interaction of the magnetic moment with the magnetic field, the electron EDM d_e, appears in the Hamiltonian as the energy shift $-2d_e\vec{S}\cdot\vec{E}$, where $\vec{S}$ is the spin of the electron. The Hamiltonian for an electron in and electric and a magnetic field is

$$H = -\left(g_S\mu_B\vec{B} + 2d_e\vec{\mathcal{E}}\right)\cdot\vec{S}, \tag{3.1}$$

where μ_B is the Bohr magneton and g_S is the electron spin g-factor. To measure the $2d_e\mathcal{E}$ term we can perform spectroscopy between the two spin states. This alone is not sufficient to accurately measure $2d_e\mathcal{E}$, because under typical conditions $2d_e\mathcal{E} \ll g_s\mu_B B$, and any small deviation from the expected value for the measured energy could be attributed to uncertainty in magnetic field. We can improve this by making one measurement for the energy between the two spin states, reversing the direction of electric field $\vec{\mathcal{E}}$, and then making a second measurement. In this differential measurement the uncertainty in B drops out, and half the difference of the two measurements is $2d_e\mathcal{E}$.

3.1.2 $^3\Delta_1$ state Hamiltonian

To achieve the best upper bound on the EDM it is imperative to amplify the effect of $d_e\mathcal{E}$ in the experiment as much as possible. To provide the largest possible energy shift for a finite EDM we strive to apply the largest electric field possible. The largest electric field that is feasible to apply with parallel plates in a vacuum is < 1 MV/cm[73], typically somewhere before this point microscopic surface roughness causes breakdown to occur in vacuum. Classes of diatomic molecules have internal electric fields[62, 16] potentially as large as ~ 100 GV/cm[47]. Our molecule of choice is HfF^+. In the $^3\Delta_1$ electronic state of HfF^+ one of the valence electrons experiences an effective electric field of $\mathcal{E}_{\text{eff}} = 23.3$ GV/cm[48, 51, 52, 26]. An electric field of this magnitude will cause a 1.13 mHz energy shift between the $m_F = +3/2$ and $m_F = -3/2$ stretch states of the $J = 1, F = 3/2$ hyperfine level. As we will see in later sections, this size energy shift is challenging to measure, but is technically feasible.

We can write down the approximate Hamiltonian for the $^3\Delta_1$ state of the HfF^+diatomic molecule using *Brown and Carrington*[11] as a template,

$$H^{^3\Delta_1} = H_e + H_{\text{vib}} + H_{\text{rot}} + H_{\text{HF}} + H_{\Lambda D} + H_{\text{Stark}} + H_{\text{Zeeman}} + H_{\text{EDM}} \ldots, \tag{3.2}$$

where H_e is the electronic contribution, H_{vib} describes the molecule vibration, H_{rot} describes the molecule rotation, H_{HF} is the hyperfine interaction with the fluorine nucleus, $H_{\Lambda D}$ is the Λ-doubling interaction, H_{EDM} is the possible contribution from the electron EDM, and the other terms describe interactions with external fields. We will restrict ourselves to eigenstates of $H_e + H_{\text{vib}} + H_{\text{rot}}$, in particular $^3\Delta_1, v = 0, J = 1$. In the $^3\Delta_1$ state $|\Sigma| = 1, |\Lambda| = 2$, and $|\Omega| = 1$, where Σ, Λ, and Ω are the projections of $\vec{S}, \vec{L}$, and $\vec{J}$ on to the internuclear axis. Within this manifold of states there is both hyperfine and Λ-doubling structure. The fluorine nucleus has a spin $I = \frac{1}{2}$, which enters into the H_{HF} term and provides an energy splitting of $E_{HF} = -46.6(1)$ MHz between the $F = 1/2$ and $F = 3/2$ states ($\vec{F} = \vec{I} + \vec{J}$). A Coriolis type effect mixes states of opposite sign Λ. Perturbations with nearby electronic states creates a splitting between $\Omega = +1$ and $\Omega = -1$ states that is $E_{\Lambda D} = 740(40)$ kHz. A diagram of the states in the $^3\Delta_1, J = 1$ manifold is shown in fig. 3.1.

In the presence of an applied external electric field a $H_{Stark} = \vec{d}_{\rm mf} \cdot \vec{E}$, where $\vec{d}_{\rm mf}$ is the molecule frame dipole moment. For HfF^+ this is $d_{\rm mf} = 1.411(6)\, e\, a_0$. At energies where $d_{\rm mf}\mathcal{E}_{\rm lab} \gg E_{\Lambda D}$ the molecule is completely polarized, and there is a $2E_{\rm Stark}$ energy splitting between states of different $|F, (m_F\Omega)\rangle$,

$$E_{\rm Stark} = -m_F\Omega\gamma_F d_{\rm mf}\mathcal{E}_{\rm lab}, \tag{3.3}$$

where $\gamma_F = 1/3$ for $F = 3/2$ and $\gamma_F = 2/3$ for $F = 1/2$. In the $F = 3/2$ manifold of states this yields four states with a positive $E_{\rm Stark}$,

$$|F = 3/2, \Omega = -1, m_F = +3/2\rangle\,,$$
$$|F = 3/2, \Omega = -1, m_F = +1/2\rangle\,,$$
$$|F = 3/2, \Omega = +1, m_F = -3/2\rangle\,,$$
$$|F = 3/2, \Omega = +1, m_F = -1/2\rangle\,,$$

and four complementary states where $m_F\Omega > 0$ and $E_{\rm Stark} < 0$. We refer to the states with $E_{\rm Stark} > 0$ as the **upper** manifold of states, denoted with u superscripts, and those states with $E_{\rm Stark} < 0$ as the **lower** manifold, denoted with l superscripts.

The application of an external magnetic field gives rise to a $H_{\rm Zeeman} = -\vec{\mu} \cdot \vec{B}$ term in the Hamiltonian. The Zeeman effect can be very complicated, so we will only discuss the leading terms for now. They are:

$$H_{\rm Zeeman} = ((g_L + g_r)\gamma_F\Lambda\Omega + (g_S + g_r)\gamma_F\Sigma\Omega - g_r\gamma_F J(J+1) - g_I k_F)m_F\mu_B B. \tag{3.4}$$

The contributions to the Zeeman Hamiltonian from nuclear spin (g_I) and molecule rotation (g_r) are small, suppressed by the ratio of the mass of the electron to the mass of the molecule ($< 10^{-3}$). This leaves the terms

$$H_{\rm Zeeman} = (g_L\Lambda + g_S\Sigma)\gamma_F m_F\Omega\mu_B B = g_F m_F|\Omega|\mu_B B. \tag{3.5}$$

For an ideal $^3\Delta_1$ molecular state $\Lambda = \pm 2$, $\Sigma = \mp 1$, and $\Omega = \Lambda + \Sigma = 1$. Considering that the orbital angular momentum g-factor is $g_L = 1$ and the spin angular momentum g-factor is $g_S \approx 2 + \alpha/\pi$,

Figure 3.1: The state diagram of the 12 states contained in the $^3\Delta_1, J = 1$ manifold. In the absence of any external electric or magnetic fields the states are denoted by dashed lines. The $F = 1/2$ and $F = 3/2$ states are split by the hyperfine energy E_{HF}, and within each hyperfine level is a Λ-doublet split by $E_{\Lambda\mathrm{D}}$. When an electric field is applied the states pick up energy E_{Stark}, and when a magnetic field is applied the states pick up energy E_{Zeeman}. In the presence of external fields the states are drawn as solid lines. For the precision EDM experiment we will perform spectroscopy on the transitions between the two pairs of $m_F = \pm 3/2$ states in the upper and lower doublet.

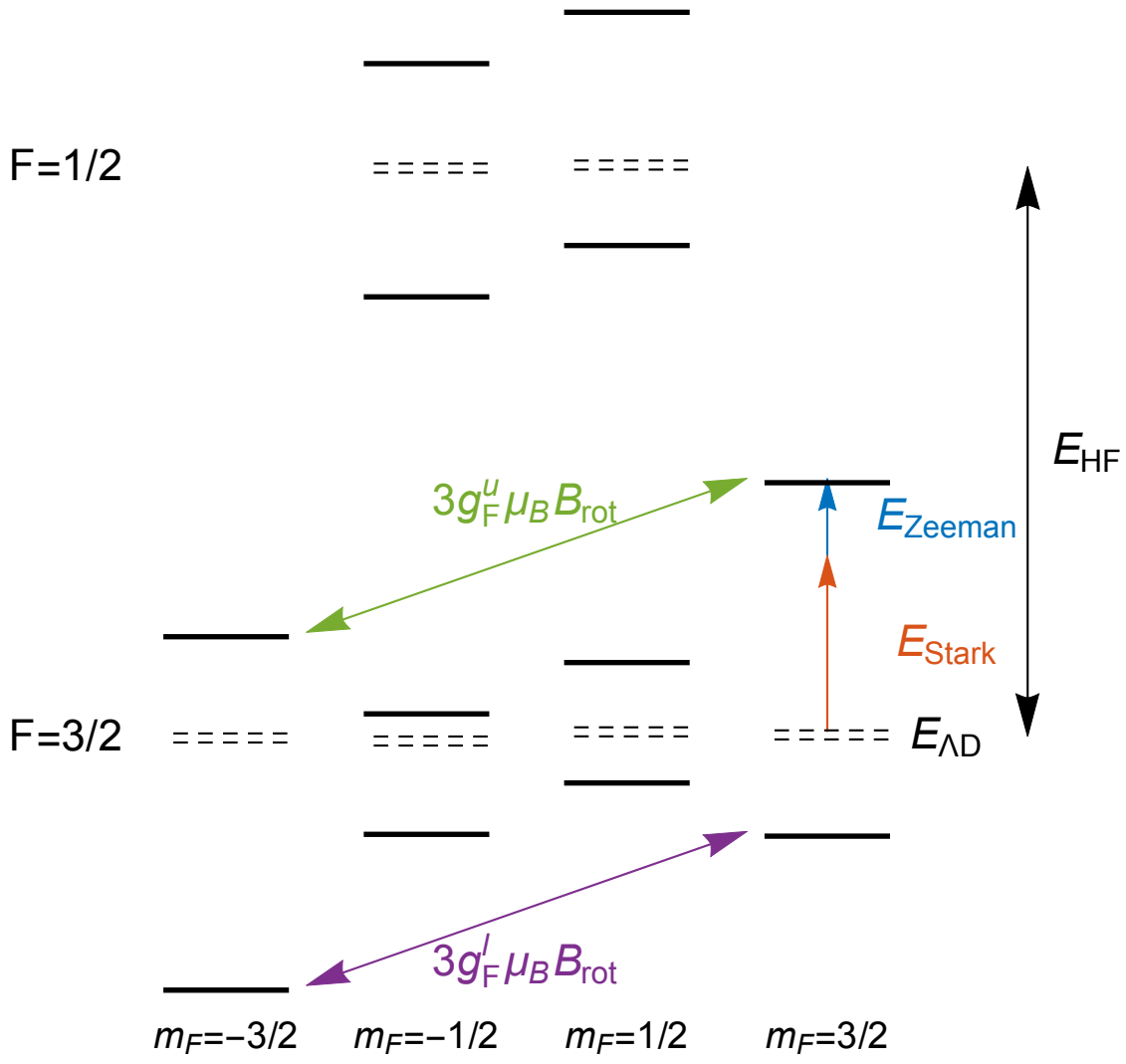

where $\alpha \approx 1/137$ is the fine structure constant, we would expect a cancellation to order α. We estimate the g-factor of the $F = 3/2$ state to be as small as $g_F \approx 0.00077$. Measurements of this value show that it is $g_F = 0.00305(10)$. This discrepancy can be due to $^3\Delta_1$ actually being an electronic state of predominantly $^3\Delta_1$ character but with slight admixtures of other electronic states, where this near cancellation of $(g_L\Lambda + g_S\Sigma)$ no longer holds. Moreover, while the g-factor for the upper and lower Λ doublet states are nominally the same, effects such as differential mixing with the $J = 2$ levels can create fractional differences on the 10^{-3} level.

Finally we must consider the effect of the electron EDM. The $^3\Delta_1$ state has an $\mathcal{E}_{\text{eff}} = 23.3$ GV/cm electric field that points along the internuclear axis. Choosing the externally applied electric field $\mathcal{E}_{\text{lab}}$ as the direction of our quantization axis $\hat{n}$ we find that for the upper doublet $\vec{\mathcal{E}}_{\text{eff}} \cdot \hat{n} = +23.3$ GV/cm, and for the lower doublet $\vec{\mathcal{E}}_{\text{eff}} \cdot \hat{n} = -23.3$ GV/cm. The EDM shift is $-d_e\vec{\mathcal{E}}_{\text{eff}} \cdot \vec{S}$, which is

$$H_{\text{EDM}}^{u/l} = \pm\Sigma d_e \mathcal{E}_{\text{eff}}, \tag{3.6}$$

where we note that for $m_F = \pm 3/2$ the projection of the electron spin on the internuclear axis is $\Sigma = \mp 1/2$.

We will proceed by separately considering the two pairs of states in the $F = 3/2$ manifold, the $|m_F = \pm 3/2, \Omega = \mp 1\rangle$ upper doublet states, and the $|m_F = \pm 3/2, \Omega = \pm 1\rangle$ lower doublet states. The Hamiltonians describing these two subspaces (with superscripts u and l denoting doublet) are

$$H^{u/l} = \frac{1}{2}\begin{pmatrix} 3(g_F \pm \delta g)\mu_B B \pm d_e\mathcal{E}_{\text{eff}} & 0 \\ 0 & -3(g_F \pm \delta g)\mu_B B \mp d_e\mathcal{E}_{\text{eff}} \end{pmatrix}, \tag{3.7}$$

where $\delta g_F = (g_F^u - g_F^l)/2$ describes the difference between g_F in the upper and lower doublets. In this reduced space Hamiltonian the sign of the electric field in the EDM term, $\mathcal{E}_{\text{eff}}$, depends on whether we are in the upper or lower Λ-doublet. This is because between the two doublets, the molecular axis, and hence the 23.3 GV/cm electric field, points in opposite directions with respect to Σ, the electron spin.

3.1.3 Effect of the rotating frame

The application of the bias electric field $\mathcal{E}_{\text{lab}}$ is not trivial in an ion trap, where the trapped region must by definition have $\left\langle \vec{\mathcal{E}} \right\rangle_t = 0$, otherwise the ions would be accelerated out of the trap. In order to work around this limitation of ion trapping technology we must apply a field $\mathcal{E}_{\text{lab}}$ where the time average $\left\langle \vec{\mathcal{E}_{\text{lab}}} \right\rangle_t = 0$. We apply a **rotating** electric field in the $x-y$ plane, $\vec{\mathcal{E}}_{lab} = \mathcal{E}_{\text{rot}}(\cos(\omega_{rot}t)\hat{x} + \sin(\omega_{rot}t)\hat{y})$[45]. There are primarily two effects of this:

(1) The ions are driven in uniform circular motion by the electric field. They make small circular orbits with radius $r = \frac{e\mathcal{E}_{\text{rot}}}{m\omega_{rot}^2}$, where $r \approx 0.47$ mm for typical operating conditions. In the presence of a quadrupole gradient $\boldsymbol{\nabla}\mathcal{B}$ these circular orbits have the effect in the molecule frame of a static magnetic field that is aligned with the quantization axis, $\mathcal{B}_{\text{rot}} = \boldsymbol{\nabla}\mathcal{B} r_{\text{rot}}$.

(2) The ions are accelerated into a rotating frame relative to the lab. In the lab frame this induces a coupling between neighboring m_F states. In the $|m_F = \pm 3/2\rangle$ reduced state space Hamiltonian the coupling is third order, and can be written as follows,

$$H^{u/l} = \frac{1}{2}\begin{pmatrix} 3(g_F \pm \delta g)\mu_B \mathcal{B}_{\text{rot}} - 3\alpha\omega_{rot} \pm d_e\mathcal{E}_{\text{eff}} & \Delta \pm \delta\Delta \\ \Delta \pm \delta\Delta & -3(g_F \pm \delta g)\mu_B Brot + 3\alpha\omega_{rot} \mp d_e\mathcal{E}_{\text{eff}} \end{pmatrix}, \tag{3.8}$$

where the off-diagonal coupling terms are [42, 44]

$$\Delta = 27\omega_{ef}\left(\frac{\hbar\omega_{rot}}{d_{\text{mf}}\mathcal{E}_{\text{rot}}}\right)^3\left(1 - \frac{1}{32}\left(\frac{d_{\text{mf}}\mathcal{E}_{\text{rot}}}{E_{\text{HF}}}\right)^2 - \frac{9}{512}\left(\frac{d_{\text{mf}}\mathcal{E}_{\text{rot}}}{E_{\text{HF}}}\right)^4\right) + \ldots, \tag{3.9}$$

$$\delta\Delta = \frac{3}{8}\Delta\left(\frac{d_{\text{mf}}\mathcal{E}_{\text{rot}}}{E_{HF}}\right)\left(1 + \frac{3}{32}\left(\frac{d_{\text{mf}}\mathcal{E}_{\text{rot}}}{E_{HF}}\right)^2 + \frac{57}{1024}\left(\frac{d_{\text{mf}}\mathcal{E}_{\text{rot}}}{E_{HF}}\right)^4\right) + \ldots. \tag{3.10}$$

3.2 Measurement

3.2.1 Ramsey spectroscopy

To measure the energy shift provided by $d_e E_{eff}$ we use Ramsey spectroscopy[56]. The general principle of Ramsey spectroscopy is to measure the energy difference, ΔE, of a two level quantum

system. The system can be described by the Hamiltonian,

$$H = \frac{1}{2}\begin{pmatrix} \Delta E & 0 \\ 0 & -\Delta E \end{pmatrix}. \tag{3.11}$$

We identify the two eigenstates of the system as $|\uparrow\rangle$ and $|\downarrow\rangle$, motivated by a spin-$\frac{1}{2}$ system. First

Figure 3.2: Depicted is a representation of Ramsey spectroscopy on the Bloch sphere. In (a) the system is initially prepared in $|\uparrow\rangle$ before a $\pi/2$ pulse rotates the system about the $|x\rangle$ axis, such that the system is in $|y\rangle = (|\uparrow\rangle + i\,|\downarrow\rangle)/\sqrt{2}$. In (b) the system precesses about the equator as $|\uparrow\rangle$ acquires phase $e^{t(\Delta E/2)/i\hbar}$ and $|\downarrow\rangle$ acquires phase $e^{-t(\Delta E/2)/i\hbar}$. Finally in (c) the second $\pi/2$ pulse is applied,

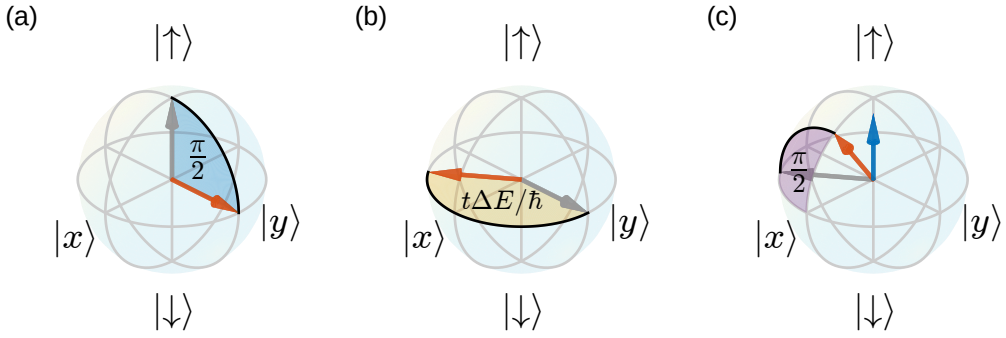

we prepare the system in one of two eigenstates, say $|\psi\rangle = |\uparrow\rangle$. As shown in fig. 3.2, we then apply a $\pi/2$ pulse operation, so called because the state is rotated by $\pi/2$ on the Bloch sphere to the equator. The state is now in the superposition $|\psi\rangle = \frac{1}{\sqrt{2}}(|\uparrow\rangle - i\,|\downarrow\rangle)$. If we allow the state to evolve forward in time under the Hamiltonian H, the phase of each component of the superposition will advance at a different rate,

$$|\psi(t)\rangle = \frac{1}{\sqrt{2}}\left(|\uparrow\rangle\, e^{\frac{t}{i\hbar}\Delta E/2} - i\,|\downarrow\rangle\, e^{-\frac{t}{i\hbar}\Delta E/2}\right). \tag{3.12}$$

We then apply a second $\pi/2$ identical to the first and measure the probability that the state is in $|\uparrow\rangle$ or $|\downarrow\rangle$,

$$P(\uparrow) = |\langle\uparrow|\psi\rangle|^2 = \sin^2\left(\frac{\Delta E}{2\hbar}t\right), \tag{3.13}$$

$$P(\downarrow) = |\langle\downarrow|\psi\rangle|^2 = \cos^2\left(\frac{\Delta E}{2\hbar}t\right). \tag{3.14}$$

We construct the population asymmetry by taking the probability difference over the probability sum,

$$\mathcal{A}(t) = \frac{P(\uparrow) - P(\downarrow)}{P(\uparrow) + P(\downarrow)} = -\cos\left(\frac{\Delta E}{\hbar}t\right). \tag{3.15}$$

By carefully measuring the frequency of oscillation of the asymmetry we can determine the energy difference of the two states ΔE.

3.2.1.1 Time Dependence

If the Hamiltonian in eq. (3.11) has some time dependence we require a more careful treatment,

$$H(t) = \frac{1}{2}\begin{pmatrix} \Delta E + \alpha(t) & 0 \\ 0 & -\Delta E - \alpha(t) \end{pmatrix}. \tag{3.16}$$

The propagator that we use to express how the phase between $|\uparrow\rangle$ and $|\downarrow\rangle$ must be explicitly integrated with respect to time,

$$|\psi(t)\rangle = \frac{1}{\sqrt{2}}\left(|\uparrow\rangle\, e^{\frac{1}{2i\hbar}\int_0^t \Delta E + \alpha(t')dt'} - i\,|\downarrow\rangle\, e^{-\frac{1}{2i\hbar}\int_0^t \Delta E + \alpha(t')dt'}\right). \tag{3.17}$$

With the addition of this time dependent term the asymmetry gain new time dependence,

$$\mathcal{A}(t) = -\cos\left(\frac{1}{\hbar}\left(t\Delta E + \int_0^t \alpha(t')dt'\right)\right). \tag{3.18}$$

If we assume that $\alpha(t)$ has some sinusoidal dependence, e.g. it is due to some oscillatory motion in the ion trap, we can write $\alpha(t) = \alpha_0 \cos(\omega t)$. We can now integrate $\alpha(t)$ in the asymmetry,

$$\mathcal{A}(t) = -\cos\left(\frac{1}{\hbar}(t\Delta E + \alpha_0 \sin(\omega t)/\omega)\right), \tag{3.19}$$

$$= -\cos\left(\frac{\Delta E}{\hbar}t\right)\cos\left(\frac{\alpha_0}{\hbar\omega}\sin(\omega t)\right)) + \sin\left(\frac{\Delta E}{\hbar}t\right)\sin\left(\frac{\alpha_0}{\hbar\omega}\sin(\omega t)\right)). \tag{3.20}$$

We may use 9.1.42 and 9.1.43 of Abramowitz and Stegun[3] to expand this as a series of Bessel functions,

$$\mathcal{A}(t) = -\cos\left(\frac{\Delta E}{\hbar}t\right)\left(J_0\left(\frac{\alpha_0}{\hbar\omega}\right) + \sum_{k=1}^{\infty} 2J_{2k}\left(\frac{\alpha_0}{\hbar\omega}\right)\cos(2k\omega t)\right)$$
$$+ \sin\left(\frac{\Delta E}{\hbar}t\right)\sum_{k=0}^{\infty} 2J_{2k+1}\left(\frac{\alpha_0}{\hbar\omega}\right)\sin((2k+1)\omega t), \tag{3.21}$$
$$\approx -\cos\left(\frac{\Delta E}{\hbar}t\right)J_0\left(\frac{\alpha_0}{\hbar\omega}\right) \qquad (\alpha_0 \ll \hbar\omega). \tag{3.22}$$

This time dependence has the effect of placing sidebands on the asymmetry. As long as the modulation index $\alpha_0/\hbar\omega \ll 1$ then the carrier frequency $\Delta E/\hbar$ should dominate and the spectral line will not shift.

3.2.2 Experimental Ramsey sequence

Using the coherent transfer process described in section 2.1.4 we prepare the HfF^+ ions in either the upper or lower doublet of the $^3\Delta_1, v = 0, J = 1, F = 3/2$ state, and an incoherent equal mixture of the $m_F = +3/2$ and $m_F = -3/2$ states. To achieve a pure initial state, e.g. $|\uparrow\rangle = |m_F = 3/2\rangle$, we must deplete the population in the undesired fraction of the incoherent mixture. We apply a series of laser pulses resonant with the $^3\Delta_1, J = 1, F = 3/2 \rightarrow^3 \Pi_0, J = 1, F = 3/2$ transition for state purification. We use the same laser that was used earlier in the experimental sequence to transfer the ions into the $F = 3/2$ state. The coherent state transfer laser is locked to a cavity to keep its wavelength stable throughout the transfer process. During the transfer procedure the laser was detuned from the $^3\Delta_1 \rightarrow^3 \Pi_0$ transition by one cavity FSR to prevent the intermediate state from becoming populated. For depletion the laser must be made resonant with the transition. We use a microcontroller to ramp the laser frequency one FSR of the cavity such that it is resonant with the depletion transition. We use a microcontroller because it allows us to ramp the laser frequency faster than the bandwidth of the electronics used to lock it to the cavity, such that when the ramp is finished a new lock is acquired now 1 FSR away.

The laser pulses are strobed at a frequency synchronous with the rotating electric field such

that the laser is only on when the k-vector is nearly parallel or antiparallel to the direction of the electric field. The laser light is circularly polarized, and by choosing the phase of the strobe such that k-vector of the laser beam points along or against the electric field direction, we can apply either σ^+ or σ^- circular polarization in the frame of our chosen quantization axis. Because we address a $\Delta J = 0$ transition, for the case of of $\sigma^+(\sigma^-)$ polarized light, only ions in the $m_F = -3/2$ ($m_F = +3/2$) have an allowed transition to the $^3\Pi_0$ state. Once promoted, the ions quickly spontaneously decay to various long lived states, with only a fraction returning to the $^3\Delta_1, J = 1$, leaving us with a pure state of ions in a single $m_F = 3/2$ or $m_F = -3/2$ in the $^3\Delta_1, J = 1$ rotational manifold. For clarity we will now only consider without loss of generality the state preparation that yields ions in upper doublet and the $m_F = +3/2$ state. We will use the shorthand $|\uparrow\rangle = |m_F = +3/2\rangle, |\downarrow\rangle = |m_F = -3/2\rangle$, $\Delta^u = \Delta + \delta\Delta$, and $g^u = g_F + \delta g$.

3.2.3 Applying $\pi/2$ pulses

To apply the $\pi/2$ pulse we take advantage of the rotation induced coupling between $|m_F = +3/2\rangle$ and $|m_F = -3/2\rangle$ in eq. (3.9),

$$H^u = \frac{1}{2}\begin{pmatrix} 3g^u\mu_B B + d_e\mathcal{E}_{\text{eff}} & \Delta^u \\ \Delta^u & -3g^u\mu_B B - d_e\mathcal{E}_{\text{eff}} \end{pmatrix}, \tag{3.23}$$

By quickly decreasing the magnitude of the rotating electric bias field $\mathcal{E}_{\text{rot}}$, we access a regime where $\Delta^u \gg (3g^u\mu_B B + d_e\mathcal{E}_{\text{eff}})$. In this regime the eigenstates are no longer pure $|\uparrow\rangle$ and $|\downarrow\rangle$, but the symmetric and antisymmetric superpositions

$$|\psi_S\rangle = \frac{1}{\sqrt{2}}(|\uparrow\rangle + |\downarrow\rangle), \tag{3.24}$$

$$|\psi_A\rangle = \frac{1}{\sqrt{2}}(|\uparrow\rangle - |\downarrow\rangle). \tag{3.25}$$

The state $|\uparrow\rangle = \frac{1}{\sqrt{2}}(|\psi_S\rangle + |\psi_A\rangle)$ will rotate into $\frac{1}{\sqrt{2}}(|\uparrow\rangle - i\,|\downarrow\rangle)$ in time $t_{\pi/2} = \frac{\pi}{2}\frac{\hbar}{\Delta^u}$. After waiting $t_{\pi/2}$ we quickly ramp the rotating electric bias field back up to return to the regime where Δ^u is small. After applying the $\pi/2$ pulse, the ions sit undisturbed in the ion trap for a time T. The phase between $|\uparrow\rangle$ and $|\downarrow\rangle$ will precess at the frequency $3g^u\mu_B B + 2d_e\mathcal{E}_{\text{eff}}$. We then apply

a second $\pi/2$ pulse and a second series of depletion laser pulses synchronized with the rotating electric field. By performing successive experiments where the second depletion strobe is in phase with the rotating electric field and where the strobe is π out of phase with the rotating electric field we are able to alternatively measure the final population of ions in $\left|m_F = +\frac{3}{2}\right\rangle$ and in $\left|m_F = -\frac{3}{2}\right\rangle$. We perform several sets of measurements of the asymmetry at different times T to create a Ramsey fringe. We fit the frequency f of the fringe with a nonlinear least squares algorithm to extract $3g^u\mu_B B + 2d_e\mathcal{E}_{\text{eff}} = 2\pi\hbar f$.

3.2.4 Optimizing statistical sensitivity

The statistical uncertainty on our measurement of the Ramsey frequency f is directly proportional to the statistical uncertainty we can ascribe to the energy shift due to $d_e\mathcal{E}_{\text{eff}}$. In the previous section we considered an ideal Ramsey fringe with perfect initial state contrast, precise $\pi/2$ pulses, and infinite lifetime. Unfortunately, nature conspires against us, and none of these conditions are fully realized. A more realistic Ramsey fringe might look like this:

$$\mathcal{A}(t) = -\mathcal{C}(t/\tau)\cos(2\pi(ft+\phi)) + \mathcal{O}. \tag{3.26}$$

Here we have allowed for a contrast $\mathcal{C} < 1$ that can decay as some function of t in a characteristic time τ. Also included are an intial phase ϕ in units of fractional periods (i.e., radians $\times 2\pi$) and a dimensionless fringe offset $\mathcal{O}$, which can result from $\pi/2$ pulses that are not precisely $\frac{\pi}{2}\frac{\hbar}{\Delta}$ in duration, of if the approximation that $\Delta \gg 3g_F\mu_B B$ does not strongly hold. To maximize the statistical sensitivity of our experiment we should device a scheme where we can minimize σ_f, the statistical uncertainty of frequency. If we propagate uncertainty through this expression, we see that

$$\sigma_{\mathcal{A}}^2 = (2\pi t\mathcal{C}(t/\tau)\sin(2\pi(ft+\phi)))^2\left(\sigma_f^2 + \sigma_\phi^2/t^2\right) + (\cos(2\pi(ft+\phi)))^2\left(\mathcal{C}'(t/\tau)\frac{t}{\tau^2}\sigma_\tau^2 + \frac{\mathcal{C}(t/\tau)}{\mathcal{C}_0}\sigma_{\mathcal{C}_0}^2\right) + \sigma_{\mathcal{O}}^2. \tag{3.27}$$

This expression is fairly tedious, and what we are looking for is to minimize σ_f. There are a few reasonable strategies we can employ that will both simplify eq. (3.27) and minimize σ_f.:

- Take data at fringe zero crossings if we take data at the peaks of the Ramsey fringe, $2(ft+\phi) = n$, where n is an integer, then the coefficient of σ_f diverges, and we have no sensitivity to frequency. If instead we choose $2(ft+\phi) = n + \frac{1}{2}$, then we maximize our sensitivity to f, and the terms for the uncertainty in the contrast, σ_τ and $\sigma_{\mathcal{C}_0}$, drop out. This can be a bit tricky, because choosing the correct time t requires prior knowledge of the frequency, which is the quantity we are trying to measure. We must first make a rough measurement of frequency that is precise enough that we can choose t to ensure that n really is an integer. The uncertainty in n is $\sigma_n = n\sigma_f/f$, and we would like $\sigma_n \ll 1/2$. This requires that $\sigma_f/f \ll 1/2n$, so if we are trying to make a measurement 10 periods into a Ramsey fringe ($n = 20$), then we must first measure the frequency to much better than 1 part in 40. If we can successfully do this then eq. (3.27) simplifies to

$$\sigma_f^2 + \sigma_\phi^2/t^2 = \frac{\sigma_{\mathcal{A}}^2 - \sigma_{\mathcal{O}}^2}{\left(2\pi t\mathcal{C}(t/\tau)\sin(2\pi(ft+\phi))\right)^2}. \tag{3.28}$$

- Fix ϕ and $\mathcal{O}$.

  The parameters ϕ and $\mathcal{O}$ are mostly affected by the preparation of the Ramsey fringe, the initial state contrast, the purity of the $\pi/2$ pulse, etc. We can make a rough initial measurement of ϕ and $\mathcal{O}$ and hold these values fixed in our nonlinear fitting. This will have the effect of potentially shifting the value of f that we determine from out fitting routine, but because we are interested in differential shifts in f, these potential shifts drop out. Also, we note that at $t = 0$ we can make an independent measure of ϕ and $\mathcal{O}$ and their uncertainty where there is no dependence on the frequency of the Ramsey fringe. If we allow ϕ to float in our nonlinear fitting routine, then $\sigma_f^2 \approx \sigma_\phi^2/t^2$, which will have the effect of increasing the uncertainty in f by a factor of $\sqrt{2}$. With these simplications eq. (3.28) becomes

$$\sigma_f = \frac{\sigma_{\mathcal{A}}}{2\pi t\mathcal{C}(t/\tau)\sin(2\pi(ft+\phi))}. \tag{3.29}$$

- Minimize $\sigma_{\mathcal{A}}$

The uncertainty in frequency is proportional to the uncertainty in the measurement of the asymmetry. For a measurement that is Poisson distributed, $\sigma_{\mathcal{A}} \sim 1/\sqrt{N}$, where N is the number of ion counts. Generally, to minimize $\sigma_{\mathcal{A}}$ we will want to operate with the highest possible number of experimental counts. Nicholas Hutzler points out in his thesis [38] that the asymmetry is not actually a Poisson distributed random variable, and we will consider that below. The asymmetry $\mathcal{A}$ is a dimensionless quantity that is the ratio of two Poisson statistics and is not itself Poisson distributed, which is why $\sigma_{\mathcal{A}}$ is not the typically expected $\sqrt{N}$.

The asymmetry is the ratio of the difference and the sum of two Poisson distributed variables, $N_\uparrow$ and $N_\downarrow$. Assuming no other sources of noise, the uncertainty in these will be the Poisson distribution uncertainty, $\sigma^2_{N_\uparrow} = N_\uparrow + bg$, where bg is the background counts. If we propagate uncertainties through the asymmetry, we find

$$\sigma^2_{\mathcal{A}} = \frac{4}{(N_\uparrow + N_\downarrow)^4}\big(N^2_\uparrow \sigma^2_\downarrow + N^2_\downarrow \sigma^2_\uparrow\big), \tag{3.30}$$

$$= \frac{4}{(N_\uparrow + N_\downarrow)^4}\big(N^2_\uparrow (N_\downarrow + bg) + N^2_\downarrow (N_\uparrow + bg)\big), \tag{3.31}$$

$$= \frac{4N_\uparrow N_\downarrow}{(N_\uparrow + N_\downarrow)^3} + \frac{4(N^2_\uparrow + N^2_\downarrow)bg}{(N_\uparrow + N_\downarrow)^4}, \tag{3.32}$$

$$= \frac{1 - \mathcal{A}^2}{(N_\uparrow + N_\downarrow)} + \frac{2(1 + \mathcal{A}^2)bg}{(N_\uparrow + N_\downarrow)^2}, \tag{3.33}$$

$$\sigma_{\mathcal{A}} = \sqrt{\frac{1}{N}}\sqrt{1 - \mathcal{A}^2 + 2(1 + \mathcal{A}^2)bg/N}, \tag{3.34}$$

where $N = N_\uparrow + N_\downarrow$ is the total number of potential signal ion counts. When we are measuring at the zero crossing of a fringe where $\mathcal{A} = 0$ the asymmetry uncertainty $\sigma_{\mathcal{A}} \sim 1/\sqrt{N}$, and that this is increased in the presence of background noise by a factor of $\sqrt{1 + 2bg/N}$.

- Maximize t

The frequency uncertainty $\sigma_f \sim 1/t$, so we achieve the best precision when we can measure our fringes out at long times. This is the primary motivation for performing the experiment in an ion trap, where long coherence times are possible.

- Choose $t < \tau$

  The experimental reality in the ion trap is that decohering processes do exist, and cause $\mathcal{C}(t)$ to trend towards 0 as $t \to \infty$. It's unclear what the exact functional form of $\mathcal{C}$ should be, as this depends on the exact mechanisms causing the decoherence, but we can experimentally determine a characteristic time in which the coherence decays, which is referred to as τ. This aim is directly at odds with the previous point, where taking data at long fringe times yields the minimal frequency uncertainty. We can determine the optimal time to focus our data collection efforts by finding the time that minimizes σ_f,

$$\sigma_f = \frac{\sqrt{1 + 2bg/N(t)}}{2\pi t \mathcal{C}(t/\tau)\sqrt{N(t)}}. \tag{3.35}$$

  Additionally, a time dependence has been included in the total number of experimentally accessible ions, $N(t)$. We perform Ramsey spectroscopy in the $^3\Delta_1$ electronic state of HfF^+, which we have experimentally determined to have a $\tau_3 = 2.1(1)$ seconds [50]. Including this exponential decay in signal further complicates the expression,

$$\sigma_f = \frac{\sqrt{1 + 2bg/(N_0 e^{-t/\tau_3})}}{2\pi t \mathcal{C}(t/\tau)\sqrt{N_0 e^{-t/\tau_3}}}. \tag{3.36}$$

  Indeed, it does seem difficult to find a fully optimal time to collect data without knowing the exact functional form with which the coherence decays. A good starting point is to simply assume any functional form that monotonically decreases to 0 as $t \to \infty$. One such function is the exponential function, and if we optimize σ_f, assuming $bg \ll N$, then we find the frequency uncertainty is minimized at

$$t = \frac{2\tau_3\tau}{2\tau_3 + \tau} = \frac{2\tau}{2 + \tau/\tau_3} = \frac{2\tau_3}{1 + 2\tau_3/\tau}, \tag{3.37}$$

  which suggest that if the coherence time τ is much less than the $^3\Delta_1$ lifetime of 2 seconds, then we should take data when $t = \tau$. On the other hand, if decoherence is not the main

limitation, and $\tau \gg \tau_3$, then we can achieve the most frequency sensitivity by choosing $t = 2\tau_3 \approx 4.2$ seconds.

3.2.4.1 Coherence Time

The factors limiting our coherence time are explored in detail by Kevin Cossel in his PhD thesis[17], but we will review them here. There are two dominant decoherence mechanisms that we have observed, decoherence due to long range ion-ion collision via the Coulomb interaction and decoherence due to spatial inhomogeneity of magnetic fields.

- Ion-ion collisions can occur when ions in the trap get close enough such the electric field of the colliding ion is larger than that from that rotating bias field $\mathcal{E}_{\text{rot}}$. This causes the polarization of the molecule to drift off the quantization axis, causing the phase between m_F states to become scrambled. Intuitively this will happen more often when the ions are at higher temperatures, as the ions will have sufficient kinetic energy to overcome the Coulomb barrier and come close enough to collide. Additionally it should occur less often for larger $\mathcal{E}_{\text{rot}}$, as more kinetic energy will be required to tilt the quantization axis. The decoherence rate due to this high energy, hard sphere type of collision is

$$\Gamma_{\text{hot}} \sim n\frac{\sqrt{T}}{\mathcal{E}_{\text{rot}}}, \tag{3.38}$$

where n is the ion density. Additionally there is another collision mechanism in the low energy limit. Glancing collisions of ions can tip the molecular axis off of the quantization axis slightly. Over the course of a transit of a colliding ion, the molecule axis will tilt away and return, tracing out a geometric phase. Over the course of many collisions the phase will randomly walk off, leading to decoherence. Intuitively this will also be suppressed at lower temperatures and higher $\mathcal{E}_{\text{rot}}$, but with very different power scaling,

$$\Gamma_{\text{cold}} \sim n\frac{\sqrt{T}}{\mathcal{E}_{\text{rot}}}\frac{T^6}{\mathcal{E}_{\text{rot}}^3}. \tag{3.39}$$

Empirically we observe a scaling of decoherence with $\mathcal{E}_{\text{rot}}^{-2.3}$ in fig. 3.3, which implies that the temperature is such that we are at an intermediate situation between these two effects.

Figure 3.3: Measurements of coherence time when changing ion density n and $\mathcal{E}_{\rm rot}$. The coherence time in (a) varies linearly with ion density, as in eqs. (3.38) and (3.39) until it reaches a ceiling due to the decoherence due to field inhomogeneities. The coherence time in (b) scales roughly as $\mathcal{E}_{\rm rot}^2$.3, possibly indicating the combination of the effects in eqs. (3.38) and (3.39).

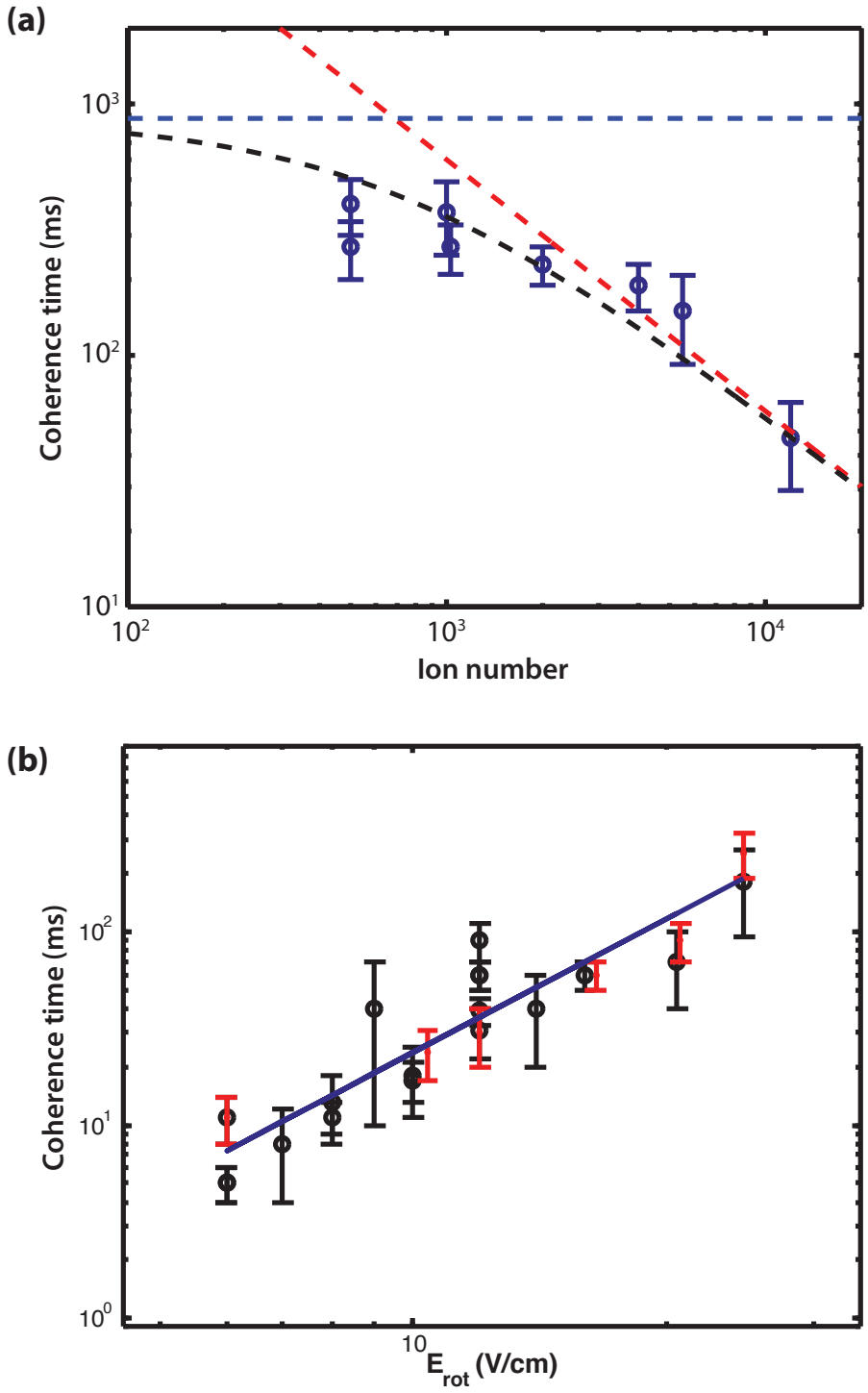

- An inhomogeneous magnetic field $\mathcal{B}_{\text{rot}}$ will result in some ions experiencing one fringe frequency and other ions experiencing a different fringe frequency. Like an ensemble of initially synchronized clocks ticking with spread of frequencies Δf, in some time $\tau \sim 1/(2\pi\Delta f)$ the phase between the ions in the ensemble will decohere. The Ramsey fringe frequency $f = 3g_F\mu_B\mathcal{B}_{\text{rot}}$, where $\mathcal{B}_{\text{rot}}$ is applied via the combination of the circular micromotion in the ion trap and a quadrupole gradient $\boldsymbol{\nabla}\mathcal{B}$, $\mathcal{B}_{\text{rot}} = \boldsymbol{\nabla}\mathcal{B}r_{\text{rot}}$. Any fractional inhomogeneity in $\mathcal{B}_{\text{rot}}$ due to e.g. trapping field inhomogeneities can be expressed as $\Delta f/f$ and included in $\tau \sim 1/(2\pi(\Delta f/f)f)$, and we see that

$$\Gamma_{\text{inhomogeneity}} \sim \frac{1}{f}. \tag{3.40}$$

  In general this type of mechanism should cause the coherence to decay as e^{-t^2/τ^2} [59], but we have been unable to differentiate this effect by fitting coherence decays to $e^{-t/\tau}$ c.f. e^{-t^2/τ^2}: both functional forms appear reasonable descriptions. Measurements of coherence time for difference fringe frequencies show that there is a fractional inhomogeneity of $\Delta f/f \sim 0.5\%$ over the size of the ion cloud.

3.2.4.2 Data rate and duty cycle

So far we have only discussed the frequency uncertainty of a single run , or "shot" of the experiment. To achieve a sufficiently high number of counts, N, it is important to run many experimental shots in series, potentially hundreds of hours of data comprising millions of ion counts. As such, it is important to not only consider the single shot frequency sensitivity but also the frequency sensitivity as a function of experimenter's time.

We will use eq. (3.36) and assume without loss of generality the limiting case of no background counts. If we perform several shots of the experiment in series, we will acquire both background counts and signal counts, but the ratio bg/N will remain unchanged, and the numerator in eq. (3.36) can be normalized to 1 and safely included later. Considering the case of running the experiment for a sufficiently long integration time, T_{int}, then the total number of ion counts we expect to see is

$N = \dot{N}T_{int}$, where $\dot{N}$ is the count rate of the experiment and $\dot{N} = N_{\text{shot}}/T_{\text{shot}}$. The quantity N_{shot} is the number of ion counts in a single shot of the experiment, or $N_0 e^{-t/\tau_3}$, and T_{shot} is the amount of time between the start of one experimental shot and the next. The time of an experiment shot should contain t, the amount of time we spend performing the Ramsey spectroscopy, but should also include some measure of dead time. This experiment dead time has several sources, but they are primarily the time spent in initial state preparation ($\approx$ 150 ms), and the time spent in state readout ($\approx$ 250 ms). Additionally, because the ionization lasers used to create HfF^+operate at 10 Hz, the experiment is triggered off this 10 Hz signal. This means there is the potential to be waiting up to 100 ms between experimental sequences if the time it takes to perform an experiment slightly exceeds an integer multiple of 100 ms. On average this contributes to a dead time of $\approx$ 50 ms. Adding in the contribution of running the experiment for many runs into eq. (3.36) we find

$$\sigma_f = \frac{\sqrt{t + t_{dead}}}{2\pi t \mathcal{C}(-t/\tau)\sqrt{N_0 e^{-t/\tau_3}}\sqrt{T_{int}}}. \tag{3.41}$$

The first point to note is the inclusion of a new factor of $\sqrt{t}$ in the numerator of the expression. There are two limiting cases to consider. The first is when $t_{\text{dead}} \gg t$, when the experiment is relatively unoptimized and there is much dead time between Ramsey sequences. This case removes the extra $\sqrt{t}$ dependence from σ_f and is now the same as above in eq. (3.36), where the optimal $t = \tau$. The second limiting case is when $t_{dead} \ll t$, and in this case we find that the new optimal time to take data at is

$$t = \frac{\tau_3 \tau}{2\tau_3 + \tau}, \tag{3.42}$$

which is a full factor of 2 shorter than eq. (3.37). In practice the experiment operates under this regime, where $\tau_3 = 2.1(1)$s, $\tau \approx 1$s, and $t_{dead} \approx 0.45$s, and the optimal $t \approx 0.58$s, assuming exponential decay in coherence. It is worth pointing out that a precise value for t does not really matter, as σ_f is very flat - 10% variations in t about the maximum only contribute to a 0.3% variation in σ_f. Moreover, the minimum value of σ_f does not have a strong dependence on the functional form of the decoherence - trying a variety of monotonically decreasing functions yield about the same minimum, as seen in fig. 3.4. If we insert some realistic experimental parameters to estimate

Figure 3.4: In this figure we have plotted examples of the frequency uncertaintyeq. (3.36) for a range of parameters. The default parameters are dead time $t_{\text{dead}} = 0.45$ s, coherence time $\tau = 1.0$ s, $^3\Delta_1$ radiative lifetime $\tau_3 = 2.1$ s, initial contrast $C_0 = 1$, and $N_0 = 1$ intial counts per shot. The defeault functional form used to describe the decay of coherence it $C(t) = exp(-t/\tau)$.

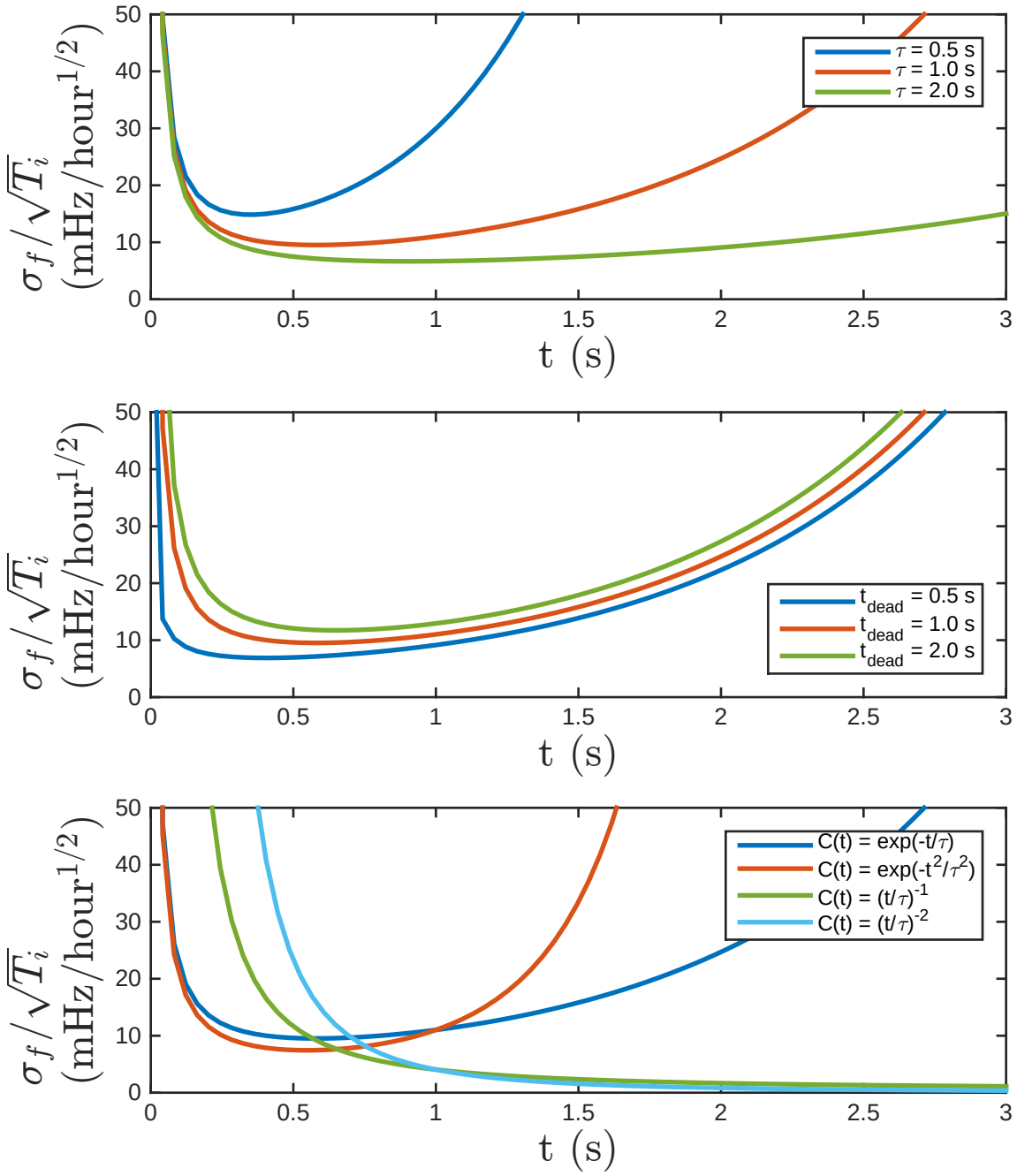

the frequency uncertainty, we find that for $N = 30$ counts per shot, with 3 background counts, an initial contrast $\mathcal{C}(0) = 0.3$, and a coherence time of $\tau = 1$ second, that $\sigma_f \approx 6.3$ mHz/$\sqrt{\text{hour}}$. With the effective electric field $\mathcal{E}_{\text{eff}} = 23.3 \times 10^9$ V/cm this is about 5.6×10^{-28} $e\cdot$cm/$\sqrt{\text{hour}}$. A typical run of experiments with these parameters achieves a sensitivity of ~ 22mHz/$\sqrt{\text{hour}}$. This is a factor of 3.5 worse than our expectation. The primary reason is that we spent a portion of our duty cycle acquiring Ramsey fringe data at short times to measure the initial phase ϕ. This both impacts out duty cycle and also the statistical sensitivity by introducing competing uncertainty quadratures σ_ϕ and $\sigma_{\mathcal{O}}$. Together these effects decrease our frequency sensitivty by a factor of 2. The additional discrepancy is due to the counts on our ion detector are a factor of 1.5 above the shot noise limit.

Chapter 4

Systematic uncertainty

4.1 Overview

What we have primarily discussed up to this point is the statistical sensitivity of the experiment. All of this sensitivity is pointless unless we can isolate the effect of the EDM. As we discussed in the previous chapter, when we apply rotating electric and magnetic fields to the HfF^+ molecule it is polarized along the electric field direction, and in the rotating frame we can consider the following effective two state Hamiltonian

$$H^{u/l} = \frac{1}{2}\begin{pmatrix} 3(g_F \pm \delta g)\mu_B(\mathcal{B}_{\rm rot} + \delta\mathcal{B}) + 3\alpha\omega_{rot} \pm d_e\mathcal{E}_{\rm eff} & \Delta \pm \delta\Delta \\ \Delta \pm \delta\Delta & -3(g_F \pm \delta g)\mu_B(\mathcal{B}_{\rm rot} + \delta\mathcal{B}) - 3\alpha\omega_{rot} \mp d_e\mathcal{E}_{\rm eff} \end{pmatrix}, \tag{4.1}$$

which describes the $|m_F = \pm 3/2\rangle$ states in the upper and lower doublets. The terms δg and $\delta\Delta$ are included to describe the differences in g-factor and rotation induced coupling between the two doublets, $\delta\mathcal{B}$ describes a residual magnetic field, and $3\alpha\omega_{rot}$ describes the perturbation due to the electric field making a small angle α with the plane of rotation. In the limit that $3g_F\mu_B\mathcal{B}_{\rm rot} \gg \Delta$ then we observe a Ramsey fringe frequency on the ${}^3\Delta_1, J = 1, F = 3/2, m_F = \pm 3/2$ transition that is approximately equal to

$$f = 3g_F\mu_B(\mathcal{B}_{\rm rot} + \delta\mathcal{B}) + d_e\mathcal{E}_{\rm eff}. \tag{4.2}$$

We will develop the various other terms that affect this frequency and gradually add more realism. In principle we could operate with $\mathcal{B}_{\rm rot} = 0$, so that the entire measured effect is due to $d_e\mathcal{E}_{\rm eff}$. There are several problems with this. The first is that the frequency shift due to even a very

small magnetic field $\mathcal{B}$ will overwhelm $d_e\mathcal{E}_{\text{eff}}$. An EDM that is $10^{-28}e$ cm contributes a frequency shift of 1.1 mHz, which will be overwhelmed by a rotating magnetic field as small as 100 nGauss. The second is that unless $3g_F\mu_B\mathcal{B}_{\text{rot}} \gg \Delta$, then the $|m_F = \pm 3/2\rangle$ states are highly mixed and a Ramsey experiment is impossible. To try to cancel out the effect due to $\mathcal{B}_{\text{rot}}$, we can make two measurements, one at $\mathcal{B}_{\text{rot}} + \delta\mathcal{B}$, and one at $-\mathcal{B}_{\text{rot}} + \delta\mathcal{B}$, where the sign change in $\mathcal{B}_{\text{rot}}$ corresponds to having $\mathcal{B}_{\text{rot}}$ point in the opposite direction with respect to the electric field. We only measure the absolute value of frequency, so switching the sign of $\mathcal{B}_{\text{rot}}$ has the effect of changing the relative sign of $\delta\mathcal{B}$ in the absolute value frequency measurement. We can consider the sum and the difference of these two measurements,

$$f^0 = \frac{1}{2}(f(+B) + f(-B)) = 3g_F\mu_B\mathcal{B}_{\text{rot}}, \tag{4.3}$$

$$f^B = \frac{1}{2}(f(+B) - f(-B)) = 3g_F\mu_B\delta\mathcal{B} + 2d_e\mathcal{E}_{\text{eff}}. \tag{4.4}$$

Here we introduce the notation of the frequency components f^0 and f^B, which are the linearly independent contributions to the frequency that are even and odd under the reversal of the rotating magnetic field. We can see that by calculating these two different linear combinations of the two data with a switched magnetic field, we divide the signal into two channels, one that is the Zeeman contribution to the Ramsey frequency, and one that is the electron EDM and the Zeeman effect, but now suppressed by a factor of $\delta\mathcal{B}/\mathcal{B}_{\text{rot}}$. It is important to note that these are sums and differences of frequency measurements, and the propagation of uncertainty works out such that the uncertainty of f^0 and f^B is no more than if we had taken measurements of only $f(+B)$ or $f(-B)$ during the same duration of time. Partitioning the data in this fashion yields clearer information. We have cleanly divided our data into a portion that is purely due to $\mathcal{B}_{\text{rot}}$ and a portion that is due to the EDM and some residual part of $\mathcal{B}_{\text{rot}}$. By performing the same sort of switch between positive and negative values of other parameters in the experiment we can continue to peel off other important quantities that are useful for analysis and diagnostics, e.g. Δ, leaving a core that is the electron EDM contribution and suppressed systematic effects. Generally, the more switches are added, the more suppression we can achieve on some of these systematics. Additionally, by measuring the

diagnostics in the other channels, the residual systematic contributions in the EDM channel can be corrected for, see section 5.1.4. For the single switch of $\mathcal{B}_{\rm rot}$ that we have considered, the remaining systematic in the EDM channel is $3g_F\mu_B\mathcal{B}_{\rm rot}(\delta\mathcal{B}/\mathcal{B}_{\rm rot})$. Ideally $(\delta\mathcal{B}/\mathcal{B}_{\rm rot})$ will be zero, but reality is not so kind. We will not be able to perfectly reverse the rotating magnetic field, and this will account for some $(\delta\mathcal{B}/\mathcal{B}_{\rm rot})$, perhaps $\sim 10^{-3}$. Additionally there will be ambient nonreversing magnetic fields present in the experiment due to the circular micromotion of the ions in the trap coupled to ambient magnetic field gradients in the lab due to ferromagnetic materials. Finally, rotating electric field is created by sinusoidal voltages on the trap electrodes. Any capacitance in the electrodes and cables leading to them can create currents running in the electrodes which will have the effect at the center of the trap of a magnetic field that rotates in synchrony with $\mathcal{B}_{\rm rot}$, but does not change sign when $\mathcal{B}_{\rm rot}$ is switched. These contributions are all summarized in $\delta\mathcal{B}$. In order to further suppress $(\delta\mathcal{B}/\mathcal{B}_{\rm rot})$ we can take advantage of the two Λ-doublets. Because they have very nearly the same g-factor they can be considered like a co-magnetometer that is internal to the molecule[20]. This comagnetometer can be used to measure the offending $\delta\mathcal{B}$ and compensate for it. We can exploit this opportunity by taking sequential measurements where the preparation is switched between transferring populating into the upper and into the lower Λ-doublets. We refer to this switch with superscript D, and the switch $\mathcal{B}_{\rm rot}$ with superscript B, and by taking four frequency measurements $f(\pm B,\pm D)$ we construct the four linearly independent combinations,

$$f^0 = \frac{1}{4}(f(+B,+D)+f(-B,+D)+f(+B,-D)+f(-B,-D)) \approx 3g_F\mu_B\mathcal{B}_{\rm rot}, \tag{4.5}$$

$$f^B = \frac{1}{4}(f(+B,+D)-f(-B,+D)+f(+B,-D)-f(-B,-D)) \approx 3g_F\mu_B\mathcal{B}_{\rm rot}\left(\frac{\delta\mathcal{B}}{\mathcal{B}_{\rm rot}}\right), \tag{4.6}$$

$$f^D = \frac{1}{4}(f(+B,+D)+f(-B,+D)-f(+B,-D)-f(-B,-D)) \approx 3g_F\mu_B\mathcal{B}_{\rm rot}\frac{\Delta\delta\Delta}{(3g_F\mu_B\mathcal{B}_{\rm rot})^2}, \tag{4.7}$$

$$\begin{aligned} f^{BD} &= \frac{1}{4}(f(+B,+D)-f(-B,+D)-f(+B,-D)+f(-B,-D)) \\ &\approx 3g_F\mu_B\mathcal{B}_{\rm rot}\left(\frac{\delta\mathcal{B}}{\mathcal{B}_{\rm rot}}\right)\left(\frac{\delta g}{g_F}-\frac{\Delta\delta\Delta}{(3g_F\mu_B\mathcal{B}_{\rm rot})^2}\right)+2d_E\mathcal{E}_{\rm eff} \approx f^B\left(\frac{\delta g}{g_F}-\frac{f^D}{f^0}\right)+2d_E\mathcal{E}_{\rm eff}. \end{aligned} \tag{4.8}$$

Combining the frequency measurements has two advantages. The first is that we may take an appropriate combination of the four terms f^0, f^B, f^D, f^{BD}, and in conjunction with a careful characterization of $\delta g/g$, extract $d_e\mathcal{E}_{\text{eff}}$ while removing all first order effects. The second advantage is that these frequency linear combinations are a good tool for discovering systematic errors. Broadly speaking, a systematic error is any effect that could be confused for the EDM, which could be any other term that appears in f^{BD}. For every additional switched parameter we see that systematic effects are suppressed, and in some other linear combination the same systematic effect appears in an unsuppressed way. Consider the linear combinations f^B and f^{BD}. The systematic effect of non-reversing magnetic fields appears as a systematic in f^{BD} as $3g_F\mu_B\mathcal{B}_{\text{rot}}\left(\frac{\delta\mathcal{B}}{\mathcal{B}_{\text{rot}}}\right)\left(\frac{\delta g}{g_F}-\frac{\Delta\delta\Delta}{(3g_F\mu_B\mathcal{B}_{\text{rot}})^2}\right)$, but a nearly identical term appears in f^B as $3g_F\mu_B\mathcal{B}_{\text{rot}}(\delta B/\mathcal{B}_{\text{rot}})$. Because $\frac{\delta g}{g_F}\approx 10^{-3}$ we can see the effect due to any unintentionally applied non-reversing magnetic fields much more easily in f^B than in f^{BD}. By deliberately tuning various parameters of the experiment to extreme operating conditions (e.g. large stray magnetic fields, detuned $\pi/2$ pulses, etc.) we can monitor f^B and the other linear combinations for effects that might appear in the f^{BD}, or "EDM channel", but in a less detectable way.

We introduce a general notation of keeping track of these various systematic terms, following the example of Sandars[34], Hinds[37], and ACME[13]. For a set of different possible switched parameters $S=\{B,D,\dots\}$ with length $n(S)$, there exist 2^n possible different states of the experiment, with 2^n possible frequency measurements, $f(\pm B,\pm D,\pm\dots)$. This yields 2^n possible different linear combinations of frequency measurements,

$$f^{\mathcal{R}}=\frac{1}{2^n(S)}\sum_{s\subseteq\mathcal{S}}(-1)^{n(\mathcal{R}\cup s)}f(-s,\mathcal{S}\setminus s), \tag{4.9}$$

where $\mathcal{R}$ is the set of switched parameters we are taking the antisymmetric difference over, and we sum over all 2^n possible subsets s of $\mathcal{S}$, and $f(-s,\mathcal{S}\setminus s)$ is a frequency measurement with the switched parameters in subset s in the negative configuration, and the switched parameters in subset complement $S\setminus s$ in the positive configuration. For example, in the above discussion we considered $S=\{B,D\}$, where magnetic field and doublet were switched parameters. The linear

combination corresponding to the non-reversing magnetic field channel

$$f^B = \frac{1}{4}(f(+B,+D) - f(-B,+D) + f(+B,-D) - f(-B,-D)), \tag{4.10}$$

where $f(+B,+D)$ means the Ramsey frequency measurement made with $\mathcal{B}_{\rm rot}$ pointing in the same direction as $\mathcal{E}_{\rm rot}$ and in the upper doublet.

In addition to switching the magnetic field direction (B), and the Λ-doublet (D), Another important parameter to switch is the direction of rotation of the rotating electric field (R). There are potential systematic effects due to Berry's phase that might arise because we are deliberately rotating our quantization axis. By performing a rotation switch we can characterize and suppress these systematic effects. The $d_e\mathcal{E}_{\rm eff}$ term does not change sign under rotation direction, and so the EDM appears in the f^{BD} channel and the f^{BDR} channel. Adding in this third switch to the set of switches we can write down eight linearly independent combinations of the frequency, and perform the series expansions of the small parameters $\delta\mathcal{B}, \delta g, \delta\Delta, \Delta$, and α,

$$f^0 = 3\mu_B g_F \mathcal{B}_{\rm rot} + \frac{\Delta^2}{2(3\mu_B g_F \mathcal{B}_{\rm rot})} + \frac{\delta\Delta^2}{2(3\mu_B g_F \mathcal{B}_{\rm rot}} + \ldots., \tag{4.11}$$

$$f^B = 3g_F\mu_B\delta\mathcal{B}\left(1 - \frac{\Delta^2+\delta\Delta^2}{2(3g_F\mu_B\mathcal{B}_{\rm rot})^2}\left(1 + 3\left(\frac{3\alpha\omega_{rot}}{3g_F\mu_B\mathcal{B}_{\rm rot}}\right)^2\right)\right) + \ldots. \tag{4.12}$$

$$f^D = \frac{\Delta\delta\Delta}{3g_F\mu_B\mathcal{B}_{\rm rot}} + 3\delta g\mu_B\mathcal{B}_{\rm rot} - \frac{\Delta^2}{2(3g_F\mu_B\mathcal{B}_{\rm rot})}\frac{\delta g}{g_F} + \ldots., \tag{4.13}$$

$$f^R = \alpha\omega_{rot}\frac{3(\Delta^2+\delta\Delta^2)}{(3g_F\mu_B\mathcal{B}_{\rm rot})^2}\frac{\delta\mathcal{B}}{\mathcal{B}_{\rm rot}} - \alpha\omega_{rot}\frac{27\Delta^2\delta\Delta^2}{(3g_F\mu_B\mathcal{B}_{\rm rot})^4}\frac{\delta\mathcal{B}}{\mathcal{B}_{\rm rot}} + \ldots., \tag{4.14}$$

$$f^{BR} = 3\alpha\omega_{rot} - 3\alpha\omega_{rot}\frac{\Delta^2+\delta\Delta^2}{2(3g_F\mu_B\mathcal{B}_{\rm rot})^2} + 3\alpha\omega_{rot}\frac{9\Delta^2\delta\Delta^2}{4(3g_F\mu_B\mathcal{B}_{\rm rot})^4} + \ldots. \tag{4.15}$$

$$f^{DR} = 3\alpha\omega_{rot}\frac{3g_F\mu_B\delta B\delta\Delta}{(3g_F\mu_B\mathcal{B}_{\rm rot})^3} + 3\alpha\omega_{rot}\frac{2d_e\mathcal{E}_{\rm eff}\Delta^2}{(3g_F\mu_B\mathcal{B}_{\rm rot})^3} + \ldots. \tag{4.16}$$

$$f^{BDR} = -3\alpha\omega_{rot}\frac{\Delta\delta\Delta - (\Delta^2+\delta\Delta^2)(\delta g/g_F)}{(3g_F\mu_B\mathcal{B}_{\rm rot})^2} + \ldots. \tag{4.17}$$

$$f^{BD} = 3g_F\mu_B\delta\mathcal{B}\left(\frac{\delta g}{g_F} - \frac{\Delta\delta\Delta}{(3g_F\mu_B\mathcal{B}_{\rm rot})^2}\left(1 + 3\left(\frac{3\alpha\omega_{rot}}{3g_F\mu_B\mathcal{B}_{\rm rot}}\right)^2\right)\right) + 2d_e\mathcal{E}_{\rm eff} + \ldots. \tag{4.18}$$

We have expanded the expressions for the frequency combinations out to second order in all of the parameters included in eq. (4.1) and truncated the series at a level where the contribution for the remaining terms, for a realistic choice of parameters, falls below 10^{-3} relative to the leading

term, or 1 μHz, whichever is smaller. The expansions in eq. (4.11) through eq. (4.18) will form the basis of our understanding of systematic effects in the following sections. They were derived from eq. (4.1), and any terms not included in the original effective two-state Hamiltonian (e.g. oscillating magnetic fields transverse to the internuclear axis), will not appear in these equations. However, eq. (4.1) represents a reasonable basis of effects to consider, and any additional effects can be considered as corrections to the original Hamiltonian, and included in the expansions in eq. (4.11) through eq. (4.18) as similar corrections.

4.1.1 Strategy

At this point we should discuss strategy. Our objective is to measure f^{BD} with as much sensitivity as possible, and also to be able to place good upper bounds on terms that might accompany $d_e\mathcal{E}_{\text{eff}}$ in f^{BD}. The expression eq. (4.18) includes terms that, under standard operating parameters of the experiment, extend down to 10^{-31} $e\cdot$cm. There are terms included that are larger than $d_e\mathcal{E}_{\text{eff}}$, and they must be accounted for. The larger worry is that some small anomaly will also enter into f^{BD} in a hitherto unanticipated way at the $< 10^{-28}$ $e\cdot$cm level. Systematics that enter at the same level as the statistical sensitivity of the experiment after a 100 hour run will be incredibly difficult to differentiate from an EDM. The way to smoke them out and head them off is to operate the experiment in a deliberate way to increase the size of the systematic effects. For example, typically we will operate the experiment between pairs of Helmholtz coils designed to null out Earth's magnetic field. We can use these same coils to apply a 5 Gauss field, which is an order of magnitude larger than Earth's field. Additionally, we have the other frequency linear combinations besides f^{BD} to aid us. If applying a large magnetic field in the lab frame has some effect that looks like a non-reversing magnetic field in the rotating frame, then it will show up in f^{B} anywhere from 100 to 1000 times larger, depending on the exact set of experimental parameters. We have a good understanding of the leading order effects in eq. (4.11) through eq. (4.18) due to the terms that are included in the effective two state Hamiltonian, eq. (4.1). Any effect that is not already taken into account in the effective two state Hamiltonian will be much more visible in

the other frequency linear combinations. Moreover, there are data channels at our disposal other than frequency. Recalling eq. (3.26), there are up to four other parameters that can be extracted from a Ramsey fringe, the initial phase ϕ, the initial contrast $\mathcal{C}_0$, the offset o, and the coherence time τ. The most statistically sensitive times to take Ramsey fringe data are typically at $t < \tau$, and as such we don't typically get good measurements of τ, but for every Ramsey fringe frequency measurement there is an accompanying ϕ, $\mathcal{C}$, and o measurement. These data channels can also be separated into different linearly independent components as was done with frequency above, which can be helpful in diagnosing systematics that affect the initial state preparation or $\pi/2$ pulses. These quantities are difficult to predict analytically, so we treat them numerically. Generally all of the linear combinations of ϕ, $\mathcal{C}$, and o will be zero, with the exception of the total sum linear combination. When examining systematics we will take special note of any time these channels deviate from zero.

4.2 Understood systematic effects

There are several effects that we can immediately predict from eq. (4.18), in particular the effects due to differential g-factor δg, and the effect of rotational coupling Δ, and $\delta\Delta$. Using the strategies outlined above we can characterise and measure these effects.

4.2.1 Differential g-factor

The first systematic effect we will consider is the term in f^{BD}, $3g_F\mu_B\delta\mathcal{B}(\delta g/g_F)$. We can correct for this term if the dominant contribution to f^B is $3g_F\mu_B\delta\mathcal{B}$. This is a good approximation if the following conditions are met:

- $\Delta^2 + \delta\Delta^2 \ll 2(f^0)^2$,
- $3\alpha\omega_{rot} \ll f^0$,

where we have substituted the leading order contribution to $f^0 = 3g_F\mu_B\mathcal{B}_{\text{rot}}$ into eq. (4.12). In order to achieve good contrast $\pi/2$ pulses we already operate with $f^0 > \Delta > \delta\Delta$. The Berry's phase

α due to things like the axial electric field in the trap will oscillate at the axial trap frequency ω_z, and so the contribution to eq. (4.1) will be a phase modulation at ω_z, as discussed in section 3.2.1.1, and not a frequency shift. As long as α oscillates around a central value of zero, then the contribution to the frequency linear combinations eq. (4.11) through eq. (4.18) will be zero as well. Therefore measurements of f^B can be used to provide a good estimate of $3g_F\mu_B\delta\mathcal{B}$ to use in correcting f^{BD}. The other piece of information we need for this correction of $3g_F\mu_B\delta\mathcal{B}(\delta g/g_F)$ is $\delta g/g_F$, the fractional differential g-factor between the upper and lower doublets. This differential g-factor arises from two different mechanisms. The first is mixing from ${}^3\Delta_1, J = 2$ states into the $J = 1$ states. Because the upper Λ-doublet is closer to the $J = 2$ than the lower doublet by $2d_{mf}\mathcal{E}_{\rm rot}$, we expect a differential effect on the order of the ratio of the rotational splitting $4B_e$ to the $J = 1$ Stark splitting $d_{mf}\mathcal{E}_{\rm rot}$. The exact analytical expression can be found in [42],

$$\frac{\delta g}{g_F} = \sum_{J'=2}\sum_{F'=\{3/2,5/2\}} \frac{d_{mf}\mathcal{E}_{\rm rot}}{B_e(J+1)}\frac{1/\gamma_F}{\Omega}[F,F',J,J']^2 \begin{pmatrix} F & 1 & F' \\ -m_F & 0 & m_F \end{pmatrix}^2 \begin{pmatrix} J & 1 & J' \\ -\Omega & 0 & \Omega \end{pmatrix}^2 \begin{Bmatrix} F' & J' & I \\ J & F & 1 \end{Bmatrix}^2, \tag{4.19}$$

$$= \frac{9d_{mf}\mathcal{E}_{\rm rot}}{40B_e}. \tag{4.20}$$

This is about 10^{-3} for a 24 V/cm electric field. The other contribution to $\delta g/g_F$ comes from Stark mixing within the $J = 1$ states. At large electric fields the $m_F = \pm 1/2$ states in the $F = 3/2$ hyperfine level mix with the $m_F = \pm 1/2$ states in the $F = 1/2$ level. Because the upper doublet states are closer to the $F = 1/2$ states than the lower doublet the perturbation is more pronounced, and via rotation induced coupling to the $m_F = \pm 3/2$ states there is a differential g-factor. We expect this to scale like $(\omega_{\rm rot}^2/(d_m f\mathcal{E}_{\rm rot}))^2(d_m f\mathcal{E}_{\rm rot}/E_{HF})$. Calculating this difference out to three orders in perturbation theory we find that

$$\frac{\delta g}{g_F} = \frac{9}{2}\left(\frac{\omega_{\rm rot}}{d_{mf}\mathcal{E}_{\rm rot}}\right)^2\frac{d_{mf}\mathcal{E}_{\rm rot}}{E_{HF}}, \tag{4.21}$$

which for the parameters in table A.1 is about 1.4×10^{-4}. We expect the combined effect to be on the order of 10^{-3} for our typical electric field magnitude and frequency. As we will discuss below, we

can experimentally measure this difference by looking at the component of Ramsey fringe frequency that changes sign with the doublet switch. We measure $\delta_g/g_F = 0.0008(1)$. Additionally, numerical diagonalization of a 32 state Hamiltonian comprising the $^3\Delta_1 J = 1$ and $J = 2$ predicts a combined $\delta g/g_F$ that is 0.000993 for the parameters in table A.1, see fig. 4.1.

4.2.2 Effective differential g-factor

There is another systematic term that looks similar to a differential g-factor, but arises from a different mechanism. This is the term $f^{BD} = (\Delta\delta\Delta/3g_F\mu_B\mathcal{B}_{\rm rot})(\delta\mathcal{B}/\mathcal{B}_{\rm rot})$. This arises from the difference in the rotation induced coupling between $m_F = \pm 3/2$ states due to the hyperfine mixing of the $m_F = \pm 1/2$ states, quantified in the term $\delta\Delta$. This term is distinct from the $\delta g/g_F$ term above in that it will also produce a systematic dependence of f^{BD} on f^B for effects other than the Zeeman interaction, such as effects arising from geometric phase. For example, a geometric phase term that didn't change sign under switching rotation direction, $m_F\alpha|\omega_{rot}|$, could yield a systematic in f^B and f^{BD} that would look like

$$f^B = 3\alpha|\omega_{rot}|, \tag{4.22}$$

$$f^{BD} = 3\alpha|\omega_{rot}|\frac{\Delta\delta\Delta}{(3g_F\mu_B\mathcal{B}_{\rm rot})^2}. \tag{4.23}$$

Effects that might look like this could be imperfect reversals in rotation, such as components fo $\mathcal{E}_{\rm rot}$ that are different for the two rotation directions. This can also potentially be used as a method of distinguishing the effect that arises from the Zeeman interaction (e.g. non-reversing magnetic fields) from something else. Fortunately, this so-called "effective" δg has a strong inverse dependence on the Ramsey fringe frequency, and at a frequency of 70 Hz it is comparable to the Zeeman differential g-factor. This presents an interesting trade-off between statistical sensitivity and systematic error susceptibility. Spatial inhomogeneity of $\mathcal{E}_{\rm rot}$ and $\mathcal{B}_{\rm rot}$ in the trap causes a decoherence rate that scales with frequency, effectively causing decoherence after a fixed number of periods. For maximum coherence time we are compelled to operate at low Ramsey fringe frequencies. However, systematic effects due to higher order terms such as eq. (4.23) have inverse dependence on frequency. The

Figure 4.1: Measurement of $\delta g/g_F$ and $\Delta\delta\Delta$ by varying the applied $\boldsymbol{\nabla}\mathcal{B}$ to vary the average Ramsey fringe frequency across a range of about 20 Hz to 300 Hz and comparing the component of the frequency that is odd under change of Λ-doublet (f^D) with the average frequency (f^0). This was done under the conditions table A.1. The effect in the f^D channel is the combination of several effects, from eq. (4.19), eq. (4.21), and eq. (4.24). Numerical theory on a 32 state Hamiltonian comprising the $^3\Delta_1 J = 1$ and $J = 2$ states is in good agreement with the data.

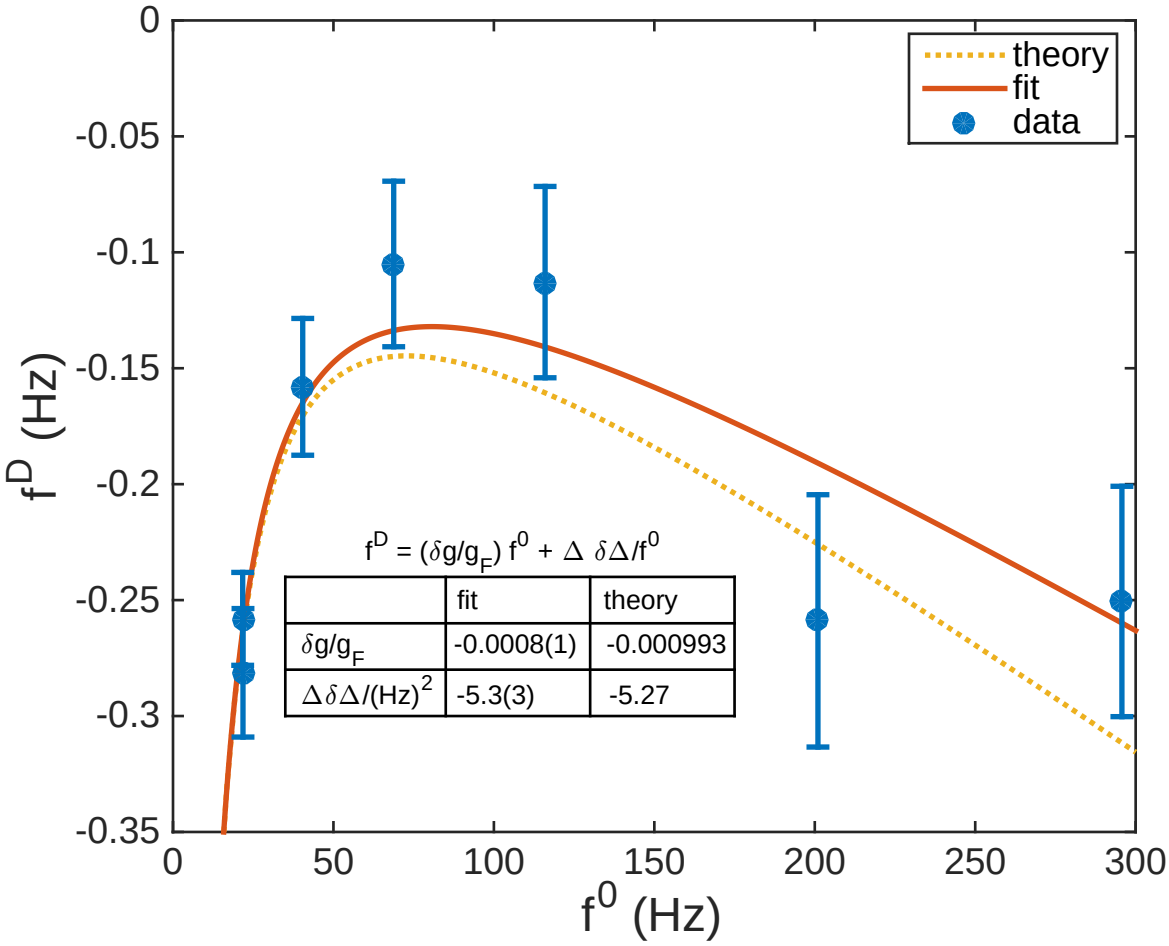

ramifications of this trade-off will be explored in chapter 5.

In total, for effects arising from the Zeeman interaction, the "effective" g-factor is

$$\frac{\delta g_{\text{eff}}}{g_F} = \frac{\delta g}{g_F} - \frac{\Delta\delta\Delta}{(f^0)^2}. \tag{4.24}$$

To characterize this term for a particular ω_{rot} and $\mathcal{E}_{\text{rot}}$, we can choose parameters from table A.1 and take several blocks of Ramsey fringes with varying fringe frequencies, and compare f^D to f^0, as in fig. 4.1, noting that to leading order, f^D/f^0 equals the expression in eq. (4.24). This allows us to extract measurements of $\delta g/g_F = -0.0008(1)$ and the product $\Delta\delta\Delta = -5.3(3)\ (\text{Hz})^2$. This agrees quite well with a numerical calculation of $\delta g/g_F = -0.000993$ and $\Delta\delta\Delta = -5.27\ (\text{Hz})^2$, a zero free parameter calculation that only relies on measured values of g_F, E_{HF}, d_{mf}, and ω_{rot}.

4.2.3 Non reversing magnetic field

From the previous section it should be clear that a non reversing magnetic field, δB, can cause a systematic error in the EDM channel f^{BD}. Because the frequency linear combination f^0 averages over both directions of the applied rotating magnetic field no residue of δB will appear there, but instead will appear in f^B, the component of the frequency that is odd under magnetic field reversal. We will refer to f^B as the "non-reversing magnetic field" channel, as non-reversing magnetic fields are the dominant term in f^B, see eq. (4.12), and below

$$f^B = 3g_F\mu_B\mathcal{B}_{\text{rot}}\left(\frac{\delta\mathcal{B}}{\mathcal{B}_{\text{rot}}}\right) + \dots. \tag{4.25}$$

The non-reversing magnetic field appears in f^{BD} suppressed by a factor of $\delta g_{\text{eff}}/g_F$,

$$f^{BD} = 2d_e\mathcal{E}_{\text{eff}} + 3g_F\mu_B\mathcal{B}_{\text{rot}}\left(\frac{\delta\mathcal{B}}{\mathcal{B}_{\text{rot}}}\right)\left(\frac{\delta g}{g_F} - \frac{\Delta\delta\Delta}{(3g_F\mu_B\mathcal{B}_{\text{rot}})^2}\right) \approx 2d_e\mathcal{E}_{\text{eff}} + f^B\frac{\delta g_{eff}}{g_F}, \tag{4.26}$$

and we see that f^{BD} should have a linear relationship with f^B. We can test the validity of this relationship by intentionally creating a large δB by deliberately making our magnetic field reversals bad. We can quantify this effect with f^B, and we can observe the systematic shift in f^{BD}, the EDM channel. Because we can easily vary f^B by tens of Hz, we can expect to see a shift in the EDM channel on the order of hundreds of mHz, as in fig. 4.2. Several other experiments have confirmed

that $d_e < 10^{-27} e$ cm, which places an upper bound on $d_e \mathcal{E}_{\text{eff}}$ being less than about 10 mHz, so this term can be neglected in comparison to the > 100 mHz shifts observed.

There are several sources of non-reversing magnetic field. The most obvious is any incomplete magnetic field reversal on our part. We apply $\mathcal{B}_{\text{rot}}$ by applying current to a pair of coils in an anti-Helmholtz configuration to generate a quadrupole gradient field $\vec{\boldsymbol{\nabla}\mathcal{B}} = \boldsymbol{\nabla}\mathcal{B}(2z\hat{z} - x\hat{x} + -y\hat{y})$ centered at the trap center. Due to the circular motion of the ions in the trap this produces the effect in the lab frame of reference of a rotating magnetic field $\mathcal{B}_{\text{rot}}$ that is equal to $r_{\text{rot}}\boldsymbol{\nabla}\mathcal{B}$, where r_{rot} is the radius of the circular micromotion due to $\mathcal{E}_{\text{rot}}$. We choose our quantization axis to point along the electric field, which points from the ion to the center of the ion's circular orbit, and we define $+\boldsymbol{\nabla}\mathcal{B}$ and $+\mathcal{B}_{\text{rot}}$ as pointing along the electric field, and $-\boldsymbol{\nabla}\mathcal{B}$ and $-\mathcal{B}_{\text{rot}}$ as pointing against the electric field. We switch the direction of $\mathcal{B}_{\text{rot}}$ by changing the sign of $\boldsymbol{\nabla}\mathcal{B}$, which is done by reversing the direction of the current through the quadrupole coils. The current is applied using a programmable bipolar current source controlled by an external voltage from a digital to analog converter. In addition to the current source internal monitoring we use an external Hall probe to measure the applied current. Offsets and errors in any of the monitoring devices may contribute to a δB, as well as any offsets in current or the position of the coils.

An additional source of $\delta\mathcal{B}$ is due to static gradients. Because $\mathcal{B}_{\text{rot}}$ is created by applied $\boldsymbol{\nabla}\mathcal{B}$, any static quadrupole gradient $\boldsymbol{\nabla}\mathcal{B}_{\text{static}}$ can contribute to a $\delta B = \boldsymbol{\nabla}\mathcal{B}_{\text{static}} r_{\text{rot}}$. Higher order multipoles can contribute to spatial inhomogeneity of δB. A quick glance at the experiment reveals several potential sources of $\boldsymbol{\nabla}\mathcal{B}_{\text{static}}$. The ion trap is inside a stainless steel vacuum chamber constructed of several nominally nonmagnetic stainless steel alloy tubes that have been welded together. The ion trap itself is made of two large aluminum end cap electrodes and 6 stainless steel electrodes that have been welded to steel rods. Stainless steel has the potential to be magnetized and produce a static gradient, and in particular stainless steel welds have the potential to become ferromagnetic because of the introduction of filler material into the weld that is of a different crystal structure. Finally, the entire experiment sits on top of a stainless steel optical table that has become permanently magnetized from years of abuse.

Figure 4.2: A non-reversing magnetic field is an EDM mimicking systematic effect. From eq. (4.12) and eq. (4.18) we see that a non-reversing magnetic field $\delta\mathcal{B}$ will appear in the f^{BD} frequency linear combination with a δg_{eff} coefficient. We also observe that $\delta\mathcal{B}$ appears in the non-reversing magnetic field linear combination, f^B, with the much larger g_F coefficient. This correlation is shown below, where the application of a large second order magnetic field gradient in the axial trap direction coupled with displacement along that direction resulted in a large effective non-reversing magnetic field, appearing in the the f^B channel as a ± 15 Hz shift. In the EDM channel, f^{BD}, this effect is suppressed to the ± 400 mHz level. For this particular δg_{eff}, experimentally shimming f^B to ± 30 mHz will result in an uncorrected systematic shift of 800μHz in the EDM channel. As discussed in section 5.1.4, this contribution may be characterized and subtracted away. Additionally, operating with smaller $\Delta\delta\Delta$, and larger Ramsey fringe frequency, $3g_F\mu_B\mathcal{B}_{\text{rot}}$, can reduce δg_{eff} and suppress this effect even more.

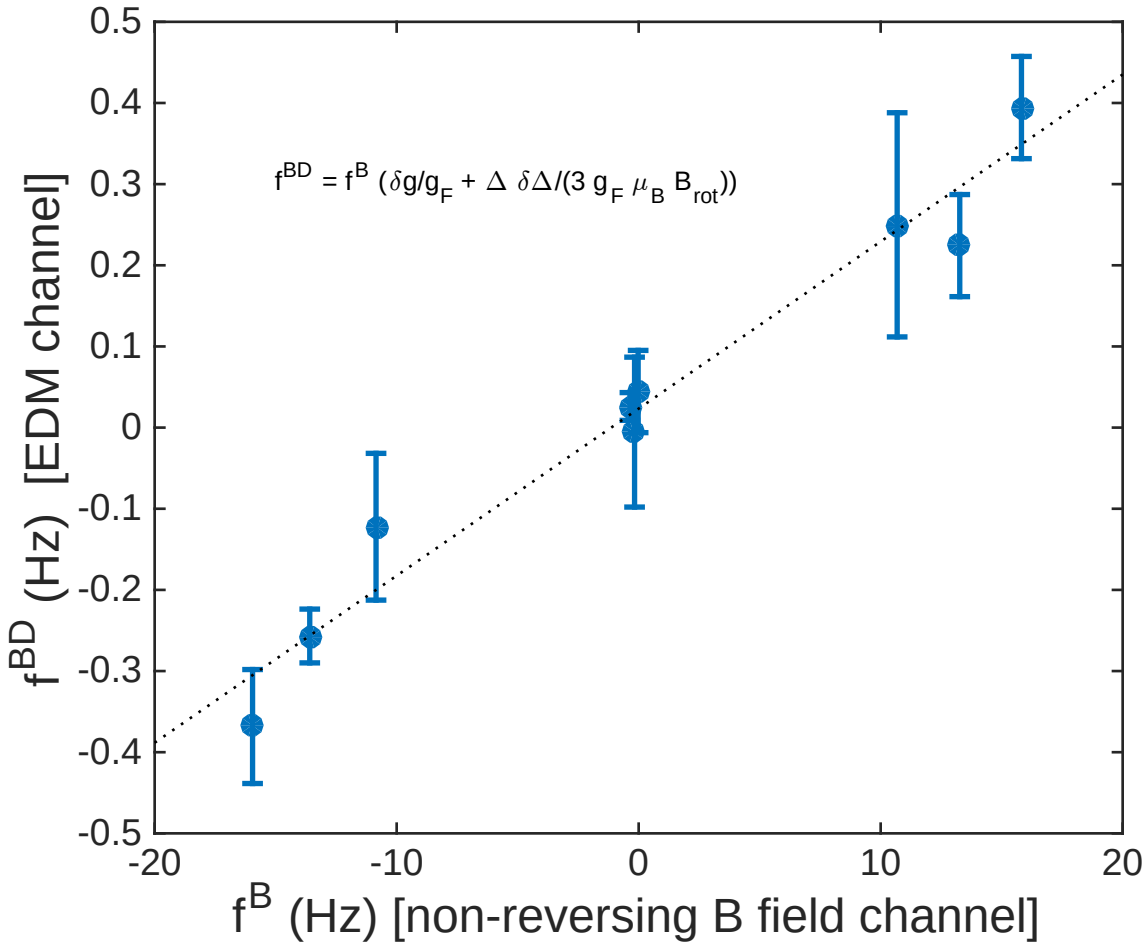

For the standard values of experiment parameters in table A.1, a static gradient at the center of the ion trap of as little as 2 mGauss/cm can contribute a 630 mHz shift in f^B, which translates to a 0.5 mHz shift in f^{BD} taking only $\delta g/g_F$ into account, which is a 5×10^{-29} $e$cm effect. Welds on the vacuum chamber typically have very high order gradients that are $10-20$ mGauss magnetic field 1 mm away, which quickly drops to the μGauss level 1 cm away. The optical table magnetic field varies considerably over the length of the table, with local "hot spots", corresponding to welds on the edge and at various support points on the interior. Several cm away from the table the gradient become smoother, and the field component in the z direction is about $(18(z/\text{cm}) - 0.6(z/\text{cm})^2)$mGauss. The center of the ion trap is about 28 cm from the table, which corresponds to a 1.2 mGauss/cm gradient. We also measured the gradient at the center of the trapping region by scanning the position of a magneto-resistive magnetometer device while the chamber was vented to atmosphere. These measurements show the background gradient to be on the order of ~ 2 mGauss/cm. At the same time we discovered the presence of a large static gradient due to a cold cathode type vacuum gauge. The cold cathode works by circulating an electron plasma in a magnetic field on the order of 1000 Gauss. Even though the gauge was more than a a meter away from the center of the trap, the gradient experienced there was > 5 mGauss/cm. This was an easy problem to solve, we simply had to remove the gauge and replace it with a hot filament gauge that did not produce a large magnetic field.

These static gradients pose two problems. The first is that they have the effect of a non-reversing magnetic field, which is an EDM mimicking systematic. The 1.2 mGauss/cm gradient of the stainless steel table produces a 3×10^{-29} $e\cdot$cm systematic. Fortunately we can use f^B as a realtime diagnostic of the non-reversing magnetic field, and deliberately apply an oppositely signed quadrupole gradient to cancel this effect out, as in fig. 4.3. We can easily apply a gradient to shim f^B to less than 50 mHz, which is 40μHz in f^{BD}, a systematic $\sim 3 \times 10^{-30}$ $e\cdot$cm. After removing the cold cathode gauge we saw a change in the required magnetic field gradient required to yield a nominally zero f^B of 4.9 mGauss/cm, or 2.9 Hz.

We must be a bit cautious with this technique, as it relies on us having exact knowledge of the

Figure 4.3: A non-reversing magnetic field can be measured by f^B, the non-reversing magnetic frequency combination. The rotating frame magnetic field that the ions experience is the result of the combination effect of an applied magnetic field gradient and the circular ion micromotion. The rotating frame magnetic field direction is reversed by applying a lab frame magnetic field gradient of the opposite sign, effectively done by reversing the direction of current through a pair of coils in an anti-Helmholtz configuration. By deliberately performing incomplete reversals of the current we are able to apply a non-reversing gradient, $\boldsymbol{\nabla}\mathcal{B}$. With the freedom to apply a $\boldsymbol{\nabla}\mathcal{B}$ of our choice, we are able to shim the measured f^B to within 30 mHz of zero.

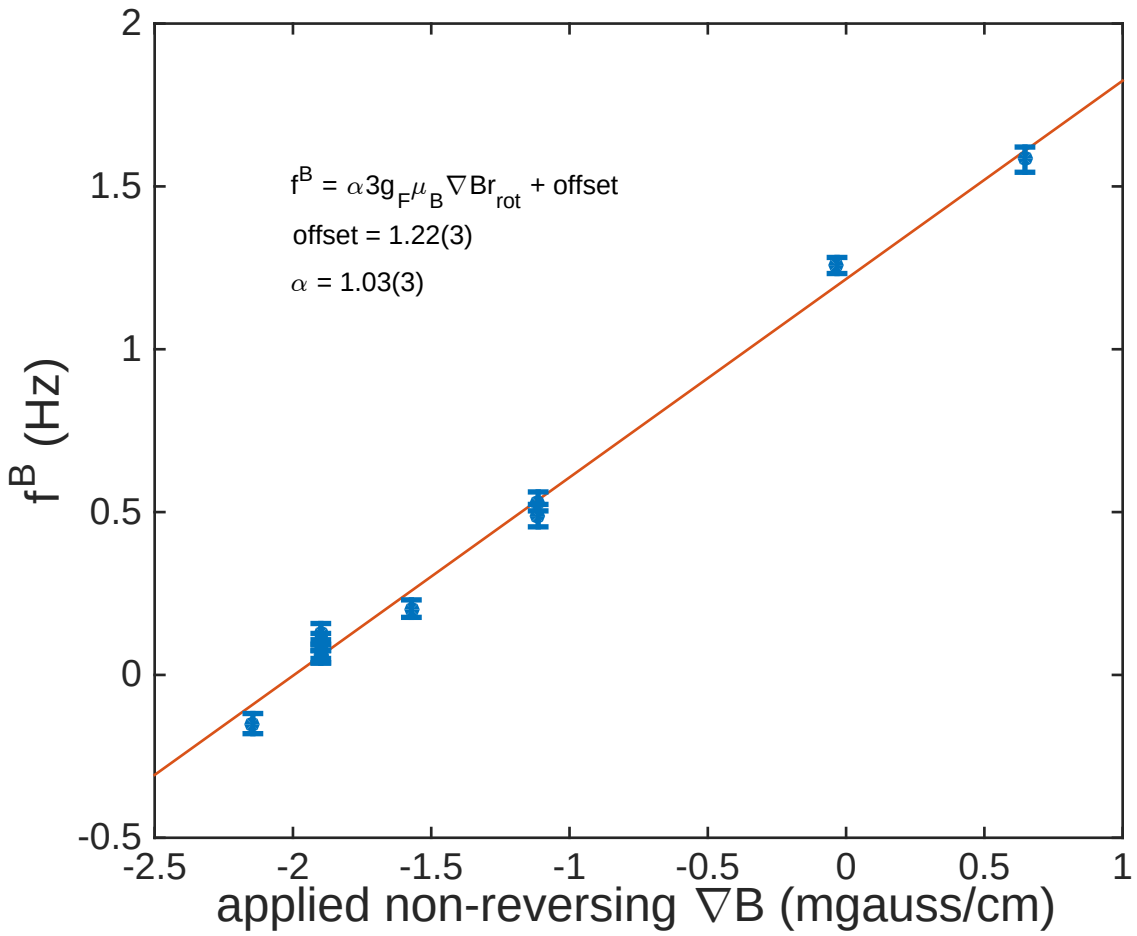

relationship between f^B and f^{BD}. This works because we know that a non-reversing magnetic field can be described by $\delta\mathcal{B}$ in eq. (4.1), and the correlation between the effects in f^B and f^{BD} is well described by the effective difference in g-factor, in eq. (4.24). However, an effect due to something other than the Zeeman interaction, if it is odd under reversal of magnetic field, will appear in f^B and f^{BD}, but with a different correlation between the two channels than a non-reversing magnetic field, as in eq. (4.22). If we add in a new non-reversing magnetic field to null out the signal in f^B, we could inadvertently introduce a new systematic on the order of $\sim (\delta g/g_F) f^B$.

The second problem with the static gradients is that perhaps they aren't so static. This might be caused by changing parameters in the lab. Temperature changes could potentially cause the magnetization of the optical table and the welds to drift. If they fluctuate over fast time scales this will decrease the coherence time of the Ramsey fringes by adding noise onto the frequency. What is more probable is that they fluctuate over longer timescales. We observed fluctuations of f^B with a standard deviation of $\sigma = 2.8$ Hz over the span of several days. After removing the cold cathode gauge causing the large stray gradient we saw a reduction in these fluctuations to a standard deviation of $\sigma = 0.74$ Hz. The problem arises when the gradients fluctuate over a timescale comparable to the time it takes the experiment to acquire a Ramsey fringe. In the proposed scheme in section 3.2.4, maximal sensitivity was assumed by the ability to be able to know the frequency well enough to only take data points on the zero crossings of the Ramsey fringes. This required two measurements: one rough and fast measurement to get an accurate enough idea of the frequency to allow us to dial in the times between the $\pi/2$ pulses for a second, longer, high sensitivity measurement. If on a similar timescale the background gradients drift enough to cause the frequency to change by a quarter of a period, then instead of collecting data on the zero crossing of a fringe, with maximal sensitivity, we will collect data on the peak of a fringe, with minimal sensitivity. A one quarter fringe slip at 500 ms corresponds to a 0.5 Hz, or 0.8 mGauss/cm drift. Unfortunately this is about at the same level of our measured day to day variations of f^B. In order to reliably park the experiment on the side of a fringe we require a measurement of f^B that is much faster than a Ramsey fringe measurement time.

Our proposed scheme to measure the background gradients is a cluster of small, inexpensive, magnetoresistive chip scale magnetometers. The HMC5883l is a 3 axis magnetometer made by Honeywell that can measure fields up to ±2 Gauss with a 4 mGauss resolution. It has an integrated 12 bit ADC, and a small 3mmx3mm package. Two of these sensors placed 20 cm apart should be able to measure a gradient with a sensitivity of 0.2 mGauss/cm. Measurements can be made very quickly, in about 1.7s, and should be able to provide information of the background gradients that is sensitive enough for us to apply a corrective gradient in real time. Doing so will allow us to feed forward our measurements to stay locked to the side of a Ramsey fringe. To this end we have constructed an array of 8 magnetometers positioned around the experiment.

A benchmark test of this magnetometer array is presented in fig. 4.4. In this test the six magnetometers placed in the region around the equatorial plane of the ion trap chamber were used. The two other magnetometers, placed above and below the ion trap, had measurements that skewed far from the expected gradients. We determined that this was due to high order magnetic field gradients emanating from the magnetized stainless steel optical table the experiment chamber was mounted to, so we removed these two magnetometers from our data set. The remaining magnetometers can predict 80% of the variation in the measured non-reversing magnetic field channel, but still leave much to be desired in terms of performance. Some of the problems with this system that might account for the unexplained variation are:

(1) The magnetometers were small evaluation boards purchased from Adafruit Industries for $10 a piece. The actual magnetometer chip is designed to be used in portable electronic applications as as digital compass with $\sim 2^\circ$ heading accuracy. The evaluation boards were meant to be used by hobbyists in applications that typically only required roughly identifying magnetic north, and are provided without any calibration. While we did individually calibrate each magnetometer against a reference Helmholtz coil, we found variations in their readings of earth's magnetic field and we found variations in their readings when placed inside a zero-Gauss chamber. Closer scrutiny of the evaluation boards led to the discovery

Figure 4.4: We make measurements of the lab frame residual magnetic field using an array of 6 chip scale magnetometers placed roughly around the equatorial plane of the ion trap chamber. Each device measures the magnetic field along three axes, providing in total 24 magnetic field measurements at 6 distinct locations. This is globally fit to a static magnetic field and 5 linearly independent first order gradients. From the quadrupole gradient we can infer an effective non-reversing magnetic field, and its effect on the non-reversing magnetic field channel, f^B, plotted below on the horizontal axis as $f^B_{\text{magnetometer}}$. This is compared to the actual f^B channel measured via Ramsey spectroscopy. The $f^B_{\text{magnetometer}}$ inferred from the magnetometer array can explain 0.8 of the variation measured in f^B. This is good as a proof of principle of the ability to measure and predict the effect of a non-reversing magnetic field, but to be able to actively cancel out fluctuating non-reversing magnetic fields in real time before a Ramsey measurement is made requires more accuracy. Specific deficiencies of the magnetometer array and their solutions are discussed in the text.

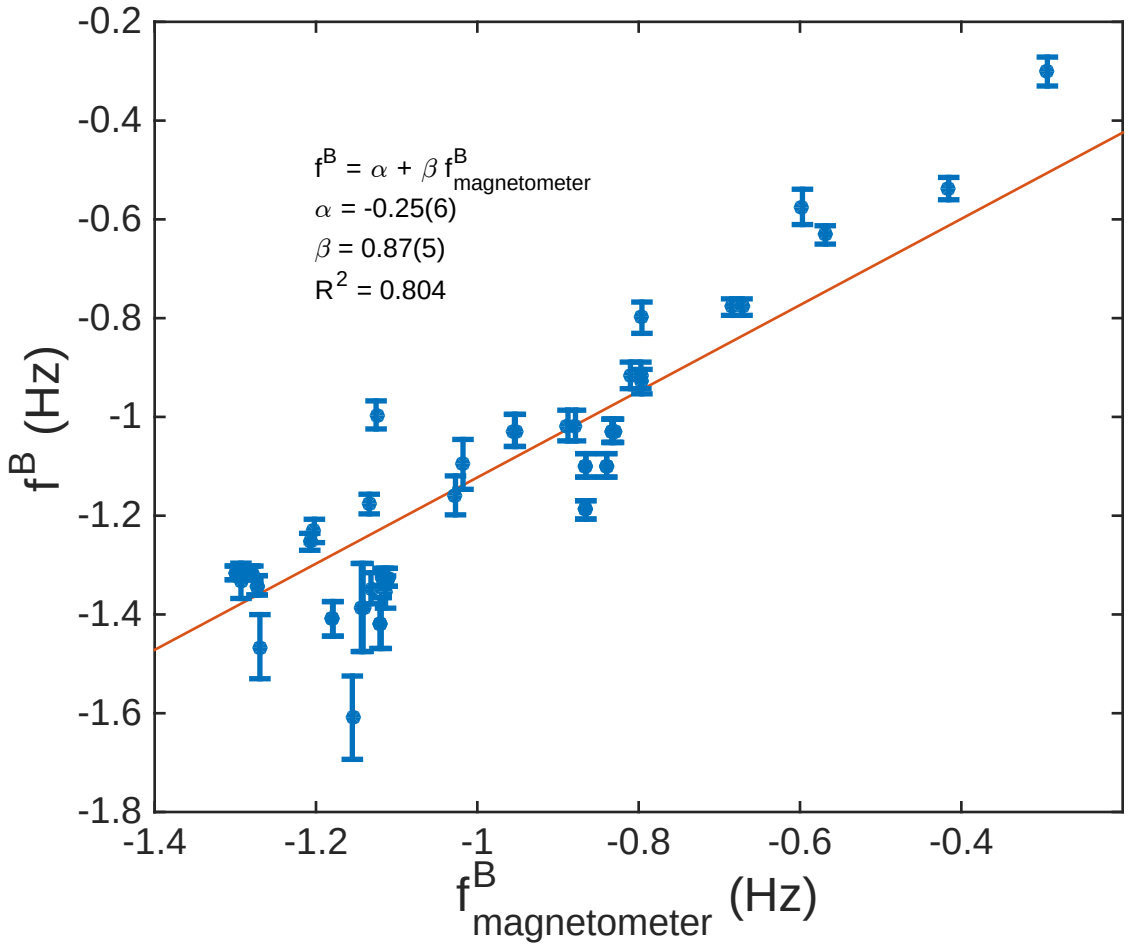

Figure 4.5: The magneto-resistive sensors described in the text. On the upper left is the previous sensor purchased from Adafruit. The components are placed close to the sensor and the PCB contacts are coated in a gold film, contributing to the magnetization of the board. we replaced these with a PCB, shown on the right, with the componets removed from the board and placed on the host side. The connector is now four brass screws, which in addition to providing an electrical connection also locate and position the magnetometer. Eight magnetometers are attached to a motherboard, shown below, which provides power and ground connections and routes the signals of the eight magnetometers to the host microcontroller.

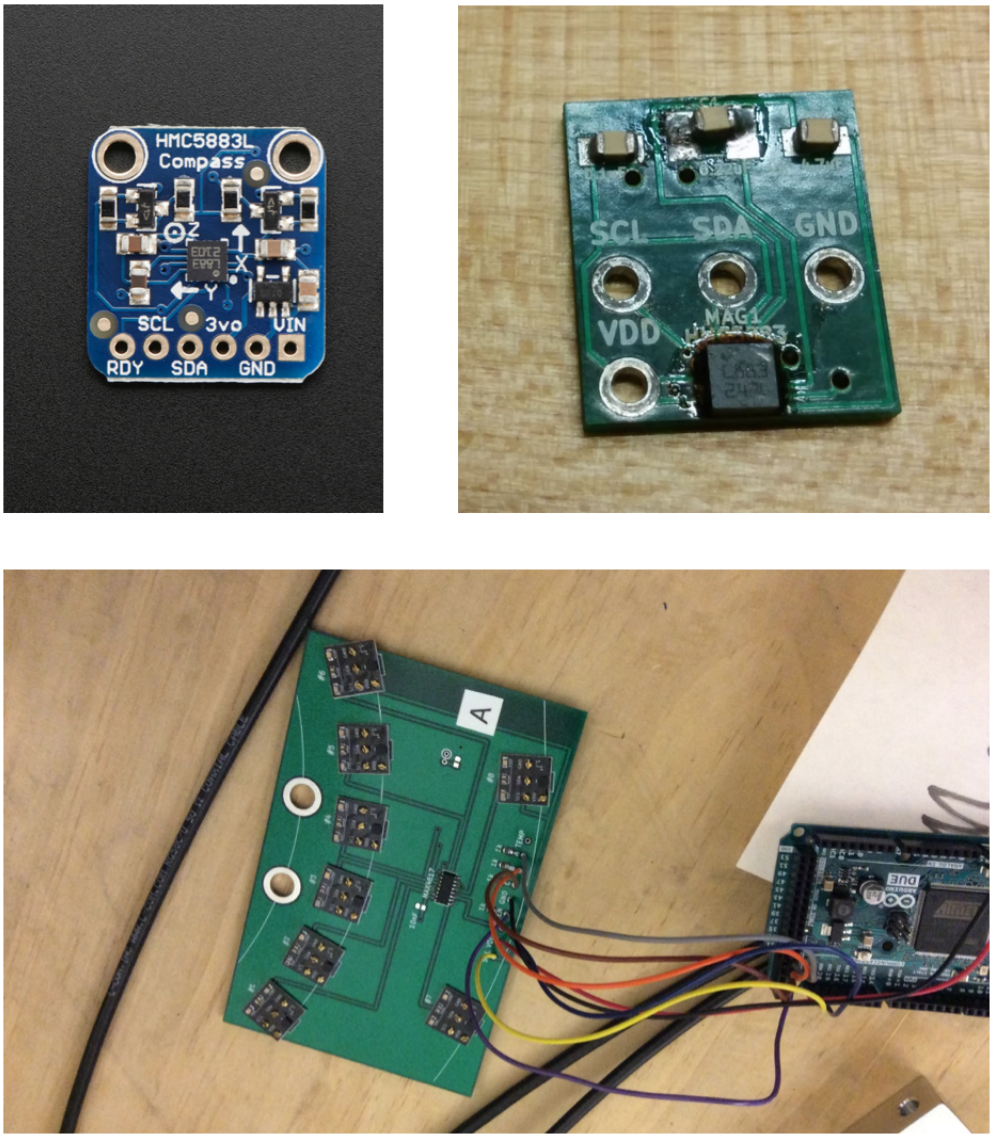

that they were constructed of magnetic materials. The printed circuit board contacts were gold coated, but underneath the layer of gold a layer of nickel was used to adhere the gold plating. The evaluation board also contained a voltage regulator, bypass capacitors, resistors, and transistors to facilitate the logic level conversion from 5V (TTL) to 3.3V (voltage level of magnetometer). All of these components exhibited some amount of magnetism. With the exception of two bypassing capacitors, these components could be removed from the board, or from the circuit entirely. We designed a new PCB for the magnetometer that is not magnetic, and used nonmagnetic surface mount capacitors placed further from the sensor. This new sensor board is already performing with less variability than the Adafruit evaluation board. Additionally, we purchased a single high accuracy three axis fluxgate magnetometer with a NIST traceable calibration and constructed a larger and more uniform calibration coil jig. By placing the magnetoresistive magnetometers next to the high accuracy fluxgate magnetometer in the calibration setup, we can potentially achieve much better calibrations of the magnetometers.

(2) The position and heading information of each magnetometer as mounted around the experiment is not good enough. The magnetometers are mounted through two holes in the evaluation board using brass or nylon screws to aluminum arms mounted to 1" indexed holes in the optical table breadboard. We machined the height of the aluminum arms to place the magnetometer at the desired height. The new PCB design of the magnetometer mounts directly to a larger PCB that is designed to attach directly to the vaccuum chamber that contains the ion trap, providing a much more reliable position reference.

(3) When fitting the 24 magnetic field measurements to the 8 linearly independent 0th and 1st order magnetic field terms we found large variations not explained by the fits, which we interpret as the existence of higher order gradient terms. These higher order gradients along with a position uncertainty can add error to the 0th and 1st order terms we hope to measure. To combat this effect, the second generation magnetometer sensor array design

has increased the number of magnetometers by an order of magnitude. A "motherboard" printed circuit board contains mounting points for 8 magnetometers. The magnetometers attach to the motherboard with 4 brass screws, giving them a well defined position and heading relative to the motherboard, as well as providing the electrical connection for power, ground, signal, and clock. The motherboard also contains a mux to route the communication from the host to each of the 8 magnetometers. Multiple motherboards can be queried for measurements by a host, in this case an Arduino Due microprocessor. We plan to incorporate as many as 6 of these motherboard around the experiment, for a total of 144 independent single axis magnetic field measurements.

This new sensor array is currently being assembled and calibrated. Two motherboard are installed on the experiment currently, and are in the process of being characterized. For more detailed technical information see the Yiqi Ni's Honors Thesis. A discussion of the future benefits of the new sensor array will be continued in section 5.2.

4.2.4 Axial magnetic fields

Because the experiment takes place in a rotating frame, it is primarily sensitive to AC magnetic fields at the rotating frequency, and the effect of temporally constant and spatially uniform magnetic fields are suppressed. We deliberately choose to operate the experiment without any magnetic shielding[42] for two reasons, the first simply being that it is easier not to, and the second being that it would affect the uniformity of our deliberately applied magnetic field gradient. In this section we examine the effect of DC magnetic fields in the rotating frame.

The application of static magnetic fields will shift the various Zeeman sublevels, affecting the strength of the 3rd and 4th order couplings between pairs of $m_F = \pm 3/2$ states in perturbation theory. We will express static lab frame magnetic fields $\vec{\mathcal{B}}_{\text{lab}}$ as $\mathcal{B}_x\hat{x} + \mathcal{B}_y\hat{y} + \mathcal{B}_z\hat{z}$, where $\hat{z}$ is the direction opposite of gravity and $\hat{x}$ and $\hat{y}$ are chosen to align with the radial trap axes. The effect

Figure 4.6: A magnetic field $\mathcal{B}_z$, applied along the axial direction of the trap, parallel to the direction of the rotation vector, results in a shift in f^R and f^{DR}. As described in eq. (4.30), the axial magnetic field shifts the Zeeman sublevels which results in an effective Δ rotational coupling that is increased by a factor of $(1 \pm 3g_F\mu_B\mathcal{B}_z/\omega_{rot})$. The effective rotation of the axial magnetic field removes the degeneracy of the two rotation directions, which is why the effect is odd under the rotation switch R and appears in f^R, and because it modulates Δ, as well as $\delta\Delta$, it also has an effect that is odd under the simultaneous switch of rotation direction and doublet and appears in f^{DR}.

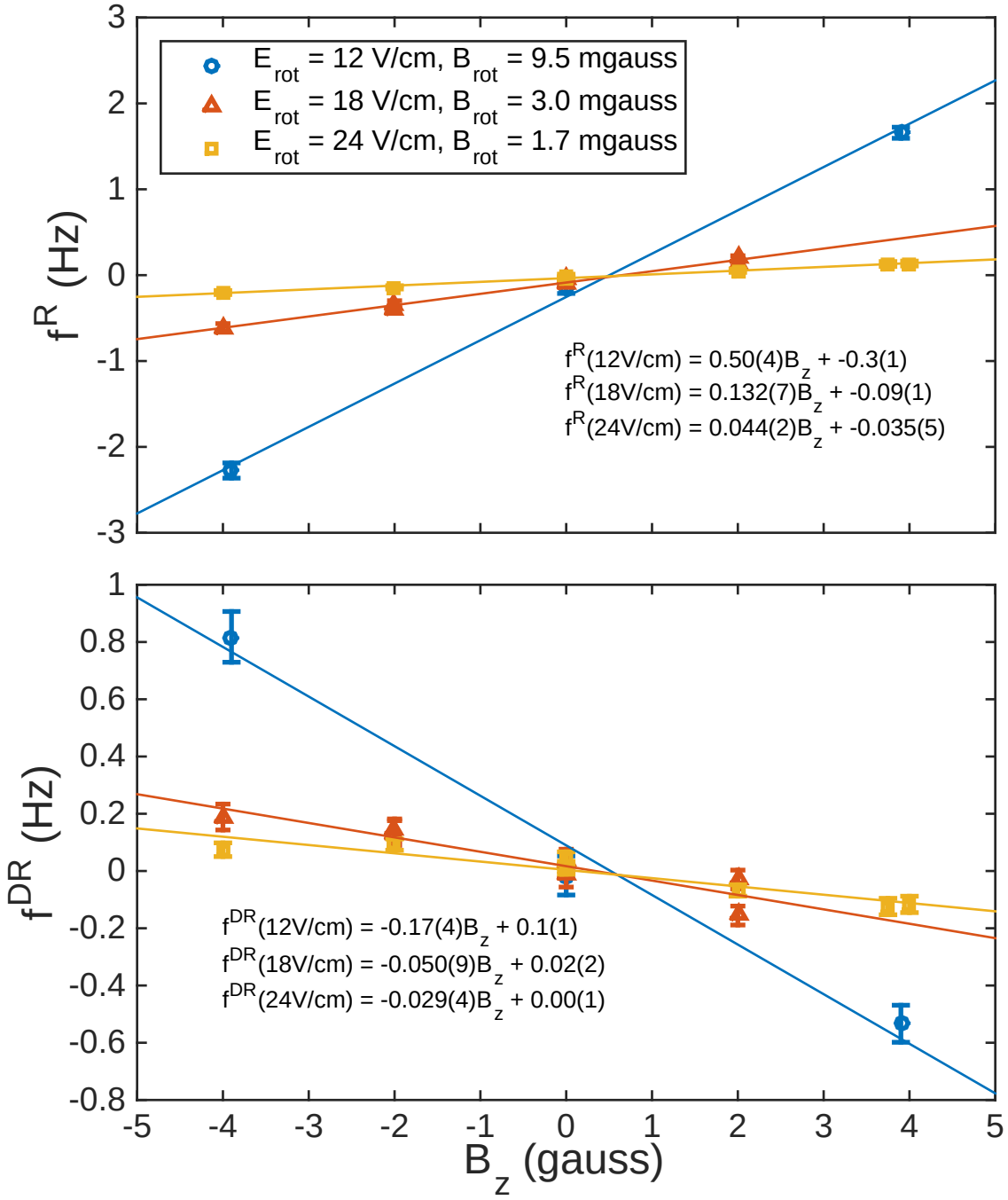

of this on the effective two state Hamiltonian eq. (4.1) is

$$\Delta \rightarrow 27\omega_{ef}\left(\frac{\omega_{rot}+g_F\mu_B(\mathcal{B}_z-i\mathcal{B}_x\sin(\omega_{rot}t)+i\mathcal{B}_y\cos(\omega_{rot}t))}{d_{mf}\mathcal{E}_{\rm rot}}\right)^3, \tag{4.27}$$

$$\begin{aligned}\left.\frac{\delta g}{g_F}\right|_{J=1} =& \frac{9}{2}\left(\frac{\omega_{rot}}{d_{mf}\mathcal{E}_{\rm rot}}\right)^2\left(\frac{d_{mf}\mathcal{E}_{\rm rot}}{E_{HF}}\right),\\ \rightarrow& \frac{9\omega_{rot}^2}{2d_{mf}\mathcal{E}_{\rm rot}E_{HF}}\left(1+\frac{2g_F\mu_B\mathcal{B}_z}{\omega_{rot}}\left(1+\frac{\mathcal{B}_x\cos(\omega_{rot}t)+\mathcal{B}_y\sin(\omega_{rot}t)}{\mathcal{B}_{\rm rot}}\right)\right)+\\ & \frac{9\omega_{rot}^2}{2d_{mf}\mathcal{E}_{\rm rot}E_{HF}}\left(\frac{g_F\mu_B\mathcal{B}_x\cos(\omega_{rot}t)}{\omega_{rot}}\right)\left(\frac{g_F\mu_B\mathcal{B}_y\sin(\omega_{rot}t)}{\omega_{rot}}\right),\end{aligned} \tag{4.28}$$

$$\mathcal{B}_{\rm rot} \rightarrow \mathcal{B}_{\rm rot}+\mathcal{B}_x\cos(\omega_{rot}t)+\mathcal{B}_y\sin(\omega_{rot}t) \tag{4.29}$$

The component of $\delta g/g_F$ due to mixing in the $J=1$ level is perturbed by terms that go as $g_F\mu_B\mathcal{B}_{\rm lab}/\omega_{rot}$. This term only approaches 1 for $\mathcal{B}_{\rm lab} > 10$ Gauss, which is already too large with the current shim coils installed on the experiment, and much larger than the ambient field due to Earth's magnetic field. Moreover, the contribution to $\delta g/g_F$ from $J=1$ mixing is already dominated by the contribution from mixing with $J=2$ states, as in eq. (4.19), so the effect of static lab frame fields on $\delta g/g_F$ can be safely ignored.

We see that the effective mixing between $m_F=\pm 3/2$ states, Δ, is affected by axial magnetic fields in much the same way as it is affected by rotation. This is because the axial magnetic field $\mathcal{B}_z$ is always perpendicular to the quantization axis, chosen to point in the $\hat{n}=\hat{x}\cos(\omega_{rot})+\hat{y}\sin(\omega_{rot})$ direction, and so it will exert a torque on the spin, mixing adjacent m_F states in much the same way that an actual rotation does. The radial magnetic field $\hat{x}\mathcal{B}_x+\hat{y}\mathcal{B}_y$ will torque the molecule whenever it does not point along the quantization axis, and will shift the m_F levels whenever it does, which is why the $\mathcal{B}_x$ and $\mathcal{B}_y$ terms appearing in Δ and $\mathcal{B}_{\rm rot}$ are phase offset by $\pi/2$. Because these terms have a time dependence we can't simply treat them as a frequency, as in section 3.2.1, but we have to explicitly treat the time dependence as in section 3.2.1.1. They will contribute phase modulation to the Zeeman shift and to Δ, which we don't have to worry about for modulations of amplitude smaller than $g_F\mu_B\mathcal{B}_{x,y}/\omega_{\rm rot}$. For now we will focus our attention on the time independent contribution of $\mathcal{B}_z$. The effect of $\mathcal{B}_x$ and $\mathcal{B}_y$ will be treated in section 4.3. Expanding eq. (4.27) to

first order we see

$$\Delta \pm \delta\Delta \rightarrow (\Delta \pm \delta\Delta)\left(1 + \frac{3g_F\mu_B\mathcal{B}_z}{\omega_{rot}}\right) + \dots. \tag{4.30}$$

This term is odd under switches of the electric field rotation direction, R. We expect to see large effects in all of the frequency linear combinations that are odd under the R switch. Also because $\delta\Delta = \frac{3}{8}\Delta\left(\frac{d_{mf}\mathcal{E}_{\rm rot}}{E_{HF}}\right)$, there will be an effect that is odd under reversal of the doublet, because of how $\mathcal{B}_z$ can modulate $\delta\Delta$, so we expect effects in the channels that are odd under doublet switch. Incorporating this effect into the expansions of frequency linear combinations eq. (4.11)-eq. (4.18) we find new terms proportional to $\mathcal{B}_z$, the largest of which are

$$f'^{D} = f^{D} + \frac{\Delta\delta\Delta}{3g_F\mu_B\mathcal{B}_{\rm rot}} 15\left(\frac{g_F\mu_B\mathcal{B}_z}{\omega_{rot}}\right)^2 + \dots., \tag{4.31}$$

$$f'^{BD} = f^{BD} + 3g_F\mu_B\delta\mathcal{B}\frac{\Delta\delta\Delta}{(3g_F\mu_B\mathcal{B}_{\rm rot})^2} 15\left(\frac{g_F\mu_B\mathcal{B}_z}{\omega_{rot}}\right)^2 + \dots., \tag{4.32}$$

$$f'^{R} = f^{R} + \frac{\Delta^2 + \delta\Delta^2}{3g_F\mu_B\mathcal{B}_{\rm rot}} 3\left(\frac{g_F\mu_B\mathcal{B}_z}{\omega_{rot}}\right) + \dots., \tag{4.33}$$

$$f'^{DR} = f^{DR} + \frac{\Delta\delta\Delta}{3g_F\mu_B\mathcal{B}_{\rm rot}} 6\left(\frac{g_F\mu_B\mathcal{B}_z}{\omega_{rot}}\right) + \dots. \tag{4.34}$$

There is also an effect in the f^{BDR} channel, but it is further attenuated by a factor of $\delta\mathcal{B}/\mathcal{B}_{\rm rot}$, so we will neglect it. For typical experimental values, and a 1 Gauss $\mathcal{B}_z$, the term $(g_F\mu_B\mathcal{B}_z/\omega_{rot}) \approx 0.016$. The magnitude of the effect in f^R and f^{DR} are 30 mHz and -20 mHz respectively per mGauss of magnetic field pointing in the same direction as the rotation vector. To validate the existence of these terms we can plot them against the measured effects in the frequency combinations, see fig. 4.7. If the predicted effects in eq. (4.33) and eq. (4.34) are correct we expect to see an exact liner relationship with a coefficient of 1. The effect agrees quite well with what we expect from eq. (4.11)-eq. (4.18).

There will also be an effect that will appear in the f^{BD} channel that is quadratic in the axial magnetic field, eq. (4.32). This term arises because of how the axial magnetic field increases the differential coupling of the two doublets δg, effectively increasing the effective differential g-factor between the two levels, spoiling the suppression of any non-reversing magnetic fields. The

Figure 4.7: The effect of axial magnetic field on f^R and f^{DR} from fig. 4.6 plotted against the axial magnetic field $\mathcal{B}_z$ scaled by the the predicted terms in eq. (4.33) and eq. (4.34). For this data $\omega_{rot} = (2\pi)250$ kHz, and $\Delta, \delta\Delta$, and $\mathcal{B}_{\text{rot}}$ were inferred from the f^D and f^0 channels.

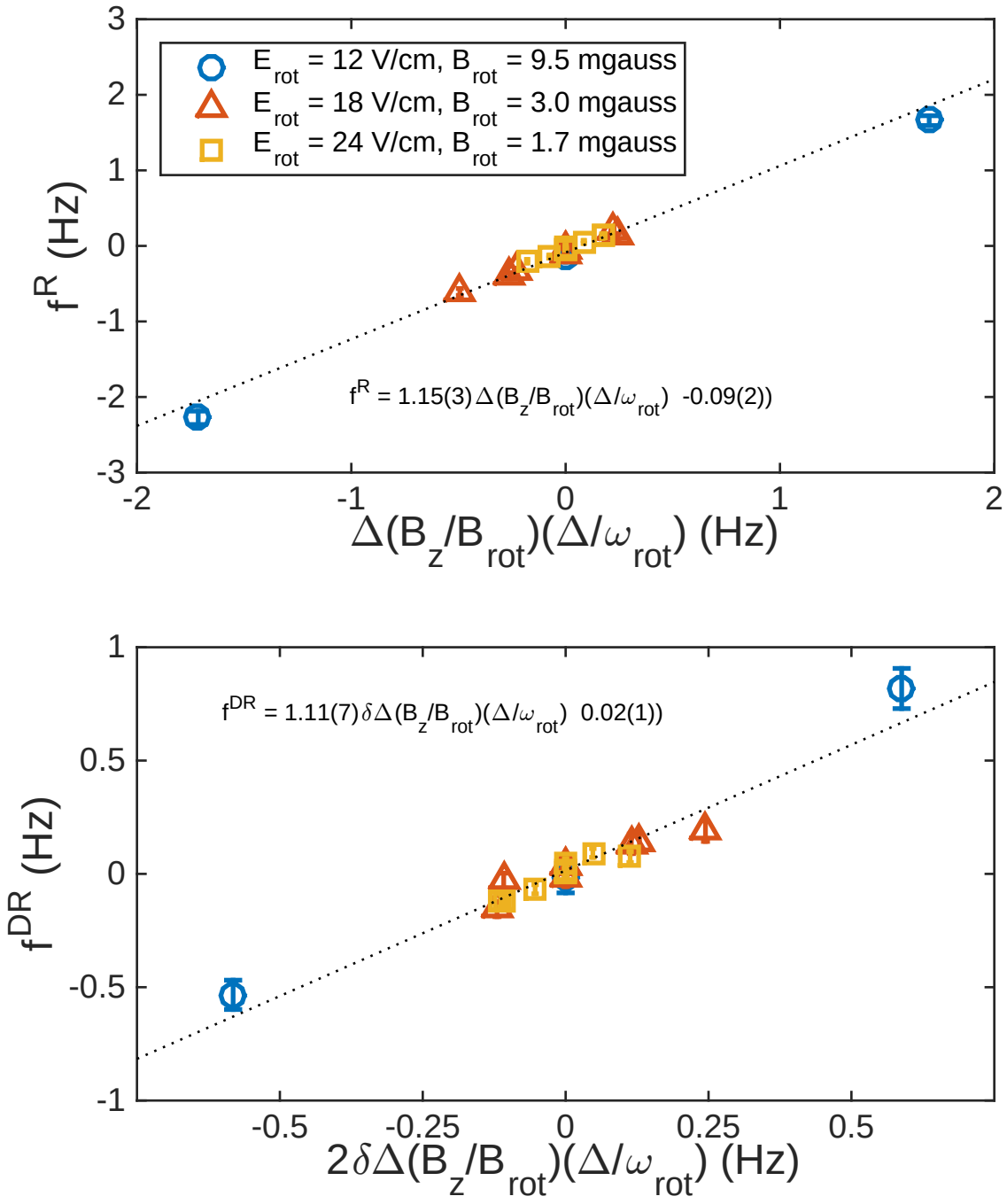

correction to the effective g-factor is

$$\frac{\delta g_{\text{eff}}}{g_F} = \frac{\delta g}{g_F} - \frac{\Delta\delta\Delta}{(3g_F\mu_B\mathcal{B}_{\text{rot}})^2}\left(1 + 15\left(\frac{g_F\mu_B\mathcal{B}_z}{\omega_{rot}}\right)^2\right). \tag{4.35}$$

The correction due to Earth's magnetic field will be smaller than 0.001, and if any attempt is made to cancel Earth's field to even the 10% level, this correction drops to 10^{-4}. For the full Earth's field this effect is a systematic shift on f^{BD} of less than 3μHz, or 5×10^{-31} $e\cdot$cm. In any case, the size of this effect is smaller than the measurement uncertainty on $\delta g/g_F$, so the effect of axial magnetic fields is completely irrelevant from the perspective of systematics for our current level of statistical sensitivity.

Another potential effect of axial magnetic fields is on the statistical sensitivity of the experiment. Because the axial magnetic field affects the coupling between adjacent m_F levels the same way that the rotation of the molecules does, it effectively increases or decreases Δ, the effective coupling between $m_F = \pm 3/2$ levels. Recalling section 3.2.3, this coupling is what is used to perform $\pi/2$ pulses at the beginning and end of the Ramsey sequence. This means that $\mathcal{B}_z$ will detune our $\pi/2$ pulses, which can lead to a decrease in contrast, which will decrease the statistical sensitivity of the experiment. The asymmetry of a Ramsey fringe, taking into account $\pi/2$ pulse timings, is

$$\mathcal{A} = -\sin^2\left(\frac{\Delta}{2\hbar}t_{\pi/2}\right)\cos(2\pi(ft+\phi)) + \cos^2\left(\frac{\Delta}{2\hbar}t_{\pi/2}\right). \tag{4.36}$$

Substituting the modification of Δ due to $\mathcal{B}_z$, ($\Delta \rightarrow \Delta(1 + (3g_F\mu_B\mathcal{B}_z/\omega_{rot})^2)$ into the above assymetry, and then expanding to first order in $\mathcal{B}_z$, we find

$$\mathcal{A} = -\left(1 - \left(\frac{\pi}{2}\frac{3g_F\mu_B\mathcal{B}_z}{\omega_{rot}}\right)^2\right)\cos(2\pi(ft+\phi)) + \left(\frac{\pi}{2}\frac{3g_F\mu_B\mathcal{B}_z}{\omega_{rot}}\right)^2. \tag{4.37}$$

While we do see a quadratic dependence of the Ramsey fringe offset and contrast on $\mathcal{B}_z$, it is roughly a factor of 2 too small, see fig. 4.8. The data agrees better if we remove the factor of $(\pi/2)^2$ from the prediction, although there is no justification for this. As a final note, this will only affect the statistical sensitivity if there is a secular drift in the axial magnetic field between experiments. We typically determine the optimal $\pi/2$ pulse time $t_{\pi/2}$ empirically, scanning $t_{\pi/2}$ until we achieve optimal fringe contrast and offset.

Figure 4.8: An axial magnetic field $\mathcal{B}_z$ mimics a faster or slower electric field rotation, which will change the effective coupling between $m_F = \pm 3/2$ states Δ by a factor of $(1 + (3g_F\mu_B\mathcal{B}_z/\omega_{rot})$. Because the $\pi/2$ pulses of the Ramsey sequence are executed using Δ to rotate into a superposition of $m_F = \pm 3/2$, if the $\pi/2$ pulse timing has previous been tuned to $t_{\pi/2} = \pi\hbar/2\Delta$, then in the presence of an axial magnetic field shifting Δ the $\pi/2$ pulses will now be off of resonance and a contrast and offset will be introduced. The offset will be increased and the contrast will be decreased by a factor of $(3g_F\mu_B\mathcal{B}_z/\omega_{rot})^2$.

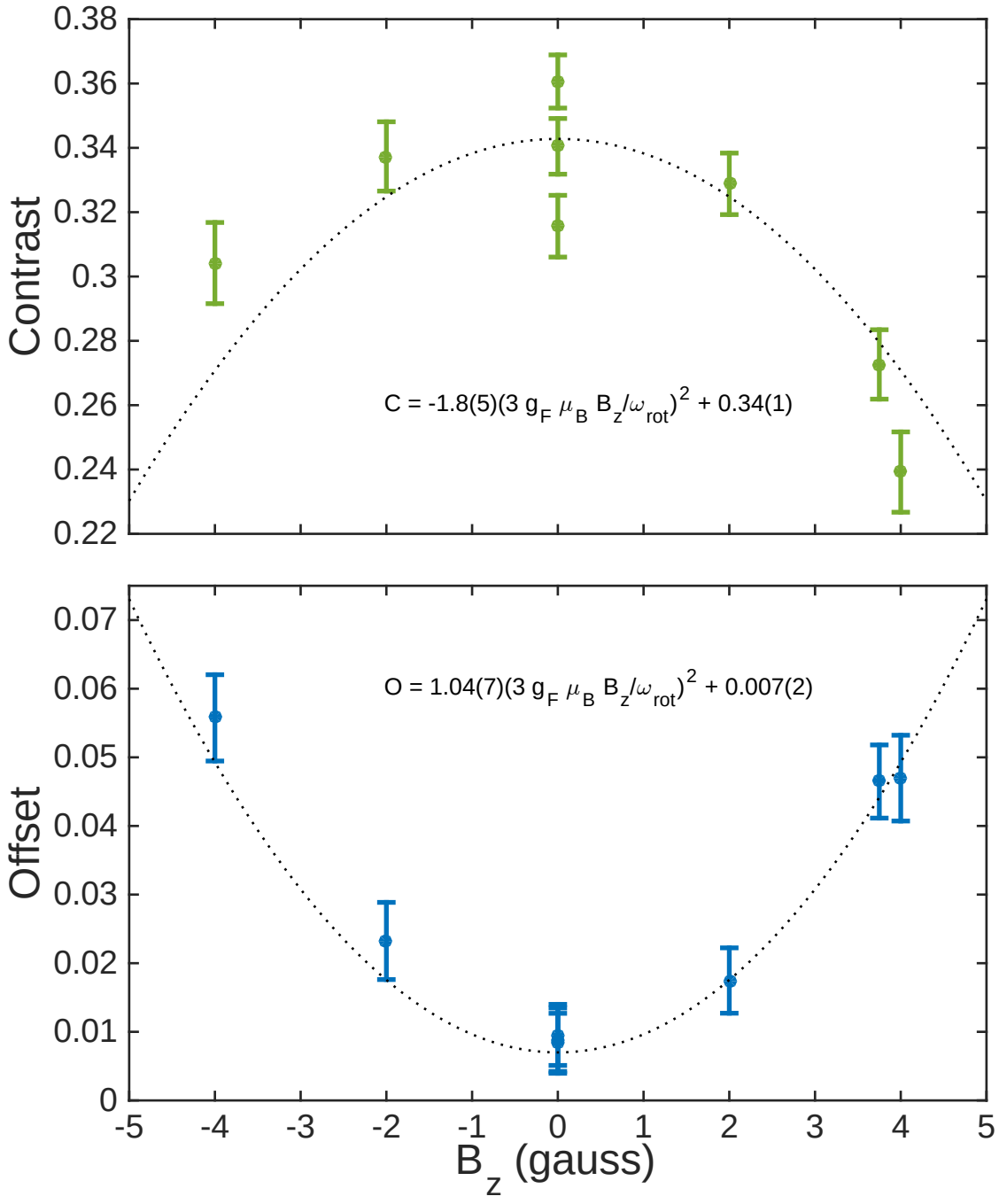

4.2.5 Fields inhomogeneities

Another potential source of systematic errors is spatial inhomogeneities in the electric and magnetic fields that the ions experience. As the ions traverse the trap, either by secular motion, radio-frequency micromotion, or rotational micromotion, the ions sample the inhomogeneities of the electric and magnetic fields and experience energy shifts. The magnetic field inhomogeneities can cause Zeeman shifts, and the electric field inhomogeneities can tip the molecule axis out of the plane of rotation and cause a berry's phase shift.

First we will consider inhomogeneities in the rotating electric field. The trap was designed with the application of a homogeneous rotating electric field in mind, so ideally the electric field will be $\mathcal{E}_{\text{rot}}(\hat{x}\cos(\omega_{rot}t) + \hat{y}\sin(\omega_{rot}t))$, but there will always be some degree of inhomogeneity. The trap is symmetric about the xy plane, and also the zx and zy plane, so first order gradients in the magnitude of $\mathcal{E}_{\text{rot}}$ should be heavily suppressed. However, we do anticiapte second order gradients due to the cylindical symmetry of the trap.

Electrostatic calculations done using COMSOL allow us to predict the inhomogeneity in $\mathcal{E}_{\text{rot}}$ for a perfectly constructed trap. If we write $\mathcal{E}_{\text{rot}}$ out with second order inhomogeneities,

$$\mathcal{E}_{\text{rot}}(x, y, z) = \mathcal{E}_{\text{rot}}\big(1 + \beta_x x^2 + \beta_y y^2 + \beta_z z^2\big), \tag{4.38}$$

then we predict roughly $\beta_x = -\beta_y = -0.0027\text{cm}^{-2}$, and $\beta_z = 0.001\text{cm}^{-2}$. Of course, the construction of the trap will never be exactly perfect, nor will the amplitude and phase of the voltage drive on each of the electrodes comprising the trap. We can characterize the inhomogeneity by measuring the shift in the ponderomotive potential when the rotating electric field is applied. In the absence of a rotating electric field, the secular motion in an ion trap is to lowest order harmonic. A rotating electric field with no inhomogeneity will not have any confining or deconfining influence on the ions because it has no gradient. A rotating electric field with a finite inhomogeneity will induce an additional ponderomotive potential, which can be observed by measuring the change in trap frequency. The change in trap frequency can be used to extract the inhomogeneity β. The

ponderomotive potential is

$$V_{\text{pon}} = \frac{1}{2} m\omega_{\text{pon}}^2 x_i^2 = \frac{e^2 \mathcal{E}_{\text{rot}}^2}{4m\omega_{rot}^2}. \tag{4.39}$$

We can match terms with x^2, y^2, and z^2 to solve for β,

$$\beta_i = 2\frac{m^2\omega_{rot}^2\omega_{i,pon}^2}{e^2\mathcal{E}_{\text{rot}}^2}. \tag{4.40}$$

The trap frequencies can be measured by giving a small kick to the ions and measuring the oscillation of the center of mass of the ion cloud in the trap. These frequencies can be measured with and without the rotating electric field. The difference of the squares of the frequencies of these two measurements yields the squared ponderomotive frequency. We applied a rotating electric field of 24 V/cm at $\omega_{\text{rot}} = (2\pi)250$ kHz and measured $\omega_{x,\text{pon}}^2 = -(2\pi)^2 1.75$ kHz^2, $\omega_{y,\text{pon}}^2 = (2\pi)^2 0.795$ kHz^2, and $\omega_{x,\text{pon}}^2 = (2\pi)^2 0.43$ kHz^2, which yields $\beta_x = -0.025\text{cm}^{-2}$, $\beta_y = 0.0114\text{cm}^{-2}$, and $\beta_z = 0.0061\text{cm}^{-2}$. This inhomogeneity has the potential to be a systematic error when coupled with displacement from the center of the trap. One potential way this can lead to a systematic frequency shift is by contributing to an oscillating Berry's phase that is not centered about zero. The angle α that the molecule makes with the xy plane is the same as the angle with the total electric field. Assuming the radial trapping fields are much smaller than the rotating electric field, then the angle α as a function of axial position z is

$$\alpha = \frac{\mathcal{E}_z(z)}{\mathcal{E}_{\text{rot}}(x,y,z)} = \frac{m\omega_z^2 z}{e\mathcal{E}_{\text{rot}}(1+\beta_z z^2)} \approx \frac{m\omega_z^2 z}{e\mathcal{E}_{\text{rot}}}(1-\beta_z z^2), \tag{4.41}$$

If we write z as having a constant offset z_0 and a sinusoidal oscillation at the trap frequency ω_z, then we find that the time average of α has a finite value,

$$\langle\alpha\rangle = \left\langle \frac{m\omega_z^2(z_0 + z_1\sin(\omega_z t))}{e\mathcal{E}_{\text{rot}}}(1-\beta_z(z_0+z_1\sin(\omega_z t))^2)\right\rangle = \frac{3m\omega_z^2 z_1^2}{2e\mathcal{E}_{\text{rot}}}\beta_z z_0 = \frac{3k_b T_z}{2e\mathcal{E}_{\text{rot}}}\beta_z z_0. \tag{4.42}$$

At the center of the trap the ions will oscillate in the axial direction, with the restoring force either pointing up or down, and similarly the axial electric field tipping the molecules up or down as well. Over the time of a period of axial oscillation the angle the molecules makes with the xy plane will average to zero. When an ion is offset from the center of the trap in the axial direction, this is

Figure 4.9: Spatial inhomogeneity in $\mathcal{E}_{\rm rot}$ and displacement from the center of the ion trap causes a Berry's frequency shift to appear in the f^{BR} frequency linear combination equal to $3\omega_{rot}\alpha$. The angle the molecules makes with the plane of rotation, $\alpha = \mathcal{E}_z/\mathcal{E}_{\rm rot}$, oscillates about a non-zero value. The frequency shift in fBR should increase linearly with z displacement, and also be proportional to $\omega_{rot}/\mathcal{E}_{\rm rot}$, see eq. (4.43). We plot f^{BR} against the scaled axis $3f_{rot}(k_B/\mathcal{E}_{\rm rot})z$ to collapse the four data sets onto a single line. This also allows us to extract a single fit value to compare to the inhomogeneity. This agrees well with the previously measured inhomogeneity, $\beta_z = 0.0061$, and an axial temperature of 15 Kelvin.

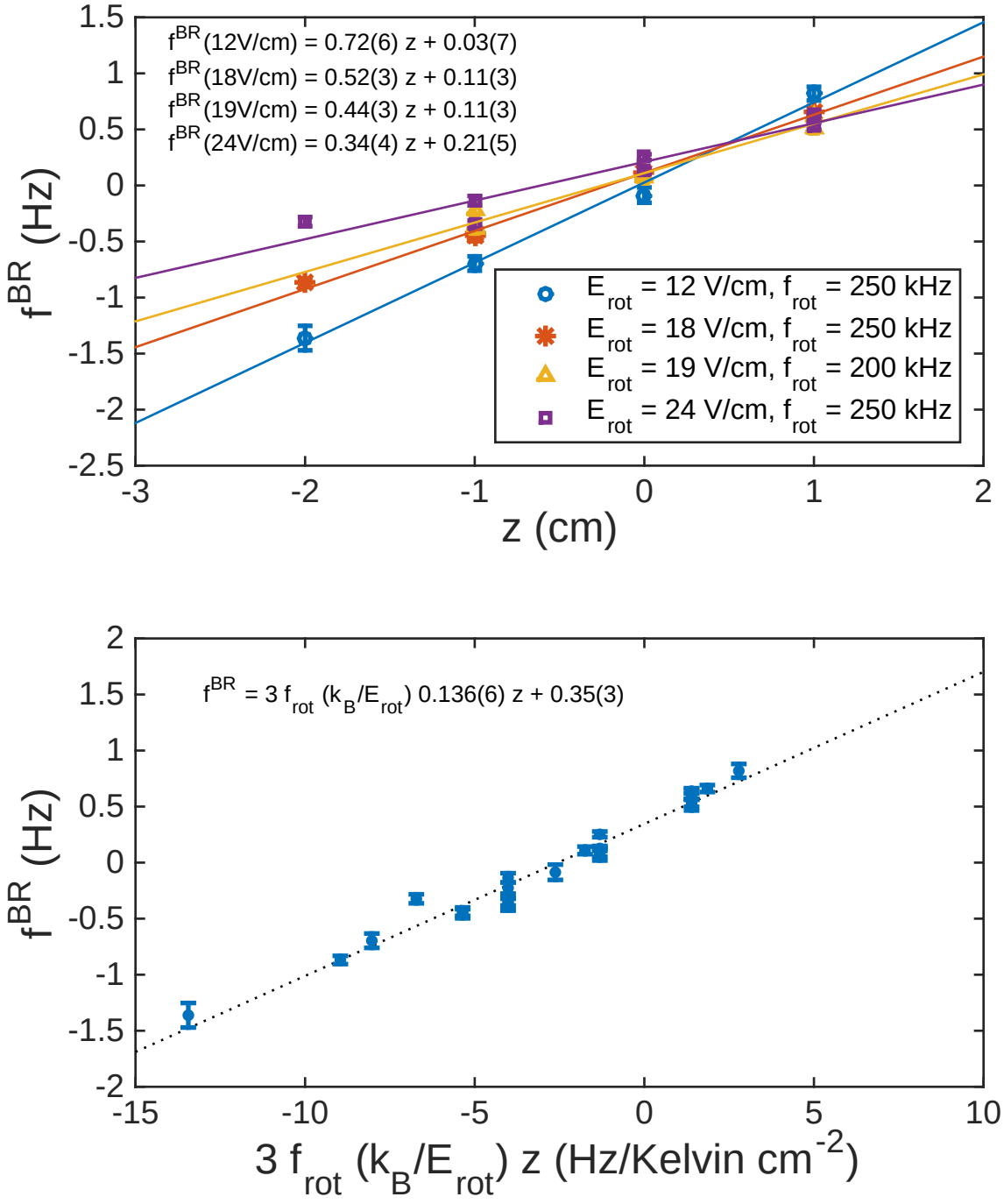

no longer the case. The rotating electric field is stronger the further the ion is from the center, so for the portion of the oscillation that the ion is furthest from the center, the angle α the molecule makes with the xy plane is smaller, and for the portion of the oscillation when the ion is closer to the center, the angle α is larger. Breaking the symmetry of $\mathcal{E}_{\rm rot}$ in the axial direction causes α to have a non-zero mean value. This leads to a Ramsey fringe frequency shift $3\alpha\omega_{\rm rot}$, which is odd under the switch of rotation direction because of the inclusion of $\omega_{\rm rot}$, and is also odd under the switch of rotating magnetic field direction. This means we expect to see this type of effect in the f^{BR} frequency linear combination,

$$f^{BR} = 3\omega_{rot}\frac{3k_bT_z}{2e\mathcal{E}_{\rm rot}}\beta_z z_0. \tag{4.43}$$

We expect to see this effect in f^{BR} as we scan the axial position z_0 in the trap. This effect should scale as $\omega_{\rm rot}/\mathcal{E}_{\rm rot}$. This is exactly what we observe in fig. 4.9. In this set of experiments we moved the ions over a range of 3 cm in the axial direction (the spacing between axial endcap electrodes is about 10cm). We see several Hz shifts in f^{BR}, and the slope of the effect scales like $\mathcal{E}_{\rm rot}^{-1}$. Plotting the observed effect in f^{BR} against an axis scaled by ω_{rot} and $\mathcal{E}_{\rm rot}$ we can fit the slope $0.136(6)\text{Kelvin/cm}^2 = (3/2)T_z\beta_z$. This agrees well with the measured inhomogeneity $\beta_z = 0.0061$ cm^{-2} and an axial temperature of $T_z = 15$ Kelvin.

Next we examine how such a Berry's frequency shift might affect the EDM channel, f^{BD}. We can combine higher order effects of terms with DR parity and BR parity to create potential terms with the correct BD parity to appear in the EDM channel, f^{BD}. An axial magnetic field has an understood effect on f^{DR}, described in eq. (4.34), which can couple to a non-reversing magnetic field that appears in f^{BR}. Additionally, the effect of $\alpha\omega_{\rm rot}$ can directly perturb the typical f^{BD} terms at a higher order in the series expansion, where an even power of ω_{rot} doesn't change sign under rotation switch. Thus there are two leading order terms for Berry's phase appearing in the EDM channel,

$$f'^{BD} = f^{BD} - \frac{\Delta\delta\Delta}{3g_F\mu_B\mathcal{B}_{\rm rot}}\left(\frac{3\alpha\omega_{rot}}{3g_F\mu_B\mathcal{B}_{\rm rot}}\right)\left(2\frac{3g_F\mu_B\mathcal{B}_z}{\omega_{rot}} - 3\frac{3\alpha\omega_{rot}}{3g_F\mu_B\mathcal{B}_{\rm rot}}\frac{\delta\mathcal{B}}{\mathcal{B}_{\rm rot}}\right). \tag{4.44}$$

Taking no care to control the z position of the ions in the trap, with the modest requirement of

nulling the axial components of Earth's field to 10%, and shimming $\delta\mathcal{B}$ to 10%, these effects are 50 μHz and 10 μHz for the axial magnetic field and α^2 correction respectively, which is a systematic of 10^{-29} $e\cdot$cm. Additionally, there will be a very obvious 2 Hz shift in the f^{BR} channel. We can either choose to correct for the effect in f^{BR} after the measurement, or servo the axial position of the ions to $z = 0$ in the trap. This can be done to better than 0.5 cm, in which case the systematic shift of f^{BD} is suppressed well below the 10^{-29} $e\cdot$cm level.

4.2.6 Unintentional gradients

We observed large frequency shifts in the non-reversing magnetic field channel f^B when we applied a magnetic field along the axial direction of the trap and then displaced the ion cloud along the same axis. This was troublesome, because there were various predicted effects of axial magnetic fields explored in section 4.2.4 and this was not one of them. Additionally, the non-reversing magnetic field channel is the one that appears most strongly in the EDM channel f^{BD}, where $\delta g/g_F$ is typically larger than 0.001, meaning that a 10 Hz shift in f^B, as observed in fig. 4.10 will be an EDM mimicking systematic to the tune of 10 mHz, or $1.7 \times 10^{-27} e$ cm. The resolution of this problem is a cautionary tale. We performed these experiments by quickly building a pair of quadrupole coils in a Helmholtz configuration around the ion trap vacuum chamber and applying current to them. What is plotted in fig. 4.10 is the effect we observed in f^B against the inferred $\mathcal{B}_z$. We are implicitly assuming that the magnetic field the coils are applying is uniform, an assumption that turns out to be completely invalid. If we consider a magnetic field that has a second order gradient $\mathcal{B}_z(z) = \mathcal{B}_z(1 + \beta z^2)$, then in addition to applying a zero order magnetic field $\mathcal{B}_z$ we are also adding a strong magnetic field gradient with a position dependence, $\delta_z\mathcal{B}_z(z) = \mathcal{B}_z 2\beta z$. Satisfying Maxwell's equations requires there also be a radial gradient $\boldsymbol{\nabla}\mathcal{B} = \mathcal{B}_z\beta z$. This is exactly a non-reversing magnetic field gradient. We therefore expect to see an effect in f^B that is

$$f'^B = f^B + 3g_F\mu_B\mathcal{B}_z\beta z\frac{e\mathcal{E}_{\text{rot}}}{m\omega_{rot}^2}. \tag{4.45}$$

To substantiate this theory we moved one of the coils we used to apply $\mathcal{B}_z$, reasoning that

Figure 4.10: We observed a large systematic shift in f^B when we applied a magnetic field in the axial direction and also displaced the ion cloud axially in the trap. This is due to an accidentally applied gradient that is proportional to the intentionally applied $\mathcal{B}_z$. This is confirmed by moving the magnetic field coils such that a different unintentional gradient would be applied, and seeing that the effect in f^B changes. Additionally we can see the effect of poor reversals of rotation direction, where $\mathcal{E}_{\text{rot}}$ has a different magnitude and inhomogeneity for the different rotation directions. This can be observed in f^{BR} when the $\mathcal{E}^R_{\text{rot}}$ shim changed.

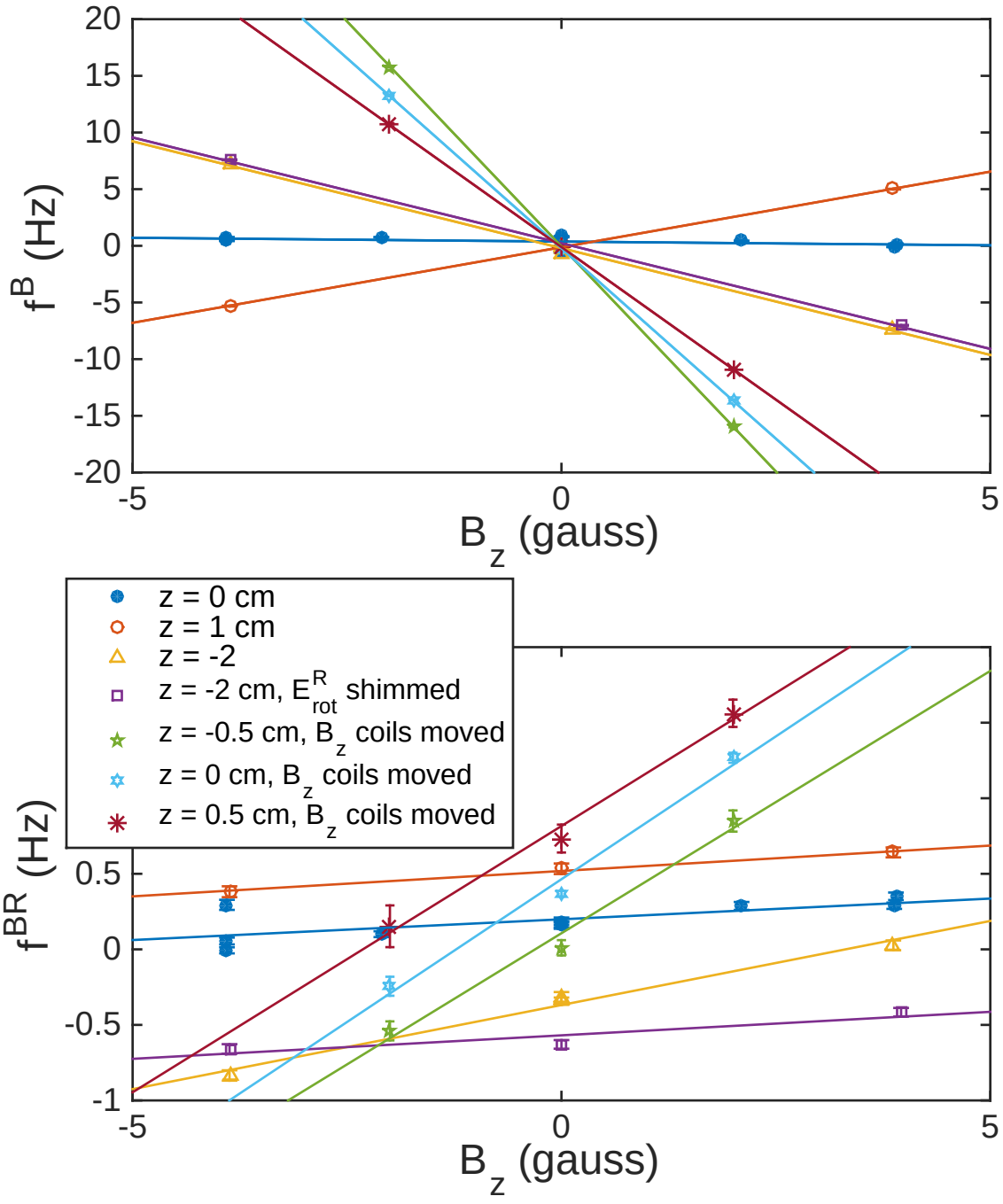

we could decrease the uniformity of the applied field and increased the size of the second order gradient β. The three sets of data in fig. 4.10 after the coils had been moved bear proof to this theory. After the coils were shifted the second order gradient increased, and the effect in f^B was greatly enhanced. The fix for this is relatively simple, to remove the coils. They were not used in the experiment except to apply axial magnetic fields and then to see what would happen. The coils were never designed to be particularly uniform, in fact they were taken from a decommissioned MOT and essentially draped over the vacuum chamber in an attempt to quickly begin the study of lab frame magnetic fields. We have replaced these coils with a new pair of coils specifically designed to be uniform, and when we installed these new coils we inserted a magnetic field probe into the center of the ion trap to characterize the applied field and any incidental gradients. The new coils have an incidental gradient of < 1 mGauss/cm when used to apply a uniform field of 2.6 Gauss.

4.3 Measured systematics

In addition to the effects that we can measure and characterize, there are additional systematic shifts that we have observed that still elude our understanding. In this section we describe those effects whose mechanisms are still unknown to us. We have attempted to study these effects by measuring how they scale with various experimental parameters, and we will catalogue these experimental relations and summarize our understanding.

Both effects arise from the application of a static lab frame magnetic field, $\mathcal{B}_{\text{lab}}$, in concert with **radial** displacement of the ion cloud from the nominal center of the trap. When we first applied a magnetic field in the xy plane of the experiment, we expected no effect, or perhaps a small effect from a previously neglected geometric phase term. Instead we observed a several Hz shift in f^B, the non-reversing magnetic field frequency combination, and paradoxically, an even larger shift in f^{BR}, the "Berry's phase" channel. The larger shift in f^{BR} was surprising because we expected that frequency shifts in f^B would be suppressed by the change in rotation direction. We determined that these shifts were linearly correlated with both the magnitude of the magnetic field but also the displacement from the center of the ion trap. Additionally we observe f^B only

for displacement parallel to the applied $\mathcal{B}_{\text{lab}}$, and f^{BR} only for displacement perpendicular to the to applied $\mathcal{B}_{\text{lab}}$, as depicted in fig. 4.11. For this reason we colloquially label the effect that appears in f^{B} as "$\vec{\mathcal{B}} \cdot \vec{r}$" and the effect that appears in f^{BR} as "$\left(\vec{\mathcal{B}} \times \vec{r}\right) \cdot \vec{\omega}_{rot}$". Both of these effects are linear with displacement from the center of the trap. This is already an important clue, because there are a limited number of ways that the ions can even know where the center of the trap is. They are:

- $\boldsymbol{\nabla}\mathcal{B}$

  The rotating magnetic field is applied via the combined effect of a static lab gradiant, $\boldsymbol{\nabla}\mathcal{B}$, and the circular micromotion of the ions driven by the rotating electric field. The quadrupole gradient is designed such that the magnetic field minimum should roughly coincide with the center of the ion trap. The biggest argument against this being the cause of the observed effects is that we change the size of $\boldsymbol{\nabla}\mathcal{B}$ we do not see any change in the size of the effect in f^{B} or f^{BR}, as in fig. 4.12 and fig. 4.14.

- Trap rf micromotion

  The ion trap is a radio-frequency Paul trap that uses a time varying quadrupole electric field to trap the ions. As the ions move away from the center of the ion trap they experience more rf micromotion, creating a ponderomotive restoring force pushing them back to the center of the trap. We displace the ion cloud by applying additional dipolar patch charges to the trap electrodes, and as they are displaced their rf micromotion increases. The argument against this rf micromotion related to the observed effect is that for an increase in the amplitude of the rf drive, as in fig. 4.12 and fig. 4.14, we expect an increase in micromotion amplitude, but do not observe a change in the effects in f^{B} and f^{BR} when we change the amplitude of the rf drive, V_{rot}.

- Accidental gradients in $\mathcal{B}_{\text{lab}}$

  We apply $\mathcal{B}_{\text{lab}}$ by using two pairs of coils each in Helmholtz configuration to null Earth's

Figure 4.11: Here we have nulled Earth's ambient magnetic field and applied an additional magnetic field aligned with the $\hat{y}$ trap axis with magnitude 2.5 Gauss. We then performed two experiments, one experiment where the ion cloud's displacement in the $\hat{y}$ direction of the trap was nominally zero and we scanned the $\hat{x}$ position of the ion cloud, the second experiment where the $\hat{x}$ direction of the trap was nominally zero and we scanned the $\hat{y}$ position of the trap several mm. The two ion detectors used are microchannel plates on opposite sides of the trap, parallel to the $\hat{x}$ axis. One detector is a time of flight detector, and the arrival time of the ions corresponds to their position along the $\hat{x}$ vector of the trap. The other detector is a imaging detector, which gives the position of the ion cloud along the $\hat{y}$ vector of the trap. We see that the f^B is only affected by displacements of the ions parallel to the magnetic field, and f^{BR} is only affected by displacements of the ions perpendicular to the magnetic field.

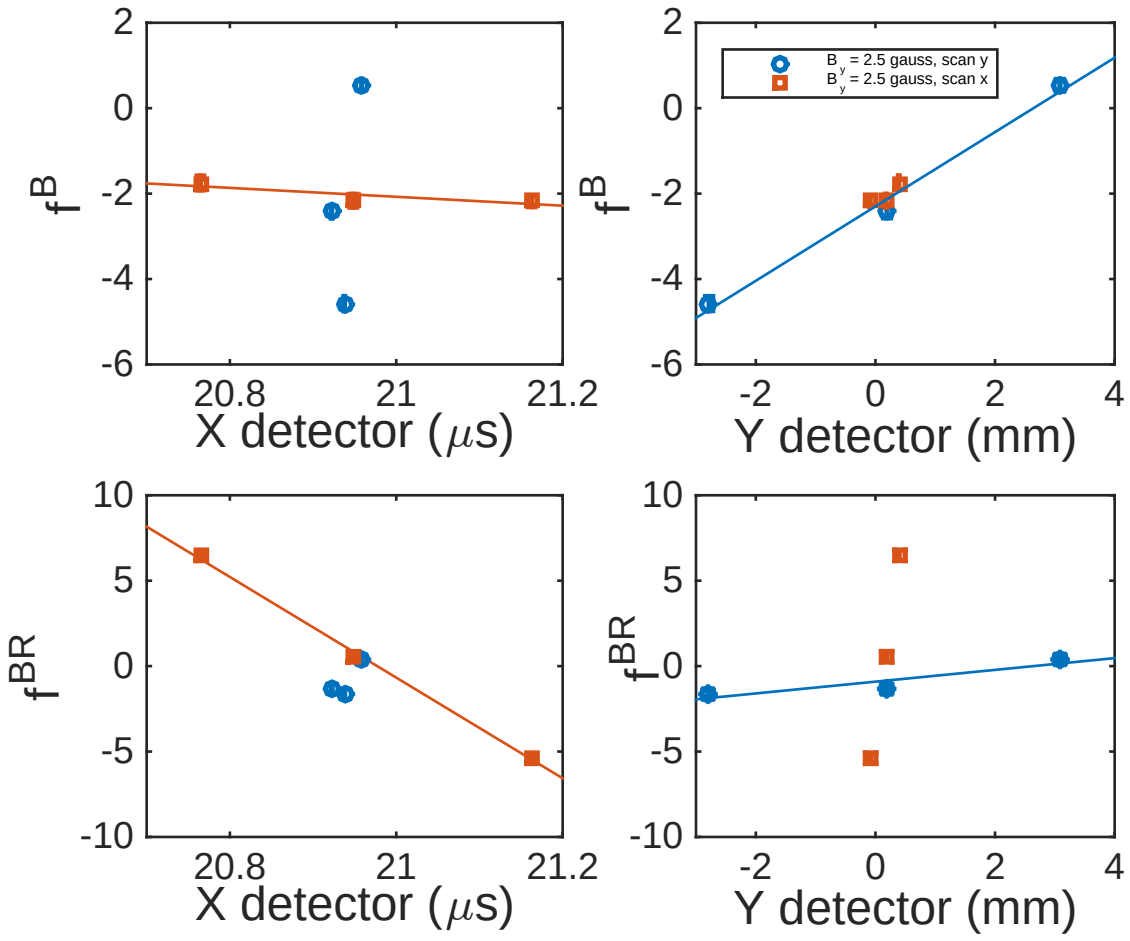

field and then apply fields that align with either the trap $\hat{x}$ or $\hat{y}$ axis. Neither coil axis is aligned with a trap axis. If in addition to a static magnetic field we are also applying a static gradient, as we displace the ions we could be sampling the effect of this gradient. The problem with this theory is that the effects can be observed in the ambient magnetic field, and the effects go away when the ambient magnetic field is actively cancelled with the two pairs of coils. It is highly unlikely that the ambient lab gradients are also identically cancelled by any accidental gradients applied by the magnetic field coils.

- $\mathcal{E}_{\text{rot}}$ inhomogeneity

  As we have seen in previous sections, inhomogeneities in $\mathcal{E}_{\text{rot}}$ can be the source of other systematic effects, in particular those arising due to a Berry's phase in the f^{BR} frequency linear combination. The rotating electric field $\mathcal{E}_{\text{rot}}$ was designed to be most homogeneous at the center of the trap, so it is not unreasonable that as the ion cloud is displaced from the center that some effect due to the inhomogeneity of $\mathcal{E}_{\text{rot}}$ will enter play. Guided by this we will examine how both of these effects scale with $\mathcal{E}_{\text{rot}}$ in the following sections.

4.3.1 $f^B \sim \vec{\mathcal{B}} \cdot \vec{r}$

Informed by our suspicions established in the previous section, we examined the dependence of this effect on f^B as a function of ion trap rf quadrupole drive, see fig. 4.12. The drive is varied by 50% and there is no strong change in the relation between f^B and displacement. This could indicate that rf micromotion has nothing to do with this effect. There are a couple of problems with this sort of experiment. The first is that we have done measurements like this twice and found different results. Earlier tests where we varied the strength of the rf drive found that there was a dependence of f^B on the strength of the drive. The difference between the older experiments and the experiments presented in fig. 4.12 is how the ion position was shifted. In the previous experiments to displace the ion cloud a dipolar patch potential was applied to the trap electrodes calculated to displace the cloud by a certain amount for a given secular trap frequency. For the more

Figure 4.12: Here we examine how the $f^B \sim \vec{B}\cdot\vec{r}$ effect scales with various experimental parameters. We apply various magnetic fields aligned with the $\hat{y}$ axis of the ion trap and then displace the ions along that direction. We see confirmation of the linear scaling in both $\mathcal{B}_y$ and y, as well as a lack of dependence on displacements in z. Additionally we see that the effect increases with increased ω_{rot} and decreases with increased $\mathcal{E}_{\text{rot}}$ (more data will be needed to establish the exact scaling). We also see a lack of dependence on $\boldsymbol{\nabla}\mathcal{B}$ or f^0. We have changed the magnetic field gradient and the Ramsey fringe frequency by a factor of 4 with no effect. Additionally there is no large effect with a change in the ion trap rf quadrupole drive, V_{rf}.

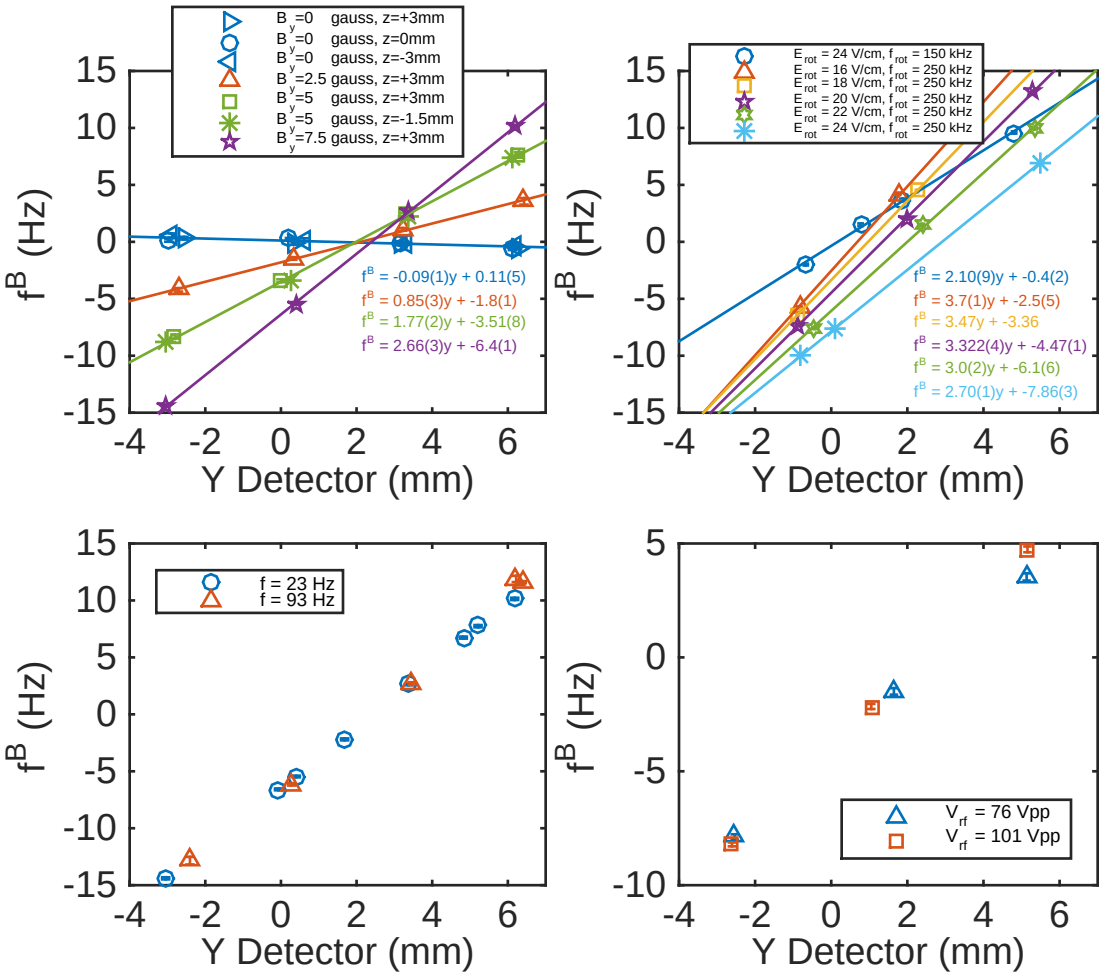

recent batch of experiments a dipolar patch correction is iteratively applied to the trap electrodes until the ion cloud center of mass converges to a desired position on the ion detector. We find this method to be more robust to changes in quadrupole drive, which will change the secular trap frequency, although there is still a secular frequency dependent transfer function that translates the detector ion position to trap ion position, which leaves open the potential to misinterpret the ion cloud position.

There is no dependence of f^B on either the Ramsey fringe frequency f^0 or lab frame magnetic field gradient. There are several important consequences of this measurement. The first is that is rules out the intentionally applied magnetic field gradient $\boldsymbol{\nabla}\mathcal{B}$ from being the "ruler" by which the ion cloud determines its displacement from the center of the trap. Secondly, because we were able to vary the frequency by a factor of 4, it shows that the effect on f^B must have a very direct, up front mechanism. In contrast to the effect of axial magnetic field on f^R, or the effect of electric field on differential rotational coupling $\delta\Delta$ on f^{BD}, where terms appear in a perturbation series expanded in terms of $(f^0)^{-n}$, these effects have no f^0 dependence. The inference we draw from this is that whatever the mechanism, it must affect the energy levels of the $m_F = \pm 3/2$ levels, and not the perturbative coupling between them. Potential types of mechanisms that directly affect these levels are things like the Zeeman interaction or a Berry's phase that doesn't average to zero.

We also note the scaling of f^B with ω_{rot} and $\mathcal{E}_{\text{rot}}$. More data is currently being taken on these scalings, but the trend established so far is that f^B increases with increasing ω_{rot} and decreasing $\mathcal{E}_{\text{rot}}$. This is evocative of a Berry's phase type of effect, where the frequency shift is proportional $\omega_{rot}\alpha$, where α is the angle the molecule makes with the xy plane. This angle is defined by the electric field pointing direction, which in the small angle approximation is $\mathcal{E}_z/\mathcal{E}_{\text{rot}}$. What is unclear is how to ensure that the effect is even under switching rotation directions if there is a dependence on an odd power of ω_{rot}. Presumably the dependence on ω_{rot} must be even, or some other factor must be included that is also odd under switching rotation direction.

The size of this effect is about 3.5 Hz/(Gauss cm) at $\mathcal{E}_{\text{rot}} = 24$ V/cm and $\omega_{rot} = (2\pi)250$ kHz. Using dimensional analysis we can write possible terms that have the right dependence on $\mathcal{B}$

and r and see what size frequency they predict. A term that has approximately the correct scaling could be something like

$$f^B \overset{?}{\sim} 3g_F\mu_B\vec{B}\cdot\vec{r}\frac{m\omega_{rot}^2}{e\mathcal{E}_{\rm rot}}, \tag{4.46}$$

however this effect is about a factor of 10^5 too large. We would need another dimensionless factor that doesn't depend on Ramsey fringe frequency, rf drive amplitude, or have the wrong dependence on $\mathcal{E}_{\rm rot}$ or ω_{rot}. Another possible guess for an effect inspired by previously discussed Berry's phase effects could be

$$f^B \overset{?}{\sim} 3\omega_{rot}\frac{\left(\vec{\mathcal{B}}\cdot\vec{r}\right)\omega_{rot}}{\mathcal{E}_{\rm rot}}. \tag{4.47}$$

This term alone is a factor of about 20 larger than the observed effect in f^B. It looks like a Berry's phase where the angle α of the molecule is defined by $\mathcal{E}_z/\mathcal{E}_{\rm rot}$, where $\mathcal{E}_z \approx (\vec{B}\cdot\vec{r})\omega_{rot}$. This has the appearance of a Lorenz force, where $r\omega_{rot}$ is a velocity. Beyond that we can say no more about this effect, other than that complex numerical simulations that include both the external degrees of freedom of the ions in realistic trapping electric fields and electric and magnetic bias fields, and also including internal states comprising the entire ${}^3\Delta_1, J = 1$ rovibronic manifold of states, does not find any sort of significant motional effect of the ions that contributes to f^B in this way.

Failing to find an understanding of the mechanism behind this effect, the next best thing we can do is place an upper limit on how much this effect will appear as a systematic in the EDM channel, f^{BD}. We know that effects in f^B that are due to a Zeeman type interaction appear in f^{BD} suppresed by $\delta g_{\rm eff}/g_F$, and that other effects in f^B, such as Berry's phase, appear in f^{BD} suppressed by a slightly different $\delta g_{\rm eff}/g_F$ that includes the contribution from the differential rotational coupling $\delta\Delta$ but not the differential g-factor $\delta g/g_F$. We can place an upper bound on the effect of f^B in the EDM channel f^{BD} by operating at large $\mathcal{B}_{\rm lab}$ and large displacement to enchance f^B as much as possible. We can shift f^B by as much as 30 Hz peak to peak. This large of an effect is sure to be seen in f^{BD}, especially for smaller $\mathcal{E}_{\rm rot}$ where the effective $\delta g_{\rm eff}/g_F$ is larger. There is a correction developed in section 5.2 that we can use to remove the expected contribution from f^{BD} due to f^B in a self consistent way. We can apply this correction to f^{BD} and look for

Figure 4.13: Here we take data with large trap displacements of ±5mm, and parallel lab frame magnetic fields of up to 7.5 Gauss to observe a frequency shift in the non-reversing magnetic field channel of up to 30 Hz. Using the self consistent correction developed in section 5.1.4, we subtract the expected contribution of f^B from the EDM channel f^{BD} and look for any residual trend. The fit to this residual trend can be used as an upper bound on the systematic effect of the anomalous f^B due to "$\vec{B} \cdot \vec{r}$".

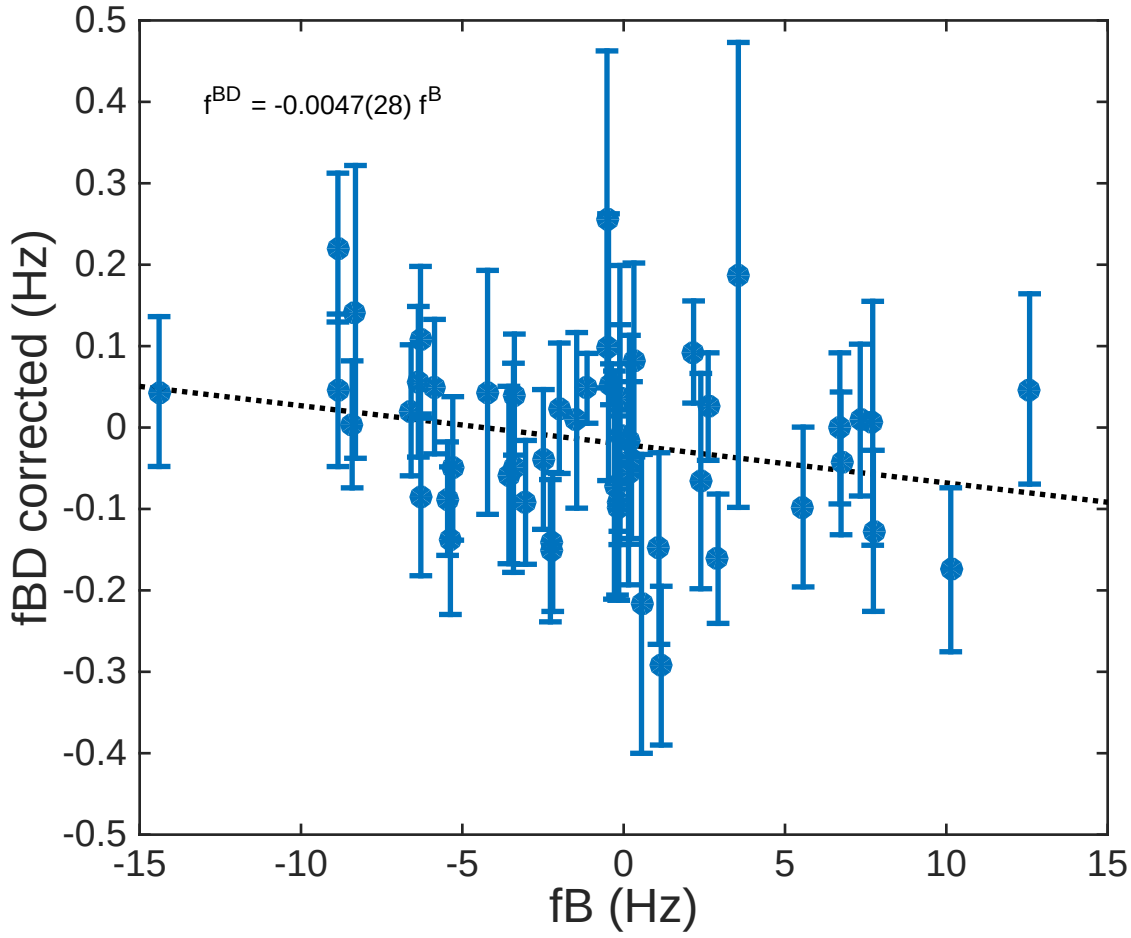

any remaining residual correlation with f^B. We find that $f^{BD} = -0.0047(28)f^B$, which has a 1.6σ significance in its difference from zero. If we can cancel out the ambient lab frame magnetic field to the 10% level to ~ 0.05 Gauss, and control the ion cloud center of mass position to 0.05 cm, then we should be able to keep f^B below 10 mHz. The systematic effect on the EDM channel f^{BD} will be $-47(28)\mu$Hz, or $8.3 \pm 5 \times 10^{-30} e$ cm.

4.3.2 $f^{BR} \sim (\vec{\mathcal{B}} \times \vec{r}) \cdot \vec{\omega}$

Similar to the anomalous f^B effect there is no dependence of f^{BR} on rf quadrupole drive, as seen in fig. 4.14. This is strong evidence that this effect cannot be due to inhomogeneity in the trapping fields or be related to rf micromotion. Likewise there is no dependence on $\boldsymbol{\nabla}\mathcal{B}$ or the Ramsey fringe frequency f^0. This indicates the effect isn't due to the displacement of the ions from the center of the magnetic quadrupole gradient. This also implies that $(\vec{\mathcal{B}} \times \vec{r}) \cdot \vec{\omega_{\text{rot}}}$ is a direct effect, similar to the anomalous effect in f^B. We do see that the f^{BR} effect has a dependence on $\mathcal{E}_{\text{rot}}$ and ω_{rot}, which points to some interaction with the spatial inhomogeneity of $\mathcal{E}_{\text{rot}}$. The dependence is roughly linear in each, $f^{BR} \propto \omega_{\text{rot}}\mathcal{E}_{\text{rot}}$. In total the unknown effect in f^{BR} can be summarized as

$$f^{BR} \propto \left(\vec{\mathcal{B}} \times \vec{r}\right) \cdot \vec{\omega}_{\text{rot}}\mathcal{E}_{\text{rot}}. \tag{4.48}$$

This term $\left(\vec{\mathcal{B}} \times \vec{r}\right) \cdot \vec{\omega}_{\text{rot}}\mathcal{E}_{\text{rot}}$ has units of electric field squared. There has to be another field or fields to compare this to in order to get something with units of frequency. These comparison fields cannot be $\mathcal{E}_{\text{rot}}$ or $\mathcal{E}_{\text{trap}}$ because this would change the nature of the dependence on $\mathcal{E}_{\text{rot}}$ and because it's already been established that there is no dependence on the trapping electric fields. It can't be the field from $\boldsymbol{\nabla}\mathcal{B}$ because this has also been ruled out of the f^{BR} dependence. Other possibilities are that the dependence of f^{BR} on ω_{rot} and $\mathcal{E}_{\text{rot}}$ is not truly linear, in which case this should be reexamined more carefully. Possible types of effects that increase with increasing ω_{rot} are effects arising from the Berry's phase. Quantities that increase with $\mathcal{E}_{\text{rot}}$ are the circular micromotion radius $r_{\text{rot}} \sim \mathcal{E}_{\text{rot}}/\omega_{\text{rot}}^2$ and the micromotion velocity $v_{\text{rot}} \sim \mathcal{E}_{\text{rot}}/\omega_{\text{rot}}$. Both of these have the wrong dependence on ω_{rot}, which could possibly be explained by an additional dependence on higher

powers of ω_{rot}. As in the previous section, without any concrete understanding of the mechanism behind this effect the best we can achieve is to place bounds on the size of any systematic that might appear in the EDM channel f^{BD}. For typical experimental parameters this effect is $f^{BR} \sim 8.9(1)$ Hz/(cm Gauss). If we can shim Earth's magnetic field to 0.05 Gauss and reproducibly place the ions to within 0.05 cm of the trap center then f^{BR} can be kept below 20 mHz. We can exaggerate the anomalous $f^{BR} \sim (\vec{\mathcal{B}} \times \vec{r}) \cdot \vec{\omega}$ effect by displacing the ion cloud several mm from the center of the trap and applying a large perpendicular magnetic field. Inevitably when we do this we will also apply an incidental parallel magnetic field component. We can subtract out the f^{B} effect due to this incidental parallel magnetic field component as best we can by applying the correction in section 5.1.4. Fitting the residual effect we find $f^{BD} = -0.0018(11) f^{BR}$. Dependent on successfully controlling the anomalous f^{BR} to 20 mHz we can place an upper bound on the residual effect on the EDM channel to be $-36(22)$ μHz, or $3 \pm 2 \times 10^{-30}$ $e\cdot$cm. Even making no attempt to shim Earth's field or place the ions in the center of the trap yields a residual systematic in f^{BD} of $1.6 \pm 9 \times 10^{-28}$ $e\cdot$cm.

4.3.3 $f^{BR} \sim zr^2$

We also observe a quadratic effect in f^{BR} with respect to displacements in the trap radial direction, as shown in fig. 4.16. Such an effect could potentially be attributed to $\mathcal{E}_{\text{rot}}$ inhomogeneity. The effect on the time independent portion of Berry's phase due to $\mathcal{E}_{\text{rot}}$ inhomogeneity is

$$\alpha = \frac{\mathcal{E}_z(z)}{\mathcal{E}_{\text{rot}}(x,y,z)} = \frac{m\omega_z^2 z}{e\mathcal{E}_{\text{rot}}(1+\beta_y y^2+\beta_z z^2)} \approx \frac{m\omega_z^2 z}{e\mathcal{E}_{\text{rot}}}(1-\beta_y y^2-\beta_z z^2-2\beta_y\beta_z y^2 z^2), \tag{4.49}$$

$$\langle\alpha\rangle = \frac{3m\omega_z^2 z_1^2}{2e\mathcal{E}_{\text{rot}}}\beta_z z_0(1-2\beta_y y^2) = \frac{3k_b T_z}{2e\mathcal{E}_{\text{rot}}}\beta_z z_0(1-2\beta_y y^2). \tag{4.50}$$

Here we have chosen to consider displacements y along the $\hat{y}$ direction instead of the more general displacements along a ray in the xy plane. We see that similar to the eq. (4.42) there is an α that doesn't time average to zero due to $\mathcal{E}_{\text{rot}}$ inhomogeneity that scales likes zy^2. This effect will appear in the channel f^{BR} as

$$f^{BR} = 3\omega_{rot}\frac{3k_b T_z}{2e\mathcal{E}_{\text{rot}}}\beta_z z_0(1-2\beta_y y^2). \tag{4.51}$$

Figure 4.14: This figure summarizes various experiments done to establish how $f^B \sim (\vec{B} \times \vec{r}) \cdot \vec{\omega}_{rot}$ scales with various experimental parameters. We apply magnetic fields along the $\hat{x}$ direction of the trap axis, and apply dipolar potentials to the trap electrodes to displace the ion cloud in the $\hat{y}$ direction. We see that the effect is linear in box $\mathcal{B}_x$ and in y. Additionally we see that the effect on f^{BR} increases with increasing $\mathcal{E}_{\text{rot}}$ and ω_{rot}. Finally, similar to the anomalous effect in f^B, there is no observed dependence of f^{BR} on magnetic field gradient $\boldsymbol{\nabla}\mathcal{B}$, Ramsey fringe frequency f^0, or rf quadrupole drive V_{rf}.

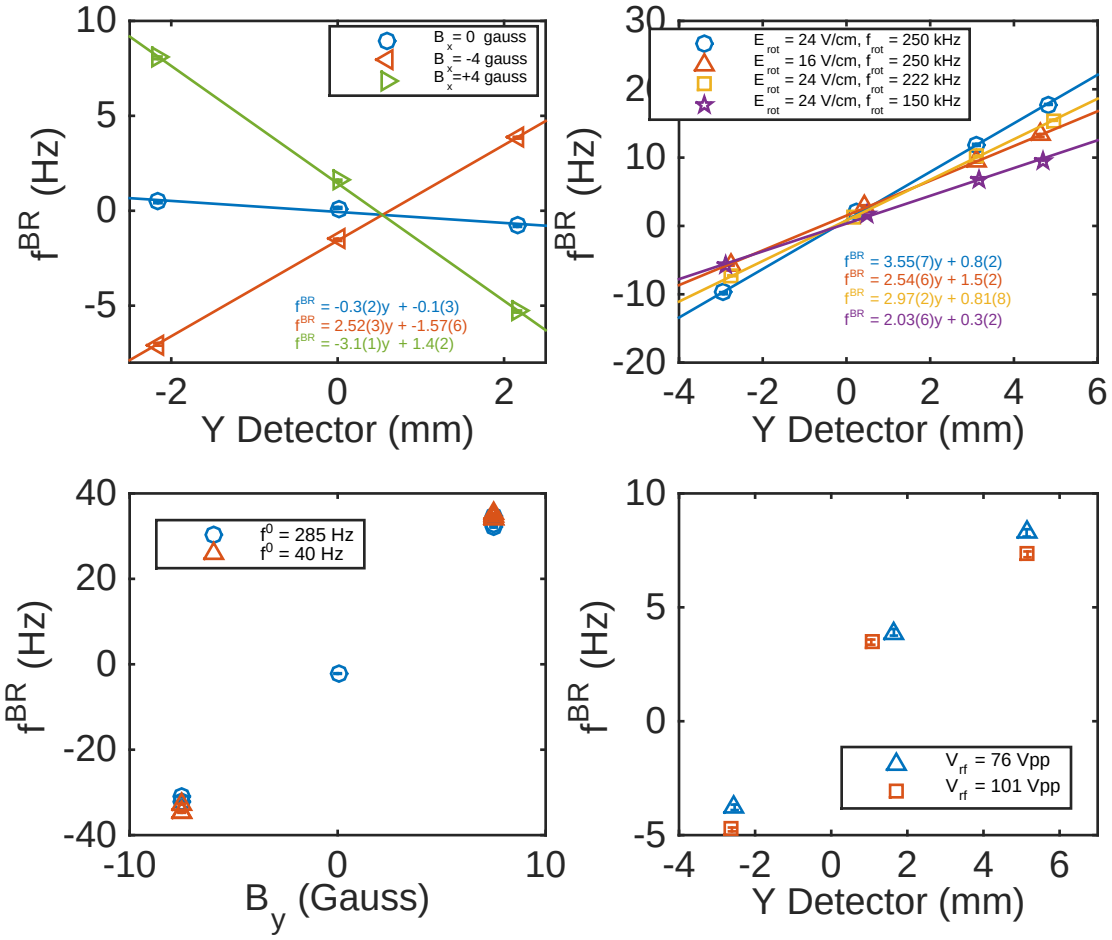

Figure 4.15: Here we take data with trap displacements of several mm, and perpendicular lab frame magnetic fields of ±7.5 Gauss to observe a frequency shift in the f^{BR} channel of up to 60 Hz. We can use the self consistent correction developed in section 5.1.4 to subtract the expected contribution of any f^{B} that might arise due to accidentally applied parallel lab frame magnetic fields and the "$\vec{\mathcal{B}} \cdot \vec{r}$" from the EDM channel f^{BD}. We then take the remaining effect and fit any residual trend. This can be used as an upper bound on the systematic effect of the anomalous f^{BR} due to "$(\vec{B} \times \vec{r}) \cdot \vec{\omega_{\text{rot}}}$".

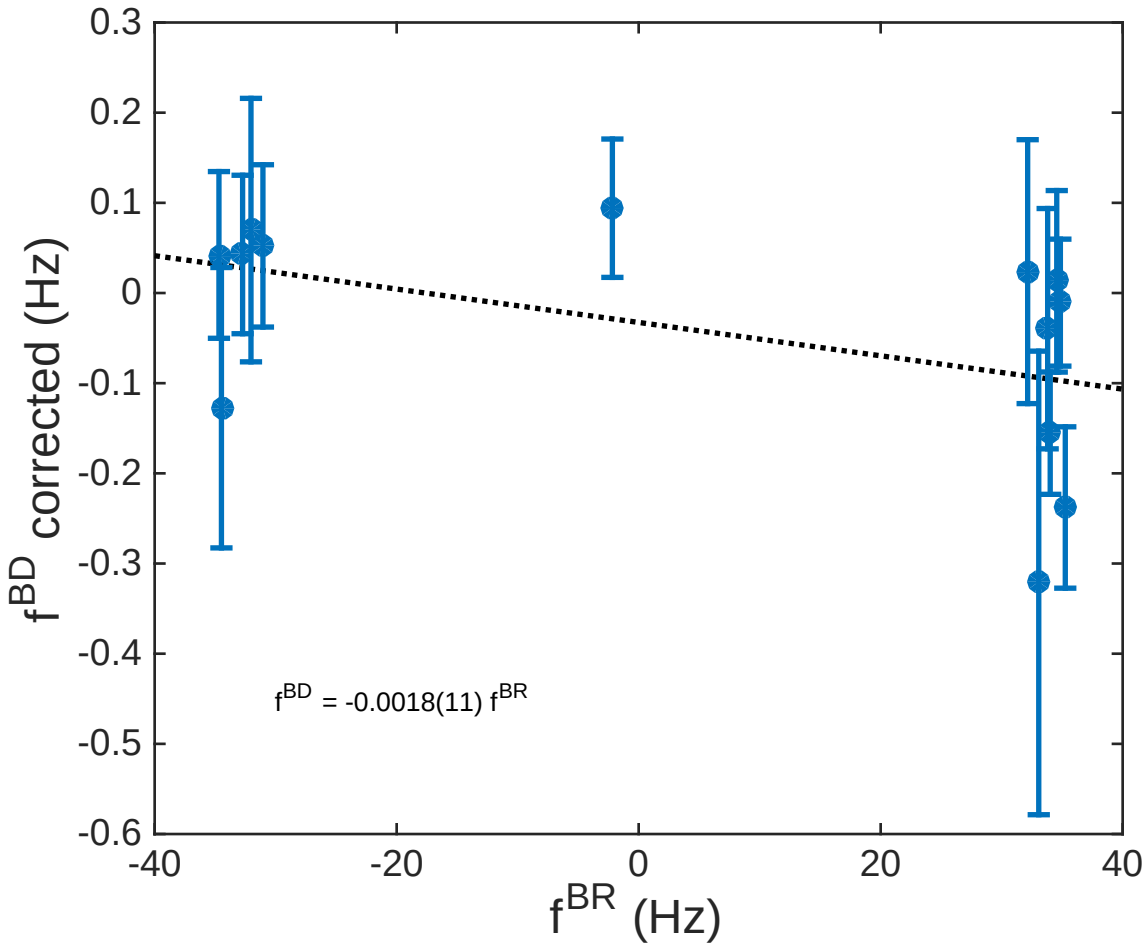

We have already determined $(3/2)T_z\beta_z = 0.136(4)$ Kelvin/cm^2. Plugging this into eq. (4.51) and equating this with the measured constant of proportionality from fig. 4.10,

$$f^{BR} \propto -0.022(1)(z/\text{cm})(y/\text{mm})^2\text{Hz}, \tag{4.52}$$

we find that $\beta_y \approx 30\text{cm}^{-2}$. This is extremely large compared to the measured $\beta_x = -0.025\text{cm}^{-2}$ and $\beta_y = 0.0114\text{cm}^{-2}$.

4.4 Potential other systematics

In addition to the systematics discussed in the previous sections there are a number of other potential sources for systematic errors. We haven't yet thoroughly investigated many of these effects, but we will list them below with a brief description and estimation their size.

- Detuning the $\pi/2$ pulses could potentially lead to a systematic effect in the doublet switch. The differential rotation-induced mixing $\delta\Delta$ requires that the timing of the $\pi/2$ pulses be different for each doublet. The $\pi/2$ pulse timings will inevitably be imperfect, and they will undoubtedly not be equally imperfect between the two doublets, which will lead to a ϕ^D term. We empirically see that we do as well as a $\phi^D = 0.0082(8)$, measured in fractions of a period. If we did not measure Ramsey fringes at short time to determine initial phase shifts, this could contribute to a 16 mHz frequency shift to the Ramsey fringe at 500 ms. With any frequency shift that is odd in B this can lead to a systematic in the EDM channel. However, we already see that $\delta\Delta$ leads to a f^D of several hundred mHz, so this effect will be an order of magnitude smaller.

- The ion trap electrodes have finite capacitance, which means that as we apply time dependent voltages to generate the rotating electric field we will incidentally also be applying time dependent currents. These currents can have the effect at the center of the ion trap of a rotating magnetic field that has the same rotation frequency and phase as $\mathcal{E}_{\text{rot}}$. This rotating magnetic field created by electrode currents will be odd under the rotation direction

Figure 4.16: We observe a quadratic shift in the f^{BR} channel as we displace the ions radially from the center of the ion trap. The amplitude of the quadratic term appears to be linearly proportional to displacement from the center of the ion trap in the axial direction, even changing sign as we move through the trap center. We anticipate an effect of this nature due to the trap electric field and $\mathcal{E}_{\mathrm{rot}}$ inhomogeneity, but this effect is larger than that of our predictions based on other inhomogeneity measurements.

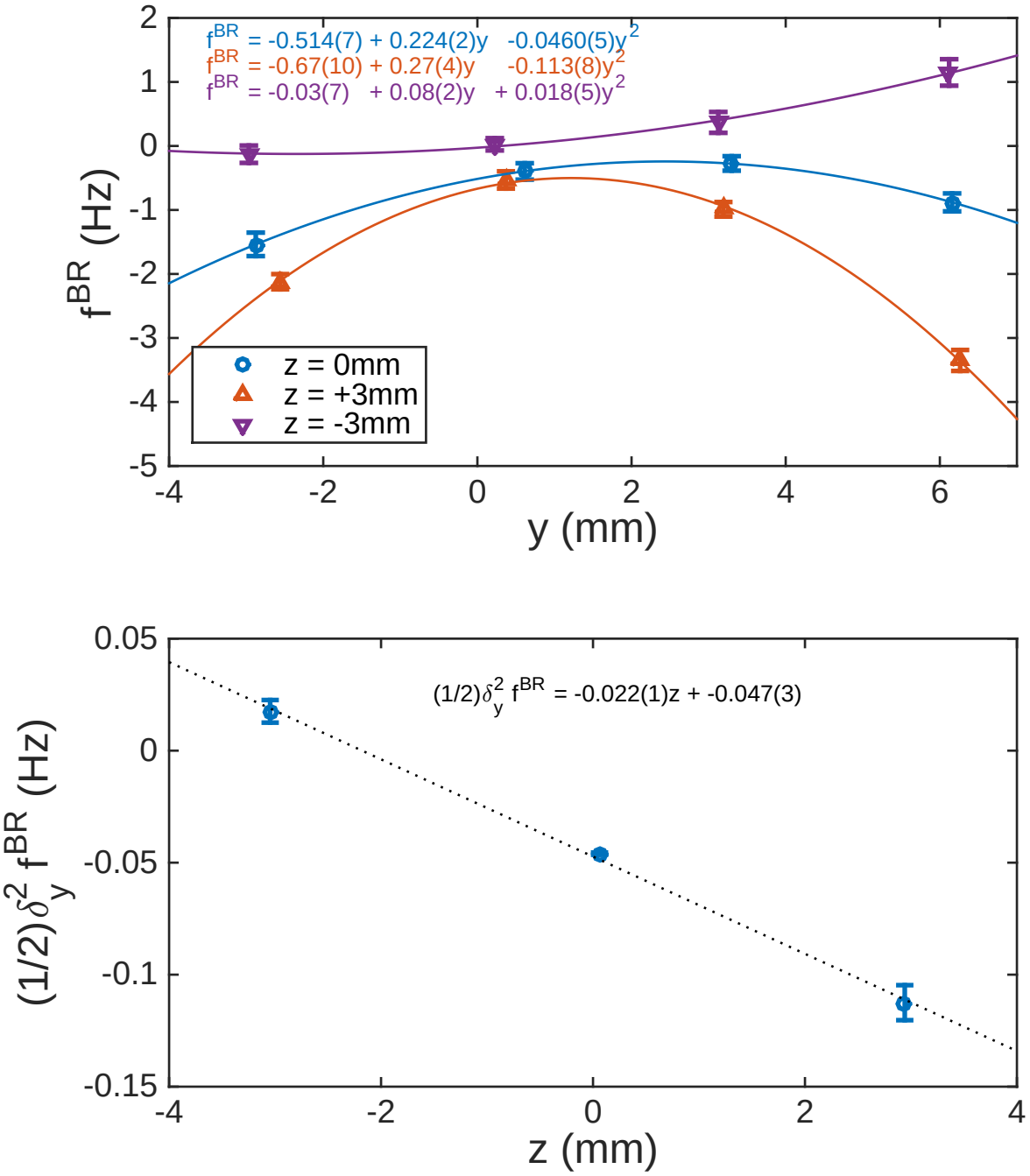

switch R, and will appear primarily in f^R. Indeed, we initially observed f^R shifts of several Hz when we generated the rotating electric field with cables attached to only one end of the trap electrodes. Currently we drive the electrodes symmetrically from both ends, and the typical f^R we measure is ~ 10 mHz.

- Motional fields are a systematic effect that have long plagued atomic beam electron EDM experiments. Motional magnetic fields due to the rotational micromotion in the trap will be on the order of $\vec{E}_{\rm rot} \times \vec{v}_{\rm rot}/c^2$, and which for typical experiment parameters will be 0.2 μGauss, and point in the axial direction. This is much less than Earth's ambient magnetic field in the axial direction of several hundred mGauss. The motional electric field due to rotational micromotion will be $\vec{B} \times \vec{v}_{\rm rot}$. This can create a Berry's phase α by tipping the molecular axis away from the horizontal plane. The Berry's phase α due to $\mathcal{B}_{\rm rot}$ will be on the order of 5×10^{-8} for typical experiment parameters. The Berry's phase due to static lab-frame fields will oscillate sinusoidally at $f_{\rm rot}$ with amplitude 10^{-5}.

- Earth rotates once on it's axis every 24 hours, which is a frequency of 11.7 μHz. This has the potential to break the rotation symmetry of the electric field rotating with angular momentum up and down in our experiment at the 11.7 μHz level in f^R.

- Time varying magnetic fields or magnetic field noise at frequencies near $f_{\rm rot}$ could potentially contribute to a non-reversing magnetic field observed in the f^B channel. We don't measure any significant noise features in the lab above 100 kHz. Additionally, the stainless steel ion trap chamber should provide some amount of shielding to rf noise such as this.

Chapter 5

Conclusion

5.1 A precision measurement of the electron EDM

5.1.1 Measurement overview

In this chapter we will discuss the logistics of compiling various pieces of data into a measurement of the electron EDM. We need to take lots of data in order to achieve good statistical sensitivity, and we need to account for all of the various potential systematic errors that were discussed in chapter 4. We will begin with a description of how the data is compiled.

The fundamental unit of data is the Ramsey fringe. To collect the data for the Ramsey fringe we step the time t between the $\pi/2$ pulses through several different values. We typically choose six to eight time steps per period of Ramsey oscillation and two to three periods, at least one at short time and one at long time. The points at short time are chosen from the first period, with the first of these points very close to time $t = 0$, see fig. 5.1. This allows us to get a good measurement of the initial phase ϕ of the Ramsey fringe. The second period is chosen at a time $t \approx \tau/2$, the time during the Ramsey fringe that has the most sensitivity to the Ramsey fringe frequency, as explained in chapter 3. We also have the option to not take the early time period and only take the long time period, assuming we have previously characterized the phase. This can gain us not quite a factor of $\sqrt{2}$ increase in sensitivity per $\sqrt{\text{time}}$ because we are not wasting half of our time taking short time data that contributes no frequency sensitivity. The increase is less than $\sqrt{2}$ because for a very long fringe the data rate for short time data is faster than the data rate of long time data.

For a typical fringe where the dead time t_{dead} is 300 ms and the long time data is at $t = 500$ ms we can expect an increase in sensitivity/$\sqrt{\text{time}}$ of $\sqrt{1100/800}$, or 17%. Additionally, when not taking the short time data we can fix the values ϕ and fringe offset as long as $\phi^{BD} = 0$ and $\mathcal{O}^{BD} = 0$, which also increased the frequency sensitivity by a factor of $\sqrt{3}$.

The data points are dispersed evenly throughout each period which means that no particular care needs to be taken to ensure that at least a couple of the points are on the sides of a fringe, where the maximum sensitivity can be attained. This is done at the cost of a factor of roughly $\sqrt{2}$ frequency sensitivity. We choose to pay this cost initially when we are exploring the space of experimental parameters because as we vary certain parameters the Ramsey fringe frequency can shift in sometimes difficult-to-predict ways, causing us to drift off the side of a Ramsey fringe and lose statistical sensitivity. The data that will be presented in this chapter was taken in the manner described above, but a set of data collected with the aim of truly attaining the highest sensitivity would have the times of the data points dialed in to the side of the Ramsey fringe.

At each time step in the Ramsey fringe we take several data points and average them together to achieve a better signal to noise ratio on the ion number measurement. We typically take fewer data points for early time periods (~ 12) and more data points for long time periods (~ 24) because the our signal is smaller and our duty cycle is longer at longer Ramsey fringe times. Additionally, we alternate data points between measuring the population in the $m_F = +3/2$ state and the $m_F = -3/2$ state. We refer to this as "chopping" between measuring the two different spin states. As described in chapter 2, we do this by changing the phase of the rotating electric field relative to the depletion pulse sequence. In a truly symmetric experiment we would chop between measuring the two different spin states and also preparing the initial population before the first $\pi/2$ pulse of the Ramsey experiment in the two different spin states. We currently do not do this, but there is no technical limitation preventing us, and we will implement this feature in our experimental sequence shortly. This fast chop between measuring the two different spin states allows us to measure $P(\uparrow)$ and $P(\downarrow)$ and construct the fringe asymmetry, eq. (3.15). After a single Ramsey fringe is acquired

Figure 5.1: Plotted in each sub-figure of (a) is the fringe asymmetry $\mathcal{A}$ against the time between $\pi/2$ pulses for a typical set of fringes in a block. The fringes oscillate at about 20 Hz, but the frequency is slightly different for each configuration of the switches B, D, and R. These 8 fringes can be combined according to the prescription in eq. (4.9) to make the frequency linear combination f^{BD}. In sub-figure (b) the EDM channel f^{BD} is shown for 6 different blocks, each comprising 8 Ramsey fringes, with the first block corresponding to the set of fringes shown in (a). This particular data were taken when we were investigating a large systematic effect (the anomalous effect that looks like $f^B \sim \vec{\mathcal{B}} \cdot \vec{r}$), which is why the f^{BD} channel in (b) varies over such a large range.

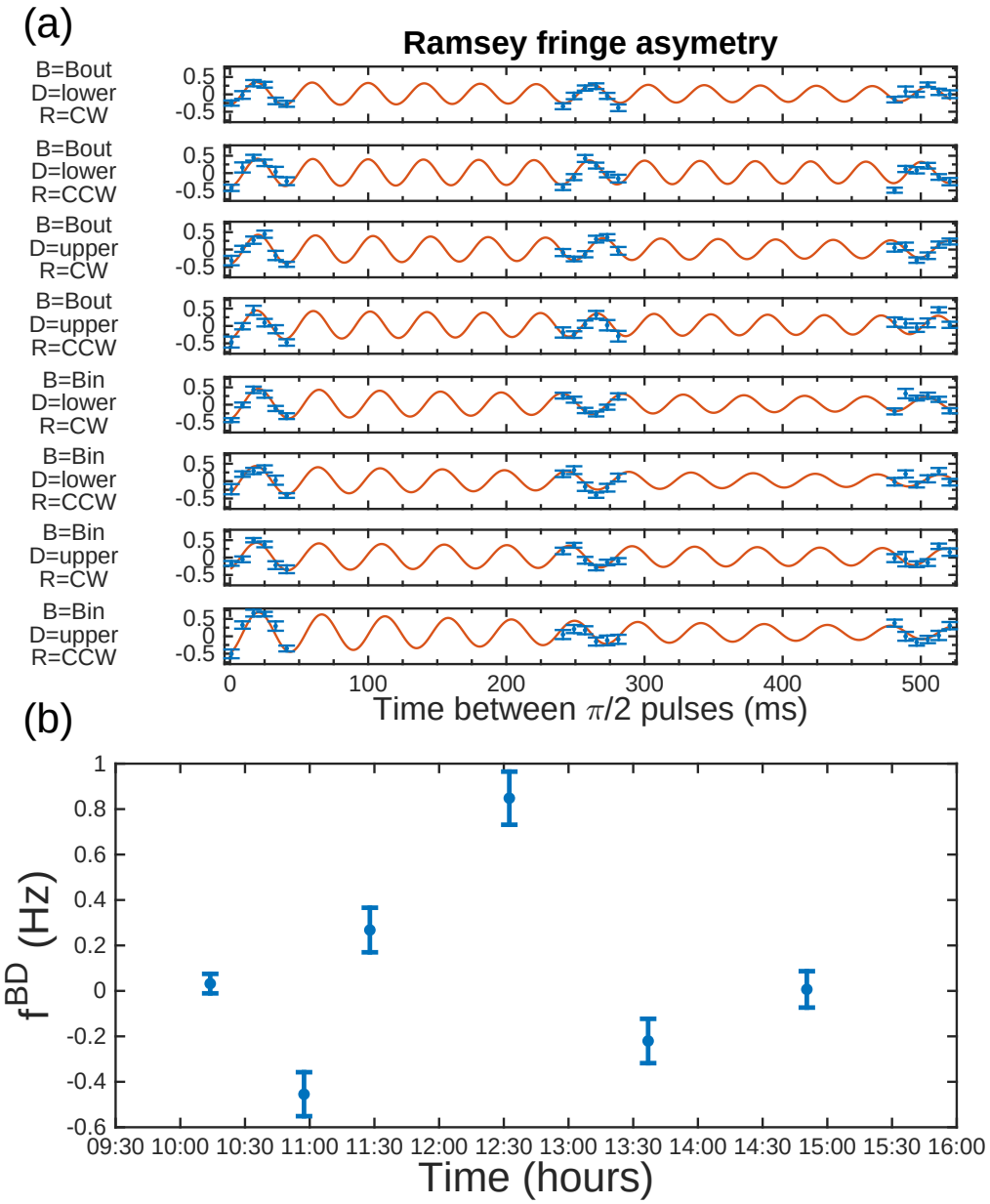

we fit it to the functional form eq. (3.26)

$$\mathcal{A}(t) = -\mathcal{C}(t/\tau)\cos(2\pi(ft+\phi)) + \mathcal{O}, \tag{5.1}$$

using nonlinear least squares analysis to extract the fringe frequency and other parameters. This Ramsey fringe is taken with a particular configuration of switches, i.e. rotating magnetic field $\mathcal{B}_{\text{rot}}$, doublet, and rotation direction. Several Ramsey fringes with parameters spanning the set of all possible parameter switch configurations are compiled into a "block". For the set of the three switches of B (rotating magnetic field direction), D (upper/lower doublet), and R (rotation direction), eight different Ramsey fringes will comprise a block. For a single block we are able to construct all of the various linear combinations of frequency, e.g. f^B, f^{BD}, as well as the linear combinations of the other data channels, e.g. ϕ, $\mathcal{C}$, ϕ^B, $\mathcal{O}^{BD}$. A set of 8 Ramsey fringes comprising a block and the value of f^{BD} for this block and 5 others taken in an afternoon are shown in fig. 5.1. With the current signal level of the experiment it typically takes about 32 minutes to acquire a block of 8 Ramsey fringes.

As discussed in chapter 4, the addition of each new switched parameter to the set of switches tends to suppress systematics in the EDM channel f^{BD} and isolate the effect of those systematics to other channels. For example, f^B has an exaggerated effect due to non-reversing magnetic fields compared to the EDM channel. While the addition of each new switched parameter does not decrease the frequency sensitivity per $\sqrt{\text{time}}$, it does have the practical disadvantage of increasing the time it takes to acquire a single block of data by a factor of 2^n, where n is the number of additional switched parameters. We therefore choose to operate with a reduced set of switches, $\{B, D, R\}$, in contrast to the larger set of all possible switches. We choose this set because it is a minimal set required to track the systematics that we have so far observed, i.e. f^B is a good measure of non-reversing magnetic fields, f^D is a good measure of rotation mixing effects Δ and $\delta\Delta$, etc. The timing of the various switches that make up a block are shown in fig. 5.2. We are aware of the danger of unknown, perhaps smaller systematic errors that we have not observed, possibly because we have chosen to focus so exclusively on a minimal set of switches. To defend

Figure 5.2: This the an example of a typical timing sequence of a series of switches in the EDM experiment.

(a) The fastest time scale of the experiment sequence. Every shot of the experiment, which in this case lasts 0.5 seconds, we switch between detecting ions in the $m_F = 3/2$ state and $m_F = -3/2$ state.

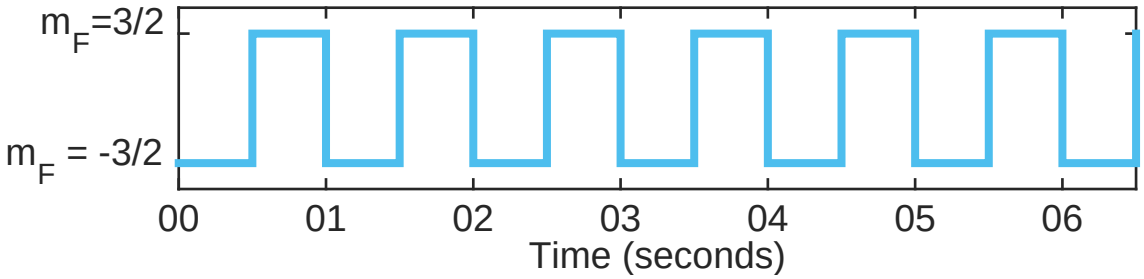

(b) Shown below is a single Ramsey fringe of a single block of data. The time between $\pi/2$ pulses is stepped through values ranging from 0 ms to 500 ms.

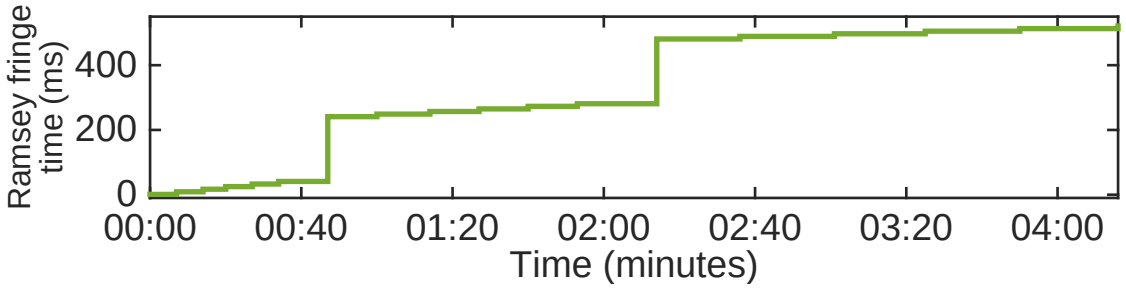

(c) Shown below are 4 blocks of data, with B (rotating magetic field direction switched at the fastest rate, followed by D (doublet), followed by R, (rotation direction). At the "super-block" level an additional parameter S is varied between 4 different values.

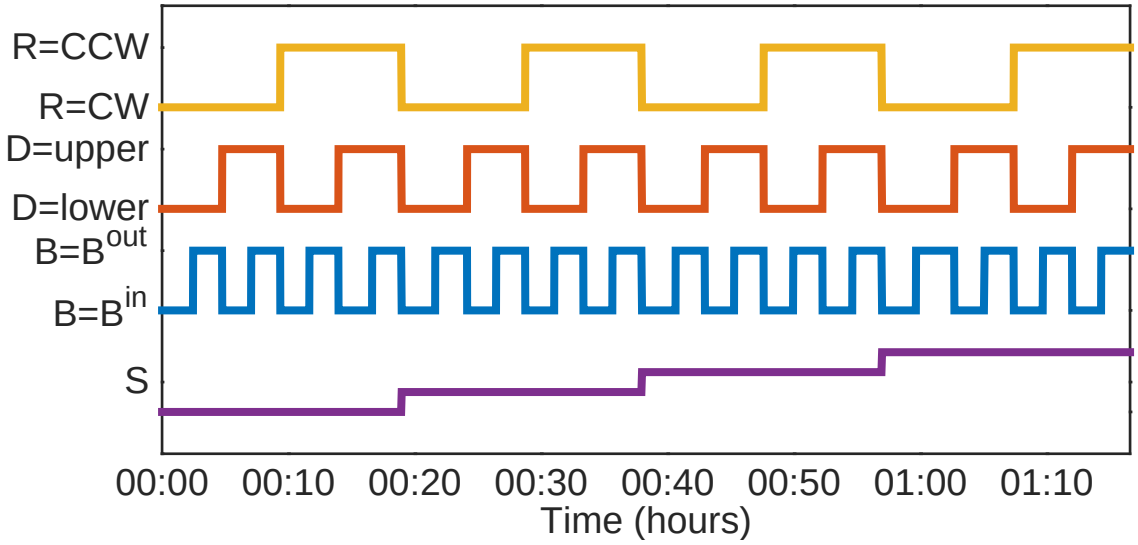

against this we can perform additional switches above the block level, for example in a sequence of 100 blocks, we will alternate one of these switches every 10 blocks. We then have the ability to average over these switches or to form new linear combinations of data channels that are odd under these switches. Examples of switches we might consider performing at the "super-block" level are:

- Depletion laser polarization σ^+/σ^-
- Rotating electric field magnitude (between two values, e.g. 24 V/cm and 16 V/cm)
- Rotating magnetic field value (between two values, e.g. 2 mGauss and 4 mGauss)
- Ion cloud center of mass trap position (+offset/-offset) in $\hat{x}, \hat{y}, \hat{z}$ directions
- Ramsey fringe time t (between two values e.g. 400 ms and 600 ms)
- Number of ions loaded into the trap

This prescription can be used to assemble a large amount of data suitable for a robust EDM measurement. For a measurement of the electron EDM with the current level of demonstrated statistical sensitivity we expect to take about 100 hours of data, comprising several hundred blocks and achieve a total statistical uncertainty of several 10^{-28} $e\cdot$cm .

5.1.2 Data blinding

In the conclusion of his paper on the measurement of e/m of the electron, Frank Dunnington had the following to say about the role of an expectation bias in experiment[22],

> It is also desirable to emphasize the importance of the human equation in accurate measurements such as these. It is easier than is generally realized to unconsciously work toward a certain value. One cannot, of course, alter or change natural phenomena ... but one can, for instance, seek for those corrections and refinements which shift the results in the desired direction. Every effort has been made to avoid such tendencies in the present work.

Indeed, Dunnington blinded his own measurement of e/m by having the angle between his electron source and his electron detector kept secret from him, only measuring it once he finished his

final analysis of all the other factors that could affect e/m. By blinding himself from his data in this way he prevented himself from unintentionally biasing his final result by the results of other experiments that came before him. Expectation bias in an electron EDM precision measurement is a real concern, because the difference between a zero and nonzero result has profound implications for physical theory. Many other groups have made very precise measurements that are consistent with zero, and a worry is that we will unintentionally bias our result in some way such that it is consistent with zero as well. This concern that expectation bias can affect the outcome of a precision measurement is well founded, if we look at historical measurements of the speed of light in fig. 5.3, we see a possible example of expectation bias influencing the outcome of an experiment. The series of measurements made in the 1930s are consistent with each other, but deviate from the true value by several standard deviations. A possible scenario where this can occur in a precision measurement experiment is if systematic errors are searched for and eliminated until the outcome of the experiment matches the experimenter's expectation, and then the search is ceased.

It is important that we don't bias ourselves on the outstanding electron EDM measurements made in the past, and blinding our data as Dunnington did is a potential way to ensure that we don't accidentally do so. At the same time, the experiment we have described is rather complicated, and we fear that blinding might obscure some problematic irregularity in the experiment, or make diagnostic analysis more difficult. There is also the concern that the blind might be difficult or even impossible to remove, ruining large amounts of data. We therefore adopt the philosophy that we should be "blind, but not dumb". We will choose to blind our data by adding an unknown offset to the EDM channel, and the offset will be dynamically added in at the last possible step in processing. Additionally, we choose to apply a small blind offset. We choose a random offset that is on the order of $\pm 1 \times 10^{-28}$ e·cm, as this will be undetectably small for any but the largest sets of our data, but it is still larger than the statistical uncertainty of the most recent EDM experiment (0.41×10^{-28})[7]. We will also add to the blind a known offset of 3×10^{-28} e·cm, which will serve to reassure us that the blind is in place and operating in the analysis like we expect. Dunnington did something similar in his e/m measurement, when he ordered the angle between his detector

Figure 5.3: Historical measurements of the speed of light, taken from [40]. The four measurements made in the 1930s are each consistent with the previous measurement but are several σ away from the true value.

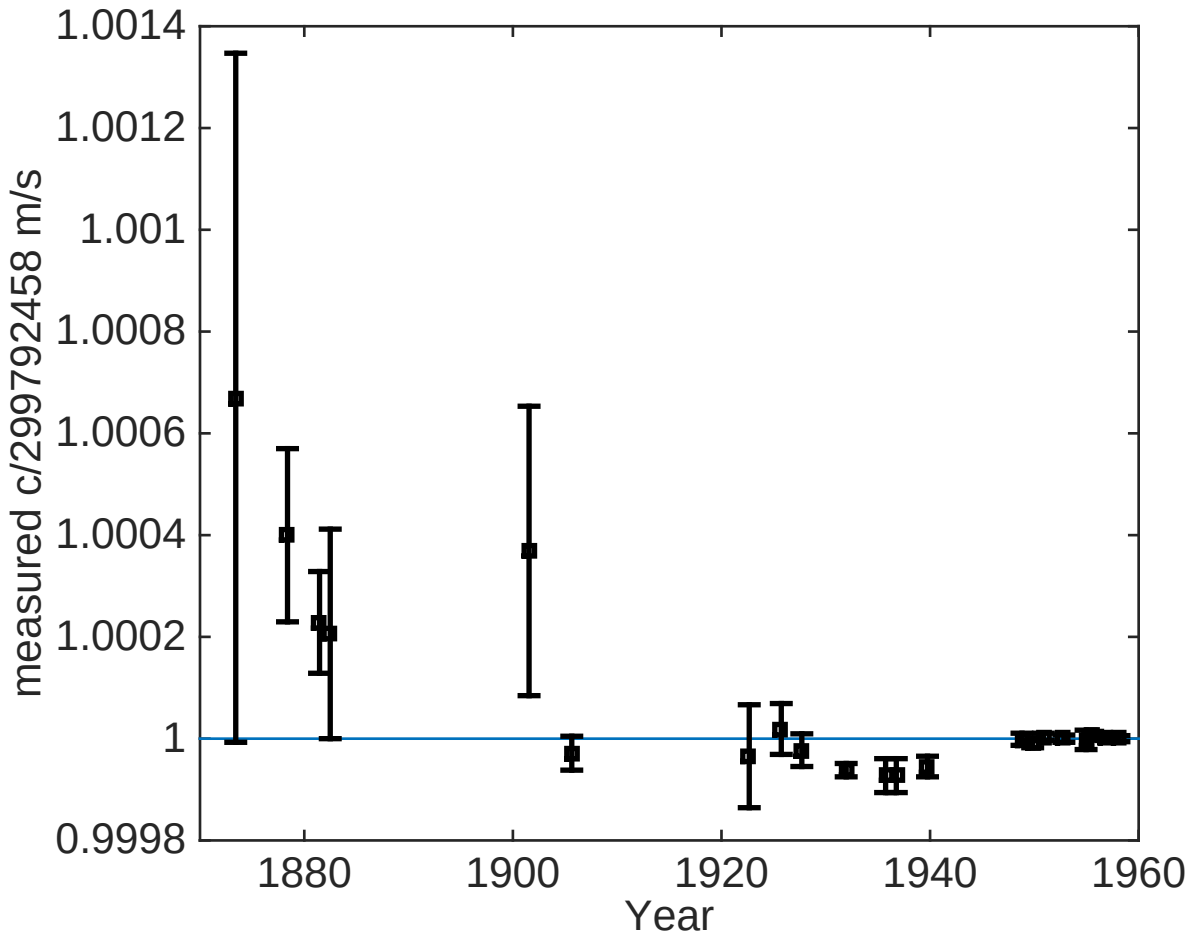

and source to be constructed at an angle of approximately 140°, but that he not be told the exact angle chosen.

Whenever we look at the frequency linear combinations of a block or blocks, a function is called which loads the raw data containing the frequencies of the Ramsey fringes that comprise the blocks. This function then calculates the frequency linear combinations according to the prescription eq. (4.9). Then, in what is quite literally the last step before the function returns the linear combinations to the user, we load the value of the blind from the network disk and add it to f^{BD},

```
lcom_table.fBD = lcom_table.fBD + fread(fopen('X:\BLIND\BLIND'),1,'double');
fclose('all');
```

The blind is added to the EDM channel at the last step before it is passed back to the user for further analysis. The full analysis procedure is detailed in appendix B. The blind that we apply is stored in a file on the network file system accessible to every computer in the lab. The file contains an 8 byte binary representation of one double precision floating point number. This number was the result of choosing a random number from a Gaussian distribution centered at 3.38 mHz with 1σ width of 1.13 mHz. This is a distribution equivalent to $3 \pm 1 \times 10^{-28}$ e·cm in EDM units for HfF^+. This random number was chosen once on January 9th, 2015, and it has been used in all analysis since then. This is important because it allows us to compare various blinded data sets, as they all have the same blind offset added. We chose a blind that intentionally has a bias of 3×10^{-28} e·cm. The reason is to be sure that we are actually applying the blind, and that we are applying it correctly, with the correct sign. Removing the blind is trivial, we simply comment out the relevant line from our analysis file, and look for a $\sim$ 3.38 mHz shift in the f^{BD} channel. We can then take the binary number from the BLIND file and convert it to a human readable double precision floating point and confirm that it matches the observed shift.

It is important to remember that this blind only affects the mean value of the f^{BD}, or EDM, channel. The other channels are not blinded, that is to say the values of f^B and f^R are the true values the experiment measures. This is important because these channels will be used as diagnostics to make sure the experiment is working correctly, and if a blind offset were applied to

them it would cause us to think that there existed a fictitious non-reversing magnetic field, in the case of f^B, or that there was some problem with the reversibility of rotation, in the case of f^R. Another feature of the blind is that it does not affect the variance of the data in the f^{BD} channel at all, so we can analyze the statistics of blinded f^{BD} data.

5.1.3 Blinded EDM measurement

We have collected almost 500 blocks comprising over 380 hours of EDM data since January 2015. Of this data, almost 150 hours was taken at deliberately offset axial positions in the trap and with deliberately applied static axial magnetic fields, often with unintentionally applied axial magnetic field gradients. We won't consider any of this data taken to study systematics in the following sections. Of the remaining 233 hours of data we will veto 2 hours worth of data blocks with fitting error bars for frequency greater than 150 mHz. The rationale behind this is that this data is the most likely to have Ramsey fringes that misfit, or was taken under conditions with not enough statistical sensitivity (i.e. short Ramsey fringe times or poor Ramsey fringe contrast). This cut is not biased by any of the actual measured values so it seems fair to do. We will also veto 8 hours of data with $\left|f^B\right| > 2$ Hz. This is necessary, as much of this data was taken under extreme conditions as we studied systematic effects, and vetoing this data allows us to remove the most extreme of those experiments. Note that 2 Hz is a much wider range than the ultimately possible 30 mHz we hope to achieve in the future by actively shimming non-reversing gradients and ion cloud trap position. For the majority of the remaining data no attempt whatsoever was made to stabilize f^B or the ion cloud trap position on even a day-to-day basis. A summary of this data is show in fig. 5.4.

After applying the above vetoes we are left with a data set of 223 hours. For measurements between the $m_F = +3/2$ and $m_F = -3/2$ state of $^3\Delta_1$ of $HfF^+$the 23.3 GV/cm internal electric field means a 1.13 mHz shift corresponds to a d_e of 10^{-28} e·cm. The f^{BD} EDM channel, after the 3×10^{-28} e·cm offset has been removed, has a mean of 0.015 ± 3.13 mHz, or $0.013\pm2.77\times10^{-28}$ e·cm, which is consistent with 0 and the 1×10^{-28} e·cm blind. The non-reversing magnetic field channel

Figure 5.4: This is 500 blocks of EDM data, roughly 380 hours, all the data taken to date. From this we removed almost 150 hours of data: 140 hours that was part of studies of systematic effects where we varied the axial position of the ion cloud in the trap and where we varied the axial magnetic field, and 10 hours where f^B, the non-reversing magnetic field, was larger than 2 Hz, or where the frequency fit error bars were large than 150 mHz. These vetos can be seen as gaps in the data in (a), in particular around measurements 250 and 420. Additionally the normal probability plot (b) shows that the data is well Gaussian distributed.

(a) Time series of f^{BD} taken to date. The gaps are due to the vetos described above.

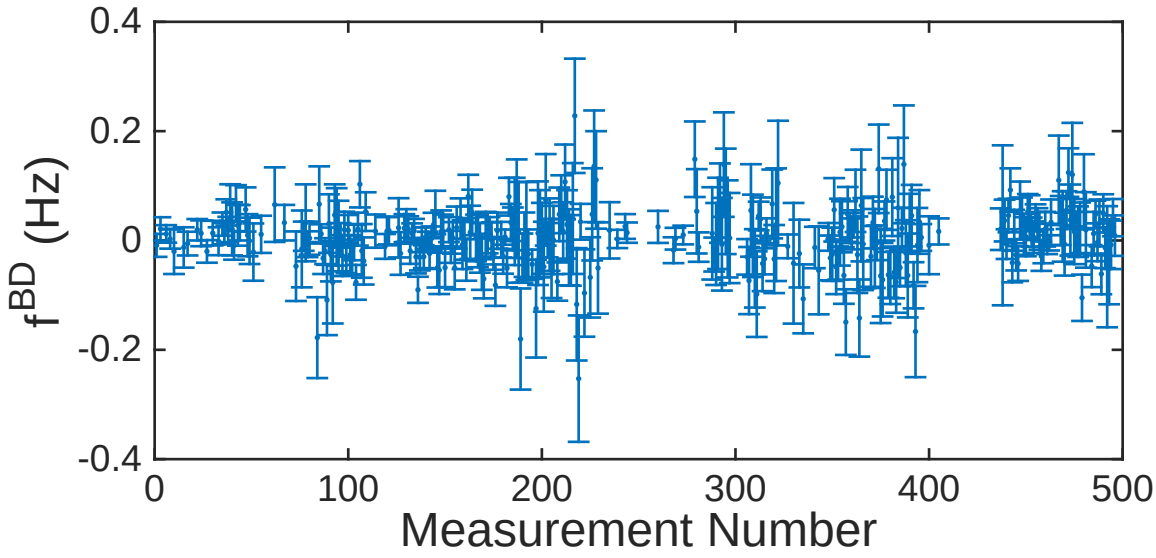

(b) Normal probability plot of $(f^{BD} - \overline{f^{BD}})/\sigma_f$. The plot is constructed by ordering the data and then plotting the sample data on the x-axis against the theoretical quantiles of the data on the y-axis. Gaussian distributed data will lie along the straight dashed line. Distributions with thin tails will curve down on the left and up on the right (like an 'N'), and distributions with fat tails will do curve up on the left and down on the right (like an 'S').

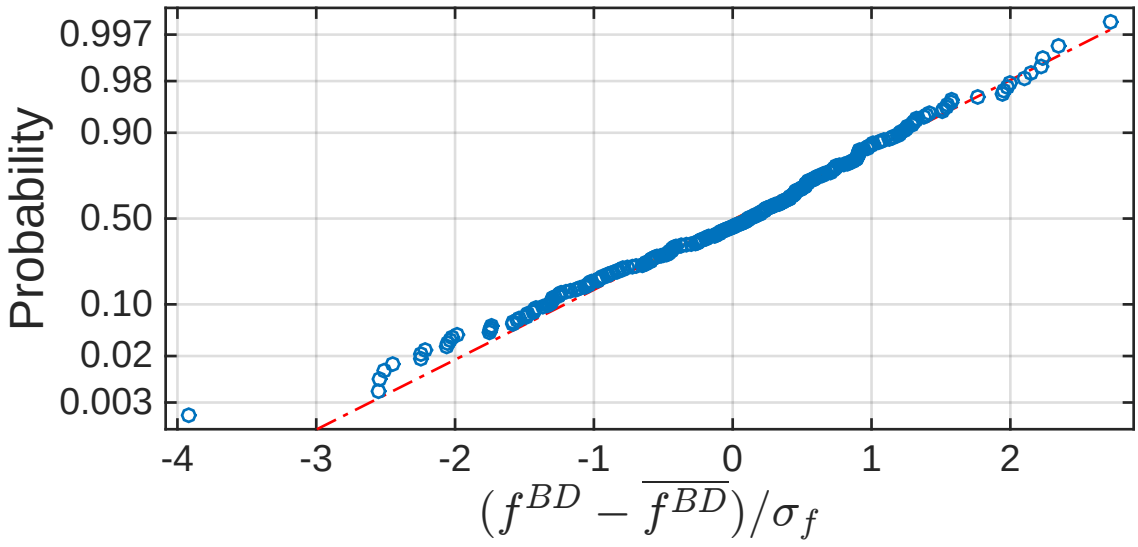

mean value is $f^B = -21.3 \pm 3.1$ mHz. The uncertainty stated for the mean value is the rms value of the individual f^B measurement uncertainties divided by $\sqrt{N}$. The variation in f^B in this data set can be quantified by the block rms value of 700 mHz. The mean, uncertainty, and variance of f^B will be of particular importance in the upcoming discussion of the systematic effects present in this data.

5.1.4 Systematic corrections

Many of the systematic terms appearing in f^{BD} discussed in section 5.1.5 can be efficiently diagnosed with the remaining frequency linear combinations, allowing us to calculate corrections and their uncertainties from the data itself. For example, a non-reversing magnetic field can be effectively measured with f^B because the leading term is $3g_F\mu_B\delta\mathcal{B}$. We may use these diagnostic terms to subtract off understood systematic effects from the f^{BD} channel. For example, the leading order terms of f^0, f^B, f^D, and f^{BD} due to non-reversing magnetic field $\delta\mathcal{B}$ and rotation terms Δ and $\delta\Delta$ are:

$$f^0 = 3\mu_B g_F \mathcal{B}_{\text{rot}} \left(1 + \frac{\Delta^2 + \delta\Delta^2}{2(3\mu_B g_F \mathcal{B}_{\text{rot}})^2}\right) + h.o., \tag{5.2}$$

$$f^B = 3g_F\mu_B\mathcal{B}_{\text{rot}} \left(1 - \frac{\Delta^2 + \delta\Delta^2}{2(3g_F\mu_B\mathcal{B}_{\text{rot}})^2}\right)\left(\frac{\delta\mathcal{B}}{\mathcal{B}_{\text{rot}}}\right) + h.o. \tag{5.3}$$

$$f^D = 3g_F\mu_B\mathcal{B}_{\text{rot}} \left(\frac{\delta g}{g_F} + \frac{\Delta\delta\Delta}{(3g_F\mu_B\mathcal{B}_{\text{rot}})^2}\right) + h.o., \tag{5.4}$$

$$f^{BD} = 3g_F\mu_B\mathcal{B}_{\text{rot}} \left(\frac{\delta g}{g_F} - \frac{\Delta\delta\Delta}{(3g_F\mu_B\mathcal{B}_{\text{rot}})^2}\right)\left(\frac{\delta\mathcal{B}}{\mathcal{B}_{\text{rot}}}\right) + 2d_e\mathcal{E}_{\text{eff}} + h.o. \tag{5.5}$$

We see there is a high degree of overlap between these channels. This allows us to use this linear vector space to construct a nonlinear subspace that is more closely aligned with the $2d_e\mathcal{E}_{\text{eff}}$ term than f^{BD},

$$f^{BD} + f^D\frac{f^B}{f^0} = 2d_e\mathcal{E}_{\text{eff}} + 3g_F\mu_B\mathcal{B}_{\text{rot}}\left(\frac{\delta g}{g_F}\right)\left(\frac{\delta\mathcal{B}}{\mathcal{B}_{\text{rot}}}\right)\left(2 - \frac{\Delta^2 + \delta\Delta^2}{(3g_F\mu_B\mathcal{B}_{\text{rot}})^2}\right) + h.o. \tag{5.6}$$

The three highest order terms remaining after this correction are roughly 100μHz, 1μHz, and 0.1μHz respectively, or roughly 1.1×10^{-29} $e\cdot$cm, 1.1×10^{-31} $e\cdot$cm, and 1.1×10^{-32} $e\cdot$cm. With

Figure 5.5: The systematic correction $f^D f^B/f^0 - 2(\delta g/g_F)f^B$ is in good agreement with the measured shift in f^{BD}. The dashed line has a slope of 1 and intersects the origin. This data was taken with a non-reversing magnetic field contribution spanning 30 Hz, and under an assortment of axial magnetic fields $\mathcal{B}_z$, contributing to a range of f^D measurements spanning ranging from -0.1 to -0.6 Hz. Even so, when synthesized in this way we can essentially entirely remove the effect of the non-reversing mangetic field and $\mathcal{B}_z$ from f^{BD}.

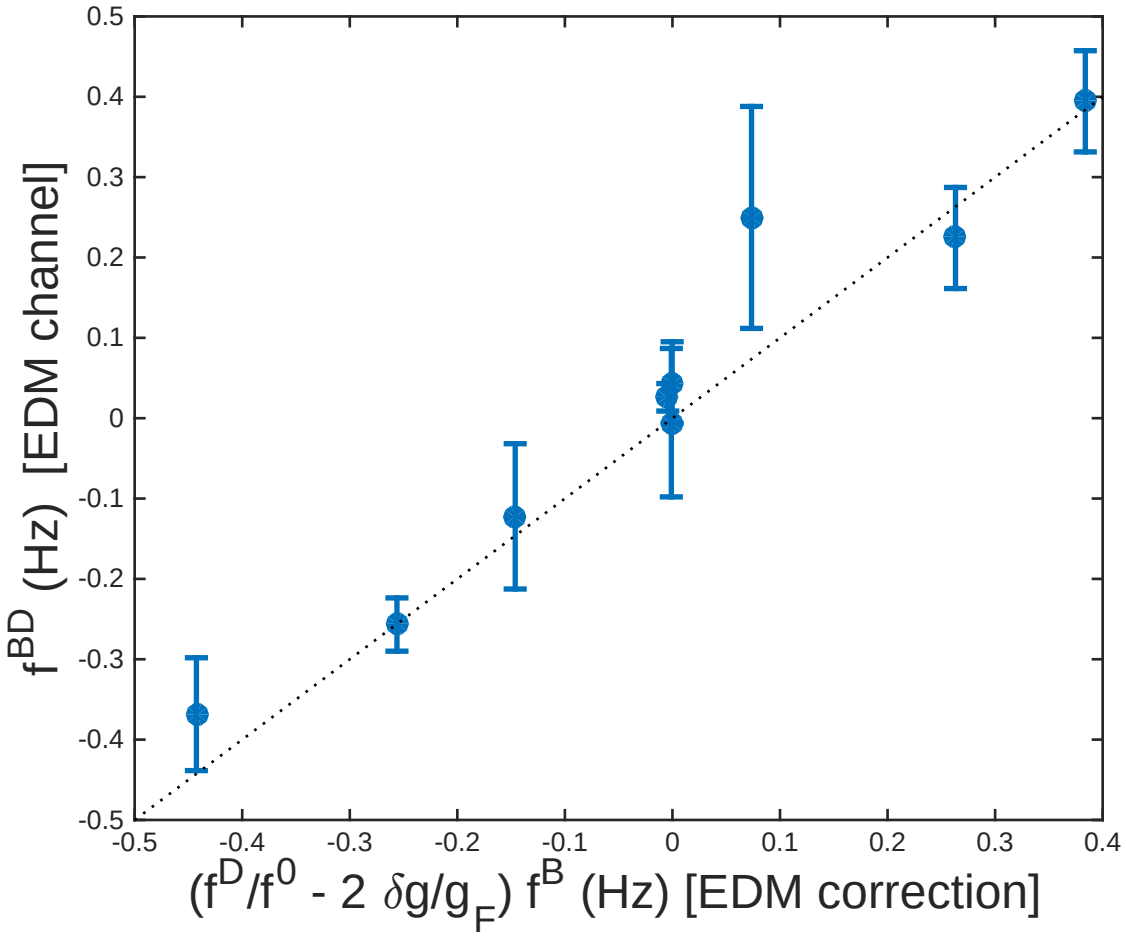

prior knowledge of the quantity $(\delta g/g_F)$ we can go even further,

$$f^{EDM} \equiv f^{BD} + f^D \frac{f^B}{f^0} - 2f^B(\delta g/g_F) = 2d_e\mathcal{E}_{\text{eff}} - \frac{2\Delta^2\delta\Delta^2}{(3g_F\mu_B\mathcal{B}_{\text{rot}})^3}\left(\frac{\delta g}{g_F}\right)\left(\frac{\delta\mathcal{B}}{\mathcal{B}_{\text{rot}}}\right) + h.o, \tag{5.7}$$

where now the final term in eq. (5.7) is 10 nHz.

Constructing $f^{BD} + f^D\frac{f^B}{f^0} - 2f^B(\delta g/g_F)$ can very efficiently isolate the EDM contribution to the Ramsey frequency linear combination f^{BD}, and there are advantages and disadvantages to this treatment. The advantage to this type of correction is that it is internally self consistent. It will work for a variety of $\mathcal{B}_{\text{rot}}, \mathcal{E}_{\text{rot}}, \omega_{\text{rot}}, \Delta$, and $\delta\Delta$, as demonstrated in fig. 5.5. But does this construction add statistical or systematic error to our measurement of the EDM? When we make a measurement and label it f^B, it is to leading order $3g_F\mu_B\mathcal{B}_{\text{rot}}(\delta\mathcal{B}/\mathcal{B}_{\text{rot}})$ plus some error, ϵ_{f^B}. When we make measurements of f^B with some uncertainty σ_{f^B}, that is a statement of the size of the upper bound of ϵ_{f^B}, i.e. ϵ_{f^B} is a random number drawn from a Gaussian distribution with standard deviation σ_{f^B}. We can estimate the uncertainty of the systematic corrections to the EDM measurement by propagating errors on eq. (5.7).

$$\begin{aligned}\sigma^2_{EDM} =& \sigma^2_{f^{BD}} + \left(\frac{f^B}{f^0}\right)^2\sigma^2_{f^D} + \left(\frac{f^D}{f^0}\right)^2\sigma^2_{f^B} + \left(\frac{f^B}{f^0}\frac{f^D}{f^0}\right)^2\sigma^2_{f^0} + \left(2\frac{\delta g}{g_F}\right)^2\sigma^2_{f^B} + \left(2f^B\right)^2\sigma^2_{\delta g/g_F},\\ =& \sigma^2_f\left(1 + \left(\frac{f^B}{f^0}\right)^2 + \left(\frac{f^D}{f^0}\right)^2 + \left(\frac{f^B}{f^0}\frac{f^D}{f^0}\right)^2 + \left(2\frac{\delta g}{g_F}\right)^2\right) + \left(2f^B\right)^2\sigma^2_{\delta g/g_F},\end{aligned} \tag{5.8}$$

Where $\sigma_{\delta g/g_F}$ is the uncertainty in the determination of $\delta g/g_F$. Above we have used the fact that each of the channels f^0, f^B, etc. all have the same uncertainty σ_f, because they were formed by sums or differences of the same eight frequency measurements. We find that in the case $f^B \ll f^0$ and $f^D \ll f^0$ the correction f^Bf^D/f^0 introduces systematic error at the level of a fraction of the statistical uncertainty of our measurement. For typical parameters $f^0 \approx 20$ Hz, $f^D \approx -0.2Hz$, and $f^B \ll 0.2$ Hz, so these conditions are satisfied and the systematic error is at the level of 1% of the statistical uncertainty. For the correction $-2f^B(\delta g/g_F)$, the systematic error amounts to replacing $(\delta g/g_F)$ with $\sigma_{\delta g/g_F}$ in our expansions, so as long as we measure $(\delta g/g_F)$ to enough precision such that $\sigma_{\delta g/g_F} \ll (\delta g/g_F)$ then we are also better off with this correction term. For typical values of the experimental parameters we have experimentally verified that $\delta g/g_F$ agrees

well with the theoretical calculations from eqs. (4.19) and (4.21). We will therefore use calculated value $\delta g/g_F = 0.000993$ and use the measurement verification uncertainty for $\sigma_{\delta g/g_F} = 0.0001$.

This will be our general strategy for calculating systematic error corrections and estimating the uncertainty of these corrections in section 5.1.5. For any of the systematic errors will discuss we can use a combination of the diagnostic frequency channels f^B, f^D, etc. and other measurably quantities to calculate the mean value of the correction and then perform propagation of uncertainties to estimate the total uncertainty of the correciton.

A potential danger of this technique is systematic effects that appear in f^B and other channels that we do not understand. Recall from section 4.3 the systematic that appears as $f^B \sim \vec{\mathcal{B}} \cdot \vec{r}$. It is still unclear whether this effect appears in the effective two state Hamiltonian as a coefficient of $(g_F \pm \delta g)$ or not. However, due to the lack of any dependence on Ramsey fringe frequency it must at the very least appear as a B odd term in the diagonal of the Hamiltonian, therefore this technique should still be applicable. Indeed, this is established in fig. 4.13, where the correction $f^D f^B/f^0$ is applied and the effect due to $\vec{\mathcal{B}} \cdot \vec{r}$ is suppressed in the EDM channel. Therefore, we expect applying this correction to have a systematic residual of $f^B(\delta g/g_F)$, due to the uncertainty of whether or not the $f^B \sim \vec{\mathcal{B}} \cdot \vec{r}$ effect interacts with $(g_F \pm \delta g)$. We could settle this question by making a very precise measurement of the $f^B \sim \vec{\mathcal{B}} \cdot \vec{r}$ at very high frequency f^0 and looking for any correlation in f^{BD}. At $f^0 = 200$ Hz the component of $\delta g_{eff}/g_F$ due to $\Delta\delta\Delta$ is about 0.0001, which is much less than the contribution due to $\delta g/g_F \approx 0.001$. We can apply a 30 Hz shift to f^B and try to observe the 30 mHz shift in f^{BD}. This will probably require about 10 hours of data to be convinced of the presence of absence of any effect.

Another possible avenue of exposure to systematic errors is if the assumption that terms that enter into the corrections are independent. If we consider the correction to the systematic error due to only non-reversing magnetic field and differential g-factor,

$$f^{\delta g/g_F} = -2\frac{\delta g}{g_F} f^B, \tag{5.9}$$

then the uncertainty of this correction, calculated by propagation of uncertainty is,

$$\sigma^2_{f^{\delta g/g_F}} = \left(-2\frac{\delta g}{g_F}\right)^2 \sigma^2_{f^B} + \left(f^B\right)^2 \sigma^2_{\delta g/g_F} + 2\left(-2\frac{\delta g}{g_F} f^B\right)\sigma_{\delta g/g_F, f^B}. \tag{5.10}$$

In the above discussion we have tacitly assumed that all covariance terms such as $\sigma_{\delta g/g_F, f^B}$ are zero, i.e. that all of the quantities that enter into the corrective terms are independent. This is true for the various frequency combinations f^B, f^D, etc., which by construction are linearly independent. However it is possible that the differential g-factor could have some dependence on non-reversing magnetic field, which would yield a $\sigma_{\delta g/g_F, f^B}$ that is nonzero. This is perhaps a safe assumption because eqs. (4.19) and (4.21) show that $\delta g/g_F$ has a dependence on $\mathcal{E}_{\text{rot}}$ and ω_{rot}, but not non-reversing magnetic field. However these calculations were only made to first order, and it is possible that the quadratic Zeeman effect could contribute to a $\delta g/g_F$ that depends on magnetic field, which would leave us vulnerable to additional systematics not discussed here.

5.1.5 Systematics

The data presented in fig. 5.4 are influenced by several potential systematic errors. We reviewed these possible effects in chapter 4, and we will summarize them here and quantify their effect for this data. Essentially all of these systematic effects arise because of some interaction with non-reversing magnetic field $\delta\mathcal{B}$. We will separate the discussion into several parts based on the various exact mechanisms through which non-reversing magnetic field can present as a systematic, but the treatment overall will be very similar.

5.1.5.1 Non-reversing magnetic field

Non-reversing magnetic fields are odd under the switch B, and they can combine with any effect that is odd under doublet switch D to provide a systematic in f^{BD}. The two primary effects that are odd under doublet switch are the differential g-factor between the two doublets, $(\delta g/g_F)$, and the difference in rotation-induced mixing Δ, the $\delta\Delta$ term. The predicted contribution to f^{BD}

due to these two effects is given in eq. (4.26),

$$f^{BD} \sim 3g_F\mu_B\mathcal{B}_{\rm rot}\left(\frac{\delta\mathcal{B}}{\mathcal{B}_{\rm rot}}\right)\left(\frac{\delta g}{g_F} - \frac{\Delta\delta\Delta}{(3g_F\mu_B\mathcal{B}_{\rm rot})^2}\right). \tag{5.11}$$

We will separately consider the contributions due to $(\delta g/g_F)$ and $\delta\Delta$ and develop systematic corrections for each. We can use the correction developed in section 5.1.4 to estimate the size of this term in a self consistent way using the diagnostic channels f^B, f^D, and f^0. First we consider the systematic due to $\delta\Delta$. The correction for this term is

$$f^{\Delta\delta\Delta} = \frac{f^B f^D}{f^0}, \tag{5.12}$$

and the uncertainty of this term is

$$\sigma^2_{f^{\Delta\delta\Delta}} = \sigma_f\sqrt{\left(\frac{f^B}{f^0}\right)^2 + \left(\frac{f^D}{f^0}\right)^2 + \left(\frac{f^B}{f^0}\frac{f^D}{f^0}\right)^2}. \tag{5.13}$$

Taking the mean of $f^{\Delta\delta\Delta}$ across our data set yields as correction of 0.238 mHz. The uncertainty of this correction can be found by calculating $\sigma^{\Delta\delta\Delta}$ for every point in the data set and then taking the block rms value divided by $\sqrt{N}$, where N is the length of the data set. This yields an uncertainty of 0.114 mHz. This uncertainty is dominated by the size of f^B, the block rms value of which is 700 mHz. If instead f^B was actively servoed to an rms value of 30 mHz, and the Ramsey fringe frequency was changed to 50 Hz, then the total systematic error contribution due to f^B would drop to 2 μHz. The next largest contribution is from f^D, which has an average value of -320 mHz due to $\Delta\delta\Delta$. With a ramsey fringe frequency of 50 Hz the total systematic uncertainty contribution from this correction is 20 μHz.

The correction to the systematic term due to $(\delta g/g_F)$ is

$$f^{\delta g/g_F} = -2\frac{\delta g}{g_F}f^B, \tag{5.14}$$

which using the calculated value of $\delta g/g_F = -0.000993$ and the mean value of $f^B = -21.3$ mHz is a correction of $f^{\delta g/g_F} = -0.043$ mHz. The uncertainty of this term is

$$\sigma^2_{f^{\delta g/g_F}} = \left(-2\frac{\delta g}{g_F}\right)^2\sigma^2_{f^B} + \left(f^B\right)^2\sigma^2_{\delta g/g_F} + 2\left(-2\frac{\delta g}{g_F}f^B\right)\sigma_{\delta g/g_F, f^B}. \tag{5.15}$$

If we proceed with the assumption that $\delta g/g_F$ is independent of f^B, then this is $\sigma^{\delta g/g_F} = 10$ μHz. This is about evenly split between the contribution due to the uncertainty of $\delta g/g_F$, $\sigma_{\delta g/g_F} = 0.0001$ and the single frequency measurement uncertainty σ_{f^B}. If we were to decrease the uncertainty of $\delta g/g_F$ or decrease the rms value of f^B this will decrease this uncertainty by about a factor of $\sqrt{2}$. Moreover, it will limit our exposure due to underestimating the systematic error uncertainty due to correlated effects, i.e. $\sigma_{\delta g/g_F, f^B} \neq 0$.

5.1.5.2 Axial magnetic field

Axial magnetic fields have the effect of shifting Δ and $\delta\Delta$, as described by eq. (4.30). This combines with any non-reversing magnetic field to give a systematic effect in f^{BD}, described in eq. (4.35),

$$f^{BD} \sim 3 g_F \mu_B \mathcal{B}_{\rm rot} (-15) \left(\frac{g_F \mu_B \mathcal{B}_z}{\omega_{rot}} \right)^2 \left(\frac{\delta \mathcal{B}}{\mathcal{B}_{\rm rot}} \right) \left(\frac{\Delta \delta \Delta}{(3 g_F \mu_B \mathcal{B}_{\rm rot})^2} \right). \tag{5.16}$$

For this set of data no effort was made to null out the axial magnetic field. We measured that the axial magnetic field at the center of the trap due to the ambient Earth's magnetic field is $\mathcal{B}_z = -0.35(1)$ Gauss, where negative is in the same direction as gravity. We can use the $\Delta\delta\Delta$ component of the non-reversing magnetic field and multiply by $-15(g\mu_B \mathcal{B}_z/\omega_{\rm rot})^2 = -0.0005$ to get the systematic error contribution of axial magnetic fields, which is 0.122 ± 0.103 μHz. This is on the order of 10^{-31} $e\cdot$cm, and we note it will only get smaller when the non-reversing magnetic field is actively shimmed and Ramsey fringe frequency increased.

5.1.5.3 Field inhomogeneities

There are two systematic errors that can affect f^{BD} that are due to field inhomogeneities. As described in chapter 4 field inhomogeneities can give rise to an average tipping angle α of the molecule axis with respect to the plane of rotation. A non-zero tipping angle results in a Berry's phase effect $f_{\rm Berry} = 3\omega_{\rm rot}\alpha$. which is odd under magnetic field reversal B, which can couple with axial magnetic fields to be even under rotation direction R, as well as couple to the differential

rotation-induced coupling $\delta\Delta$ to give an effect that is odd in D, as explained in eq. (4.44),

$$f^{BD} \sim 3g_F\mu_B\mathcal{B}_{\rm rot}(6)\left(\frac{3\alpha\omega_{rot}}{3g_F\mu_B\mathcal{B}_{\rm rot}}\right)\left(\frac{g_F\mu_B\mathcal{B}_z}{\omega_{rot}}\right)\left(\frac{\Delta\delta\Delta}{(3g_F\mu_B\mathcal{B}_{\rm rot})^2}\right). \tag{5.17}$$

Additionally there is a second order Berry's phase effect that goes as α^2 that is also even under R, which can couple to any non-reversing magnetic field and $\delta\Delta$ to be odd under BD reversal,

$$f^{BD} \sim 3g_F\mu_B\mathcal{B}_{\rm rot}(-3)\left(\frac{3\alpha\omega_{rot}}{3g_F\mu_B\mathcal{B}_{\rm rot}}\right)^2\left(\frac{\delta\mathcal{B}}{\mathcal{B}_{\rm rot}}\right)\left(\frac{\Delta\delta\Delta}{(3g_F\mu_B\mathcal{B}_{\rm rot})^2}\right). \tag{5.18}$$

The tipping angle α is zero when the ions are at the center of the trap, but any displacement away from center in the axial direction and the ions can sample the field inhomogeneities. Because on average the ions are at the center of the trap, $\alpha = 0$ and there is no systematic correction to be made. The uncertainty on the axial displacement is 2.5 mm, which we can determine from the data blocks where axial displacement was recorded. Using the measured value of $T_z\beta_z = (2/3)0.136(6)$ Kelvin/cm^2 from eq. (4.43) we can get an uncertainty on α, $\sigma_\alpha \approx 10^{-7}$. The relevant parameter, $(3\sigma_\alpha\omega_{\rm rot}/3g_B\mu_B\mathcal{B}_{\rm rot}) = 0.00375$ for $\omega_{\rm rot} = 250$ kHz, $\mathcal{E}_{\rm rot} = 24$ V/cm, and Ramsey fringe frequency of 20Hz. We can of course calculate the uncertainty on this parameter for every single block in the data set and take the rms value. When we do this the systematic error contribution from the Berry's phase/axial magnetic field term from eq. (5.17) is 3.46 μHz, and the contribution due to the second order effect from eq. (5.18) is 63.9 nHz. In total this is about a 3×10^{-31} e·cm effect.

5.1.5.4 The effect that looks like $\vec{\mathcal{B}} \cdot \vec{r}$

The unknown effect that is proportional to $\vec{\mathcal{B}}\cdot\vec{r}$ has worst case limits placed on the contribution to f^{BD} using the data in fig. 4.13. In this worst case limit we have removed the contribution to f^B due to $\Delta\delta\Delta/(f^0)^2$, which we empirically observe is also true for this effect. The worse case limit we place on any residual effect that remains after the correction due to the partially understood effect. This limit is $f^{BD} = -0.0047(28)f^B$. The correction and uncertainty of this correction for

any residual effects are

$$f^{\vec{\mathcal{B}}\cdot\vec{r}} = 0.0047 f^{B}, \tag{5.19}$$

$$\sigma^2_{f^{\vec{\mathcal{B}}\cdot\vec{r}}} = (0.0047)^2 \sigma_{f^B} + (-0.0028)^2 f^{B}, \tag{5.20}$$

which yields a correction and uncertainty of -0.102 ± 0.112 mHz, which is consistent with zero. The uncertainty of this systematic is dominated by the block rms value of f^B for the data set. If we reduce the rms value of f^B to 30 mHz via an active servo of the non-reversing magnetic field then the uncertainty of this systematic term drops to the 15 μHz level, or about 10^{-30} $e\cdot$cm. We have already established the Ramsey fringe frequency has no effect on this systematic. Additionally, more careful measurements of the residual effect on f^{BD} due to large f^B yield better uncertainties on this characterization and reduce the systematic error. A potential error in this analysis can come from correlations of the characterized worse cast upper bound, $f^{BD} = 0.0047(28) f^{B}$, with the non-reversing magnetic field. This could potentially be limited by taking data to place upper bounds in the presence of deliberately applied non-reversing magnetic fields.

5.1.5.5 The effect that looks like $\vec{\mathcal{B}} \times \vec{r}$

The unknown effect that looks like $\vec{\mathcal{B}} \times \vec{r}$ has limits placed in its contribution to the EDM channel by the measurement made in fig. 4.15. These limits are $f^{BD} = -0.0018(11) f^{BR}$. We can use the mean value of f^{BR} to calculate the appropriate systematic correction and its uncertainty,

$$f^{\vec{\mathcal{B}}\times\vec{r}} = 0.0018 f^{B}, \tag{5.21}$$

$$\sigma^2_{f^{\vec{\mathcal{B}}\times\vec{r}}} = (0.0018)^2 \sigma_{f^{BR}} + (-0.0011)^2 f^{BR}, \tag{5.22}$$

which yields a correction and correction uncertainty of 66.4 ± 64.8 μHz. This is dominated by the block rms value of f^{BR}, which is about 1 Hz for this set of data. In the past several months we have implemented a more rigorous ion cloud trap displacement shim routine in the experiment control. Under this new control the block rms value of f^{BR} for this data is 0.4 Hz. With f^{BR} reduced to 0.4 Hz the systematic effect in f^{BD} will be about 25 μHz, and it can be suppressed even more, as discussed in section 4.3.2, to well below the 10^{-30} $e\cdot$cm level.

5.1.6 Statistics

We note that several of the systematic errors summarized in section 5.1.5 decrease as the Ramsey fringe frequency increases. On the other hand the statistical sensitivity decreases as the Ramsey fringe frequency increases, as explained in section 3.2.4.1. For coherence times $\tau \ll \tau_{^3\Delta_1}$ the statistical sensitivity of each data point in a Ramsey fringe $\sigma_f \sim 1/\tau \sim f$. For the set of data considered in this section, the ~ 20 Hz Ramsey fringe frequency used happens to provide a good balance between statistical uncertainty and systematic uncertainty. Optimizing this trade-off depends on how much data we intend to take in a run and also how well we think we can control systematic errors. For the rate of 30 mHz/$\sqrt{\text{hour}}$ quoted in chapter 3, and assuming 100 hours of data, this is a 3 mHz statistical uncertainty. The dominant systematic is currently non-reversing magnetic field, and is about 0.17 mHz. If we were faced with the problem of systematic errors that were drastically larger than the statistical uncertainty we could trade statistical uncertainty by decreasing Ramsey fringe frequency to decrease the systematic uncertainty.

5.1.7 Total EDM measurement

The statistical uncertainty in the EDM measurement is 3.11 mHz after the correction in the previous section has been applied. The systematic errors are cataloged in table 5.1. The total systematic uncertainty is 172 μHz. We can compile these into an EDM measurement,

$$2d_e\mathcal{E}_{\text{eff}} = 0.532 \pm 3.12_{\text{stat}} \pm 0.173_{\text{syst}} \pm 1.13_{\text{blind}}\ \text{mHz}, \tag{5.23}$$

or translated to units of $e{\cdot}$cm using $\mathcal{E}_{\text{eff}} = 23.3$ GV/cm,

$$d_e = 0.472 \pm 2.77_{\text{stat}} \pm 0.153_{\text{syst}} \pm 1.00_{\text{blind}} \times 10^{-28}\ e{\cdot}\text{cm}. \tag{5.24}$$

It is also customary to quote measurements consistent with zero as an upper bound. Analytically deriving the single sided upper bound requires making various assumptions about the shape of the distribution of the uncertainties. The best measure of the distribution of these terms we possess is actually the data itself. We will use a numerical technique to calculate the single sided upper

bound, the bootstrap method[24]. This is a Monte Carlo method, where we generate fictitious data sets by sampling from f^{BD} with replacement. By sampling our own data set we are able to generate random numbers that are guaranteed to match the sample distribution. With this fictitious data set we can calculate the value of d_e with systematic corrections. We can then repeat this procedure 10^5 times and calculate what value is greater than d_e for 90% of the fictitious data sets. This places an upper bound on the EDM of $|d_e| < 4.6 \times 10^{-28}$ $e \cdot$cm with 90% confidence (where we are now quoting a 90% confidence interval, rather than 1σ errorbars). This improves on the 2011 limit set by Imperial[36], and is less than a factor of 5 away from the current best limit set by ACME in 2014[7, 27]. This has the potential to be improved upon in the near future. This limit was created using a set of data taken with the intent to study systematic errors. It wasn't optimized for statistical sensitivity, and in contrast to taking care to decrease the impact of systematic errors, we specifically tried to increase the effect of systematics. In the next section we will discuss improvements planned for future experiments.

Table 5.1: Summary of systematic errors. The blind offset is included in this table and treated as a systematic effect. Entries also included at the bottom of the table are the statistical measurement of f^{BD} and the total corrected EDM measurement.

Systematic Effects	Correction (mHz)	Uncertainty (mHz)
blind	-3.38	1.13
non-reversing magnetic field ($\Delta\delta\Delta$)	0.238	0.114
non-reversing magnetic field ($\delta g/g_F$)	-0.0430	0.0100
axial magnetic field	0.000122	0.000103
field inhomogeneity $\sim \alpha^1$		0.00346
field inhomogeneity $\sim \alpha^2$		0.0000639
$f^B \sim \vec{\mathcal{B}} \cdot \vec{r}$	-0.102	0.112
$f^{BR} \sim \vec{\mathcal{B}} \times \vec{r}$	0.0664	0.0648
Total Systematics	0.160	0.173

Measurement	Mean (mHz)	Uncertainty (mHz)
f^{BD}	3.72	3.12
Total EDM Measurement	0.496	3.32

5.2 Future direction of the experiment

In this previous section we present a preliminary measurement, but work is not finished. We arrived at this preliminary measurement with data that was almost entirely meant for studying systematics. There are a number of improvements that are possible in the very short term, near future, and distant future that should make it possible to meet and then exceed the current best limit placed on the electron EDM.

5.2.1 Improvements to current experiment

There are several things that can be done to improve the statistical sensitivity of the current experiment, and also to limit the susceptibility to systematic errors. In the discussed data set we managed to achieve a statistical sensitivity of almost 40 mHz/$\sqrt{\text{hour}}$. It should be possible to do significantly better than this without any material changes to the physical experiment. Blocks of data taken under so-called baseline conditions, which are block taken with parameters meant to investigate the statistical sensitivity of the experiment, i.e. a data point that was not investigating systematic effects, have an average sensitivity that is 22 mHz/$\sqrt{\text{hour}}$, which is already a factor of two better than this measurement. Additionally, we can optimize our data acquisition for statistical sensitivity by only taking data on the zero-crossings of Ramsey fringes, fixing the initial phase of the Ramsey fringe fit, and only taking data at long times of Ramsey fringes. Succeeding in these objectives, we can hope to do even better than our current measurement sensitivity by a factor of two, as discussed in chapter 3. This should allow us to potentially achieve statistical uncertainty of ~ 1 mHz for 100 hours of data.

There are also easy gains possible on the front of systematic errors. Many of the limiting systematics in table 5.1 are essentially a result of large f^B readings, in particular the non-reversing magnetic field systematic and the not yet understood $f^B \sim \vec{\mathcal{B}} \cdot \vec{r}$ effect. It should be possible to actively shim the value of f^B to within 30 mHz of zero by applying a non-reversing magnetic field gradient. We currently perform this shim sporadically whenever the value of f^B for a baseline

set of data becomes too large, but it could easily be added into the experimental sequence after every block. This should reduce both of these systematics to below the 1 mHz level. Additionally we can null out the ambient DC magnetic field in the lab with 3 pairs of coils to reduce the $f^B \sim \vec{\mathcal{B}} \cdot \vec{r}$ effect. We are also in the process of improving the experiment's magnetometry, via the improvements to the cluster of magnetometers described in section 4.2.3. This will allow us to get better measurements of the ambient magnetic fields and magnetic field gradients, which will give us greater confidence in our abilities to null out Earth's field and shim the non-reversing magnetic field gradient.

We are currently in the process of preparing the experiment to run for 100 continuous hours in a mode that is optimized for statistical sensitivity and will be more resilient to systematic errors. We hope to learn a great deal about how far we can push the statistical sensitivity of this iteration of the experiment, and we look forward to uncovering new potential sources of systematic errors that are only visible below the 1 mHz threshold.

5.2.2 Improvements for next generation experiment

Ultimately we would like the statistical sensitivity of this experiment to persist well below the 1 mHz level. The figure of merit for sensitivity is $\mathcal{E}_{\text{eff}}\tau\sqrt{\dot{N}}$, the product of effective electric field, coherence time, and count rate. The effective electric field simply is what it is for our species, and the coherence time τ is already approaching the lifetime of the $^3\Delta_1$ electronic state. The remaining sensitivity gains will come from improvements to our count rate. The first area we will focus on is the efficiency of transfer of ions from the $^1\Sigma_0^+$ state where they are created to the $^3\Delta_1$ state where we perform our spectroscopy. As discussed in section 2.1.4, this is currently 40%. By employing pulsed tapered amplifiers[70] we hope to achieve enough power to be able to perform stimulated Raman adiabatic passage (STIRAP)[8] on the ions, where we hope to realize $\sim$ 90% transfer efficiency. This will yield a factor of 2 increase in count rate, as well as potentially increasing Ramsey fringe contrast.

A second avenue where we hope to improve count rate is by designing and building a 3$^{\text{rd}}$

generation ion trap. The current 2nd generation trap was designed to optimize the efficiency of collection of fluorescence photons, which necessitated most of the surface in the trap to be highly reflective and metallic. We have since switched to using photo-dissociation as our detection technique, obviating many of the current trap features. By painting the trap black with a conductive paint we hope to minimize the influence of patch charges accumulating on trap electrodes, allowing us to achieve better $\mathcal{E}_{\mathrm{rot}}$ field uniformity and to ramp down the confinement of the ion trap. Better $\mathcal{E}_{\mathrm{rot}}$ uniformity will improve systematics, and the ability to ramp down the trap confinement will allow us to load more ions into the trap without increasing ion density, an effect that limits the Ramsey fringe coherence time. By adiabatically ramping down the trap frequencies a factor of 3 in each direction we can increase the trap volume by a factor of $\sqrt{27}$, increasing possible ion number in the trap by a factor of 5.

An additional planned improvement includes changing how we detect the ions of dissociation. Currently we dissociate HfF^+ ions and count the Hf^+ products. Because of the inefficiencies in the various processes of creating ions, state transfer, detection, etc. we might end up counting only tens of Hf^+ ions in the presence of $\sim$1000 HfF ions. The dynamic range of the detector is not good enough to count both Hf^+ and HfF^+, so we count the Hf^+ and allow the HfF^+ mass peak to saturate. This is discarding valuable information that we could use to normalize out technical noise that occurs during the neutral molecule creation, ionization, and state transfer processes. By adding a reflectron in our time of flight (TOF) mass spectrometer we can try to direct the Hf^+ and HfF^+ TOF packets onto separate detectors with different gains, allowing us to accurately count both the number of un-dissociated HfF^+ ions and the number of dissociation Hf^+ products. Additionally, we can also try to use this reflectron to stretch the Hf^+ ion packet out in time, allowing us to operate the ion detector in digital mode, rather than analog mode. The advantage of this is that the digital counting mode has better counting statistics, because the signal is not convolved with an ion peak distribution function.

5.2.3 Potential for ThF^+

Earlier we mentioned that the value of $\mathcal{E}_{\text{eff}}$ is fixed, but this can be tuned slightly with the choice of a different molecular species. The diatomic ion ThF^+ is isoelectronic to HfF^+, but with the advantage of many more protons in the thorium nuclear, enhancing the effective electric field to 36(2) GV/cm[47, 66, 21], roughly 1.5 times larger than HfF^+. This factor goes directly into the potential statistical sensitivity. Moreover, the $^3\Delta_1$ electronic state is the ground state for ThF^+[32], which means that the state lifetime will be limited by excitation from blackbody radiation to excited rotational and vibrational states. With the right ion trap design this could potentially allow us to achieve Ramsey fringes with $>$ 2s coherence times. The downside is that very little is known about ThF^+ that is useful for an EDM measurement. We currently do not have techniques for state-selective ionization, state-selective readout, or state transfer, but experiments are currently underway to investigate these possibilities.

5.3 Conclusion

In conclusion, we present a preliminary upper bound of the electron EDM of $|d_e| < 4.6 \times 10^{-28}$ e·cm with 90% confidence. This limit is derived from data taken with the intent of characterizing systematic shifts of the EDM, and moreover is still blinded. As the measurement appears to be statistics limited, there is a clear short term path to decreasing the upper bound to the 1×10^{-28} level by simply taking data in a more efficient manner. Furthermore, signal enhancement provided by improving state transfer and by constructing a new ion trap capable of storing significantly larger numbers of ion should be able to perform a measurement of the electron EDM at the several 10^{-29} e·cm level.

Bibliography

[1] K. Abdullah, C. Carlberg, E. D. Commins, H. Gould, and S. B. Ross. "New experimental limit on the electron electric dipole moment." Phys. Rev. Lett., **65**, 2347 (1990).

[2] K. Abe, H. Fuke, S. Haino, T. Hams, M. Hasegawa, A. Horikoshi, A. Itazaki, K. C. Kim, T. Kumazawa, A. Kusumoto, M. H. Lee, Y. Makida, S. Matsuda, Y. Matsukawa, K. Matsumoto, J. W. Mitchell, Z. Myers, J. Nishimura, M. Nozaki, R. Orito, J. F. Ormes, K. Sakai, M. Sasaki, E. S. Seo, Y. Shikaze, R. Shinoda, R. E. Streitmatter, J. Suzuki, Y. Takasugi, K. Takeuchi, K. Tanaka, N. Thakur, T. Yamagami, A. Yamamoto, T. Yoshida, and K. Yoshimura. "Search for Antihelium with the BESS-Polar Spectrometer." Phys. Rev. Lett., **108**, 131301 (2012).

[3] M. Abramowitz and I. Stegun. Handbook of Mathematical Functions. Dover Publications (1965).

[4] T. Aoyama, M. Hayakawa, T. Kinoshita, and M. Nio. "Tenth-order QED contribution to the electron $g-2$ and an improved value of the fine structure constant." Phys. Rev. Lett., **109**, 111807 (2012).

[5] C. A. Baker, D. D. Doyle, P. Geltenbort, K. Green, M. G. D. van der Grinten, P. G. Harris, P. Iaydjiev, S. N. Ivanov, D. J. R. May, J. M. Pendlebury, J. D. Richardson, D. Shiers, and K. F. Smith. "Improved experimental limit on the electric dipole moment of the neutron." Phys. Rev. Lett., **97**, 131801 (2006).

[6] B. J. Barker, I. O. Antonov, V. E. Bondybey, and M. C. Heaven. "Spectroscopic measurements for HfF^+ of relevance to the investigation of fundamental constants." The Journal of Chemical Physics, **134**(20), 201102 (2011).

[7] J. Baron, W. C. Campbell, D. DeMille, J. M. Doyle, G. Gabrielse, Y. V. Gurevich, P. W. Hess, N. R. Hutzler, E. Kirilov, I. Kozyryev, B. R. O'Leary, C. D. Panda, M. F. Parsons, E. S. Petrik, B. Spaun, A. C. Vutha, and A. D. West. "Order of magnitude smaller limit on the electric dipole moment of the electron." Science, **343**(17) (2014).

[8] K. Bergmann, H. Theuer, and B. W. Shore. "Coherent population transfer among quantum states of atoms and molecules." Rev. Mod. Phys., **70**, 1003 (1998).

[9] W. Bernreuther and M. Suzuki. "The electric dipole moment of the electron." Rev. Mod. Phys., **63**, 313 (1991).

[10] H. A. Bethe. Elementary Nuclear Theory. John Wiley and Sons, Inc. (1947).

[11] J. Brown and A. Carrington. Rotational Spectroscopy of Diatomic Molecules. Cambridge University Press (2003).

[12] N. Cabibbo. "Unitary symmetry and leptonic decays." Phys. Rev. Lett., **10**, 531 (1963).

[13] Campbell, Wesley C., Chan, Cheong, DeMille, David, Doyle, John M., Gabrielse, Gerald, Gurevich, Yulia V., Hess, Paul W., Hutzler, Nicholas R., Kirilov, Emil, O'Leary, Brendon, Petrik, Elizabeth S., Spaun, Ben, and Vutha, Amar C. "Advanced cold molecule electron edm." EPJ Web of Conferences, **57**, 02004 (2013).

[14] L. Canetti, M. Drewes, and M. Shaposhnikov. "Matter and antimatter in the universe." New Journal of Physics, **14**(9), 095012 (2012).

[15] J. H. Christenson, J. W. Cronin, V. L. Fitch, and R. Turlay. "Evidence for the 2π decay of the K_2^0 meson." Phys. Rev. Lett., **13**, 138 (1964).

[16] E. D. Commins, J. D. Jackson, and D. P. DeMille. "The electric dipole moment of the electron: An intuitive explanation for the evasion of Schiff's theorem." American Journal of Physics, **75**(6), 523 (2007).

[17] K. C. Cossel. Techniques in molecular spectroscopy: from broad bandwidth to high resolution. Ph.D. thesis, University of Colorado (2014).

[18] K. C. Cossel, D. N. Gresh, L. C. Sinclair, T. Coffey, L. V. Skripnikov, A. N. Petrov, N. S. Mosyagin, A. V. Titov, R. W. Field, E. R. Meyer, E. A. Cornell, and J. Ye. "Broadband velocity modulation spectroscopy of HfF^+: Towards a measurement of the electron electric dipole moment." Chemical Physics Letters, **546**, 1 (2012).

[19] D. D. D. Manura. SIMION (R) 6.0. Scientific Instrument Services, Inc. (1996).

[20] D. DeMille, F. Bay, S. Bickman, D. Kawall, L. Hunter, D. Krause, S. Maxwell, and K. Ulmer. "Search for the electric dipole moment of the electron using metastable PbO." AIP Conference Proceedings, **596**(1), 72 (2001).

[21] M. Denis, M. S. Nørby, H. J. A. Jensen, A. S. P. Gomes, M. K. Nayak, S. Knecht, and T. Fleig. "Theoretical study on ThF^+ , a prospective system in search of time-reversal violation." New Journal of Physics, **17**(4), 043005 (2015).

[22] F. G. Dunnington. "A determination of $\frac{e}{m}$ for an electron by a new deflection method." Phys. Rev., **43**, 404 (1933).

[23] S. Eckel, P. Hamilton, E. Kirilov, H. W. Smith, and D. DeMille. "Search for the electron electric dipole moment using Ω-doublet levels in PbO." Phys. Rev. A, **87**, 052130 (2013).

[24] B. Efron. "Bootstrap methods: Another look at the Jackknife." Ann. Statist., **7**(1), 1 (1979).

[25] J. Engel, M. J. Ramsey-Musolf, and U. van Kolck. "Electric dipole moments of nucleons, nuclei, and atoms: The standard model and beyond." Progress in Particle and Nuclear Physics, **71**, 21 (2013).

[26] T. Fleig and M. K. Nayak. "Electron electric-dipole-moment interaction constant for HfF^+ from relativistic correlated all-electron theory." Phys. Rev. A, **88**, 032514 (2013).

[27] T. Fleig and M. K. Nayak. "Electron electric dipole moment and hyperfine interaction constants for ThO." Journal of Molecular Spectroscopy, **300**, 16 (2014). Spectroscopic Tests of Fundamental Physics.

[28] K. Fuyuto, J. Hisano, and E. Senaha. "Toward verification of electroweak baryogenesis by electric dipole moments." (2015).

[29] R. L. Garwin, L. M. Lederman, and M. Weinrich. "Observations of the failure of conservation of parity and charge conjugation in meson decays: the magnetic moment of the free muon." Phys. Rev., **105**, 1415 (1957).

[30] D. Gerlich. "Ion-neutral collisions in a 22-pole trap at very low energies." Physica Scripta, **1995**(T59), 256 (1995).

[31] J. Goldemberg and Y. Torizuka. "Upper limit of the electric dipole moment of the electron." Phys. Rev., **129**, 2580 (1963).

[32] D. N. Gresh, K. C. Cossel, Y. Zhou, J. Ye, and E. A. Cornell. "Broadband velocity modulation spectroscopy of ThF^+ for use in a measurement of the electron electric dipole moment." Journal of Molecular Spectroscopy, **319**, 1 (2016).

[33] D. Hanneke, S. Fogwell Hoogerheide, and G. Gabrielse. "Cavity control of a single-electron quantum cyclotron: Measuring the electron magnetic moment." Phys. Rev. A, **83**, 052122 (2011).

[34] G. E. Harrison, M. A. Player, and P. G. H. Sandars. "A multichannel phase-sensitive detection method using orthogonal square waveforms." Journal of Physics E: Scientific Instruments, **4**(10), 750 (1971).

[35] D. A. Hite, Y. Colombe, A. C. Wilson, K. R. Brown, U. Warring, R. Jördens, J. D. Jost, K. S. McKay, D. P. Pappas, D. Leibfried, and D. J. Wineland. "100-fold reduction of electric-field noise in an ion trap cleaned with *In Situ* argon-ion-beam bombardment." Phys. Rev. Lett., **109**, 103001 (2012).

[36] J. J. Hudson, D. M. Kara, I. J. Smallman, B. E. Sauer, M. R. Tarbutt, and E. A. Hinds. "Improved measurement of the shape of the electron." Nature, **473**(7348), 493 (2011).

[37] J. J. Hudson, M. R. Tarbutt, B. E. Sauer, and E. A. Hinds. "Stochastic multi-channel lock-in detection." New Journal of Physics, **16**(1), 013005 (2014).

[38] N. R. Hutzler. A New Limit on the Electron Electric Dipole Moment: Beam Production, Data Interpretation, and Systematics. Ph.D. thesis, Harvard University (2014).

[39] D. M. Kara, I. J. Smallman, J. J. Hudson, B. E. Sauer, M. R. Tarbutt, and E. A. Hinds. "Measurement of the electron's electric dipole moment using YbF molecules: methods and data analysis." New Journal of Physics, **14**(10), 103051 (2012).

[40] J. R. Klein and A. Roodman. "Blind analysis in nuclear and particle physics." Annual Review of Nuclear and Particle Science, **55**(1), 141 (2005).

[41] M. Kobayashi and T. Maskawa. "CP-violation in the renormalizable theory of weak interaction." Progress of Theoretical Physics, **49**(2), 652 (1973).

[42] A. Leanhardt, J. Bohn, H. Loh, P. Maletinsky, E. Meyer, L. Sinclair, R. Stutz, and E. Cornell. "High-resolution spectroscopy on trapped molecular ions in rotating electric fields: A new approach for measuring the electron electric dipole moment." Journal of Molecular Spectroscopy, **270**(1), 1 (2011).

[43] T. D. Lee and C. N. Yang. "Question of parity conservation in weak interactions." Phys. Rev., **104**, 254 (1956).

[44] H. Loh. Search for an electron electric dipole moment with trapped molecular ions. Ph.D. thesis, University of Colorado (2013).

[45] H. Loh, K. C. Cossel, M. C. Grau, K.-K. Ni, E. R. Meyer, J. L. Bohn, J. Ye, and E. A. Cornell. "Precision spectroscopy of polarized molecules in an ion trap." Science, **342**(6163), 1220 (2013).

[46] H. Loh, J. Wang, M. Grau, T. S. Yahn, R. W. Field, C. H. Greene, and E. A. Cornell. "Laser-induced fluorescence studies of HfF^+ produced by autoionization." The Journal of Chemical Physics, **135**(15), 154308 (2011).

[47] E. R. Meyer and J. L. Bohn. "Prospects for an electron electric-dipole moment search in metastable ThO and ThF^+." Phys. Rev. A, **78**, 010502 (2008).

[48] E. R. Meyer, J. L. Bohn, and M. P. Deskevich. "Candidate molecular ions for an electron electric dipole moment experiment." Phys. Rev. A, **73**, 062108 (2006).

[49] P. J. Mohr, D. B. Newell, and B. N. Taylor. "CODATA recommended values of the fundamental physical constants: 2014." (2015).

[50] K.-K. Ni, H. Loh, M. Grau, K. C. Cossel, J. Ye, and E. A. Cornell. "State-specific detection of trapped HfF^+ by photodissociation." Journal of Molecular Spectroscopy, **300**, 12 (2014). Spectroscopic Tests of Fundamental Physics.

[51] A. N. Petrov, N. S. Mosyagin, T. A. Isaev, and A. V. Titov. "Theoretical study of HfF^+ in search of the electron electric dipole moment." Phys. Rev. A, **76**, 030501 (2007).

[52] A. N. Petrov, N. S. Mosyagin, and A. V. Titov. "Theoretical study of low-lying electronic terms and transition moments for HfF^+ for the electron electric-dipole-moment search." Phys. Rev. A, **79**, 012505 (2009).

[53] M. A. Player and P. G. H. Sandars. "An experiment to search for an electric dipole moment in the $^3P_2$ metastable state of xenon." Journal of Physics B: Atomic and Molecular Physics, **3**(12), 1620 (1970).

[54] M. Pospelov and A. Ritz. "Electric dipole moments as probes of new physics." Annals of Physics, **318**(1), 119 (2005).

[55] E. M. Purcell and N. F. Ramsey. "On the possibility of electric dipole moments for elementary particles and nuclei." Phys. Rev., **78**, 807 (1950).

[56] N. F. Ramsey. "A molecular beam resonance method with separated oscillating fields." Physical Review, **78**(6) (1950).

[57] B. C. Regan, E. D. Commins, C. J. Schmidt, and D. DeMille. "New limit on the electron electric dipole moment." Phys. Rev. Lett., **88**, 071805 (2002).

[58] R. Rosenberg, M. McDowell, and J. Noonan. "X-ray photoelectron spectroscopy analysis of aluminum and copper cleaning procedures for the advanced photon source." Journal of Vacuum Science and Technology, A (Vacuum, Surfaces and Films); (United States), **12:4** (1994).

[59] P. Rosenbusch. "Magnetically trapped atoms for compact atomic clocks." Applied Physics B, **95**(2), 227 (2009).

[60] A. D. Sakharov. "Violation of CP invariance, C asymmetry, and baryon asymmetry of the universe." Soviet Physics Uspekhi, **34**(5), 392 (1991).

[61] E. E. Salpeter. "Some atomic effects of an electronic electric dipole moment." Phys. Rev., **112**, 1642 (1958).

[62] P. Sandars. "Enhancement factor for the electric dipole moment of the valence electron in an alkali atom." Physics Letters, **22**(3), 290 (1966).

[63] P. G. H. Sandars and E. Lipworth. "Electric dipole moment of the cesium atom. a new upper limit to the electric dipole moment of the free electron." Phys. Rev. Lett., **13**, 718 (1964).

[64] L. I. Schiff. "Measurability of nuclear electric dipole moments." Phys. Rev., **132**, 2194 (1963).

[65] S. Seidelin, J. Chiaverini, R. Reichle, J. J. Bollinger, D. Leibfried, J. Britton, J. H. Wesenberg, R. B. Blakestad, R. J. Epstein, D. B. Hume, W. M. Itano, J. D. Jost, C. Langer, R. Ozeri, N. Shiga, and D. J. Wineland. "Microfabricated surface-electrode ion trap for scalable quantum information processing." Phys. Rev. Lett., **96**, 253003 (2006).

[66] L. V. Skripnikov and A. V. Titov. "Theoretical study of ThF^+ in the search for T, P-violation effects: Effective state of a Th atom in ThF^+ and ThO compounds." Phys. Rev. A, **91**, 042504 (2015).

[67] J. H. Smith, E. M. Purcell, and N. F. Ramsey. "Experimental limit to the electric dipole moment of the neutron." Phys. Rev., **108**, 120 (1957).

[68] Space Physics Data Facility (SPDF). "Common Data Format."

[69] J. Swift and M. Cunliffe. Gulliver's Travels. Jones & Company (1726).

[70] K. Takase, J. K. Stockton, and M. A. Kasevich. "High-power pulsed-current-mode operation of an overdriven tapered amplifier." Opt. Lett., **32**(17), 2617 (2007).

[71] The HDF Group. "Hierarchical data format version 5." (2000-2010).

[72] M. C. Weisskopf, J. P. Carrico, H. Gould, E. Lipworth, and T. S. Stein. "Electric dipole moment of the cesium atom. a new upper limit to the electric dipole moment of the electron." Phys. Rev. Lett., **21**, 1645 (1968).

[73] D. W. Williams and W. T. Williams. "Effect of electrode surface finish on electrical breakdown in vacuum." Journal of Physics D: Applied Physics, **5**(10), 1845 (1972).

[74] C. S. Wu, E. Ambler, R. W. Hayward, D. D. Hoppes, and R. P. Hudson. "Experimental test of parity conservation in beta decay." Phys. Rev., **105**, 1413 (1957).

Appendix A

Typical experiment parameters

Table A.1: Typical parameter values for the experiment. We have also collected data at other values of $\mathcal{E}_{\rm rot}, \omega_{\rm rot}, \boldsymbol{\nabla}\mathcal{B}$, etc., which change many of the parameters below.

	Typical Value	Source	Description
N	2000		number of trapped ions
m	199 amu		mass of ^{180}Hf^{19}F$^+$
$\mathcal{E}_{\rm rot}$	24 V/cm		rotating electric field
$\omega_{\rm rot}$	$2\pi \times 250$ kHz		rotational micromotion frequency
$\omega_{\rm rf}$	$2\pi \times 50$ kHz		ion trap rf frequency
$\omega_{\rm sec}$	$2\pi \times (5, 4, 1.5)$ kHz		(x, y, z) trap secular frequencies
T	30 Kelvin		initial ion cloud temperature
$T_{\rm relaxed}$	10 Kelvin		relaxed trap temperature
$r_{\rm rot}$	0.47 mm	$\frac{e\mathcal{E}_{\rm rot}}{m\omega_{\rm rot}^2}$	rotational micromotion radius
$v_{\rm rot}$	740.8 m/s	$\frac{e\mathcal{E}_{\rm rot}}{m\omega_{\rm rot}}$	rotational micromotion velocity
$\boldsymbol{\nabla}\mathcal{B}$	40 mGauss/cm		magnetic quadrupole gradient
$\mathcal{B}_{\rm rot}$	1.88 mGauss	$\boldsymbol{\nabla}\mathcal{B} r_{\rm rot}$	rotating magnetic field
g_F	+0.00305(10)	[45]	$^3\Delta_1, J = 1, F = 3/2$ g-factor
$\delta g/g_F$	-0.00099(1)	$\frac{(g_F^u - g_F^l)}{(g_F^u + g_F^l)}$	differential g-factor
f^0	23.7 Hz	$3 g_F \mu_B \mathcal{B}_{\rm rot}$	mean Ramsey fringe frequency
τ	1 s		Ramsey fringe coherence time
ω_{ef}	$2\pi \times 740(40)$ kHz	[18]	$^3\Delta_1$ Λ-doubling
E_{HF}	-46.6(1) MHz		$^3\Delta_1$ hyperfine splitting
$d_{\rm mf}$	1.805(8) MHz/(V/cm)	$1.411(6)\, e\, a_0$	molecule frame dipole moment
Δ	3.84 Hz	$27\omega_{ef}\left(\frac{\omega_{\rm rot}}{d_{mf}\mathcal{E}_{\rm rot}}\right)^3$	rotation-induced mixing
$\delta\Delta$	-1.34 Hz	$\frac{3}{8}\Delta\left(\frac{d_{\rm mf}\mathcal{E}_{\rm rot}}{E_{HF}}\right)$	differential rotation-induced mixing
f^D	-0.217 Hz	$\frac{\Delta\delta\Delta}{3 g_F \mu_B \mathcal{B}_{\rm rot}}$	doublet odd frequency combination
$\mathcal{E}_{\rm eff}$	23.3 GV/cm	[26]	effective electric field
$2 d_e \mathcal{E}_{\rm eff}$	1.13 mHz/(10^{-28} $e\cdot$cm)		electron EDM splitting

Appendix B

Matlab code to generate linear combinations channels

```
function lcom_table = generate_lcoms(varargin)
%GENERATE_LCOMS   generate linear combinations of EDM data.
%   lcom_table = GENERATE_LCOMS(data) produces the linear combinations of
%   the various channels in the table data. The function has the following
%   three input flags:
%
%   lcom_table = GENERATE_LCOMS(data,'switches',switches)
%       will calculate the linear combination over the subset of switches
%       provided in 'switches'. GENERATE_LCOMS will produce 2^N linear
%       combinations, where N is the length of 'switches'. The input
%       'switches' must be a cell array of column labels for the table
%       data. The default value of 'switches' is{'Brot','Doublet','Rotation'}
%
%   lcom_table = GENERATE_LCOMS(data,'avg_index',ind)
%       will calculate the linear combinations taking averages over
%       parameters whose values change more quickly than we might wish to
%       differentiate into individual blocks. The variable 'ind' must be a
%       cell array of column labels to average over. The default value of
%       'ind' is {'hff'}, where we average over the number of HfF counts.
%
%   lcom_table = GENERATE_LCOMS(data,'filter',ind)

%% Parse the inputs
p = inputParser;
addRequired(p,'data',@istable);
addParameter(p,'switches',{'Brot','Doublet','Rotation'},@iscell);
addParameter(p,'avg_index',{'hff'},@iscell);
parse(p,varargin{:});

data = p.Results.data;
avg_index = p.Results.avg_index;
switches = p.Results.switches;

%% Descriptors and Symbols
% define symbols for each switch
known_switch_labels = {'Brot','Doublet','Rotation'};
known_switch_symbols = {'B','D','R'};
```

```
% define symbols for each channel
channels = {'freq','phase','offset','contrast','tau'};
channel_symbols = {'f','p','O','C','t'};
% check for unknown switches. If we find any this function should be
% updated!
if ~all(arrayfun(@(x) ismember(x,known_switch_labels),switches))
    error('sorry, generate_lcoms cant recognize on of your switch labels');
end
% concatenate all of the switch symbols into a string.
switch_symbols = strjoin(known_switch_symbols,'');

%% Generate the parity sums
% turn the recorded switch state of 0 or 1 into -1 or +1.
data_parity = (-1).^(1+data{:,switches});
% pick out a matrix of the measured value of each data channel (for speed).
data_channels = data{:,channels};
% find the columns that have text data
text_columns = data.Properties.VariableNames(arrayfun(@(i) iscell(data{1,i})
    ,1:size(data,2)));
% construct the columns that we will use to index individual blocks.
block_index = setxor(data.Properties.VariableNames,[switches channels cellfun
    (@(x) ['s_' x],channels,'uni',false) avg_index]);
block_index = block_index(~ismember(block_index,text_columns));
% put the text columns at the beginning of the output table
block_index = [text_columns block_index(~any(isnan(data{:,block_index})))];
% assign a block index to each row of input data
[~,~,index] = unique(data(:,block_index));
% Choose other columns to save. These will also be averaged over
columns = setxor(data.Properties.VariableNames,[text_columns switches channels
    cellfun(@(x) ['s_' x],channels,'uni',false)]);
% Generate a ptable of parities. This is a table of 1s and 0s that
% describes all the various ways to combine the switches for a block. It
% has 2^N rows and N columns, where N is the number of switches.
parity = logical(de2bi((1:2^length(switches))-1'));
% Generate symbols for all the various combinations for each channel. This
% should have length M*2^N, where M is the number of channels (f, phi, ...)
% and N is the number of switches. This will include entries like 'f',
% 'fBD', 'tD', etc.
linear_combinations = cell(1,length(channels)*size(parity,1));
for c=1:length(channels)
    for p=1:size(parity,1)
        linear_combinations{(c-1)*size(parity,1) + p} = [channel_symbols{c}
    switch_symbols(parity(p,:))];
    end
end
% find which column in the data each linear combination refers to.
linear_combination_columns = arrayfun(@(x) find(ismember(channel_symbols,x),1,
    'first'),cellfun(@(x) x(1),linear_combinations));
% lcom_table is the variable we will store all of the various linear
% combinations.
lcom_columns = [cellfun(@(x) strcat('s',channel_symbols{ismember(channels,x)})
    ,channels,'uni',false) linear_combinations];
n_rows = length(min(index):max(index));
```

```
lcom_table = array2table(zeros(n_rows,length(columns)),'VariableNames',columns);
lcom_table(:,text_columns) = cell2table(repmat({''},n_rows,length(text_columns)));
lcom_table(:,lcom_columns) = array2table(zeros(n_rows,length(lcom_columns)),'VariableNames',lcom_columns);
% Iterate through each block of data by block index.
for i = min(index):max(index)
    % extract the subtable of data that describes block with index i
    block = data(i==index,:);
    % find the parity that describes how to cobinate the data channels in
    % this block into the linear combinations
    block_parity = data_parity(i==index,:);
    % find the matrix of numerical data that is the data channels for this
    % subblock
    block_channels = data_channels(i==index,:);
    n = size(block,1);
    % create a table, 'row', that is the average of the columns we want
    % (things like ion number and date). This is a temporary table for this
    % block
    row = cell2struct(num2cell(mean(block{:,columns},1))',columns);
    for j=1:length(text_columns)
        row.(text_columns{j}) = block{1,text_columns{j}};
    end
    % append to this table the errorbars combined in quadrature for each
    % channel, to get things like 'sf', 'sO', etc..
    for c = 1:length(channels)
        row.(['s',channel_symbols{c}]) = sqrt(sum(block.(['s_',channels{c}]).^2))/n;
    end
    % Now we loop through all the linear combinations we would like to make
    for p = 1:length(linear_combinations)
        % lcom will be shorthand for the specific linear combination we are
        % considering. It is a text string that describes the channel and
        % also the parity of the combinations, e.g. fBD
        lcom = linear_combinations{p};
        % Channel data is a vector of the data for that particular channel,
        % for the particular block we are considering. lcom(1) holds the
        % character that indentifies this channel, e.g. 'f'
        channel_data = block_channels(:,linear_combination_columns(p));
        % Now loop through the rest of the combination text string to
        % figure out the parity of the sums. channel_data is multiplied by
        % (-1) anytime it coincides with the '0' state of any switch.
        for s = 2:length(lcom)
            lcom_parity_bits = block_parity(:,switch_symbols==lcom(s));
            channel_data = channel_data.*lcom_parity_bits;
        end
        % append this onto temporary table for this block
        row.(lcom) = sum(channel_data)/n;
    end
    % Append the table for this block onto the overall table
    lcom_table(i,:) = struct2table(row);
end
```

```
134 lcom_table = [table((min(index):max(index))','VariableNames',{'index'})
    lcom_table];
135
136 %% Find the EDM channel and apply the blind.
137 % if the blind exists, load it into memory and apply it to the fBD channel.
138 if exist('X:\BLIND\BLIND','file')
139     lcom_table.fBD = lcom_table.fBD + fread(fopen('X:\BLIND\BLIND'),1,'double'
    ); fclose('all');
140 % if the blind doesn't exist, don't look at the data unblinded! Apply a
141 % very large blind instead (4+/-1 10^27 e-cm).
142 else
143     % 2*(10^-27 cm)*(23.3e9 eV/cm)/h = 0.0112678304 hertz
144     edm27 = 0.0112678304;
145     lcom_table.fBD = lcom_table.fBD + normrnd(4*edm27,edm27);
146     fprintf('BLIND not found. Using new random blind 4+/-1 10^27 e-cm\n');
147 end
148 end
```